STUDY ON GENERATION OF ATTOSECOND PULSE WITH POLARIZATION GATING

by

SHAMBHU GHIMIRE

B.Sc., Tribhuvan University, Nepal, 1997
M.Sc., Tribhuvan University, Nepal, 2000
M.S., Kansas State University, 2003

AN ABSTRACT OF A DISSERTATION

submitted in partial fulfillment of the requirements for the degree

DOCTOR OF PHILOSOPHY

Department of Physics

College of Arts and Sciences

KANSAS STATE UNIVERSITY
Manhattan, Kansas

2007

Abstract

It is still a dream to image the dynamics of electrons in atoms and molecules experimentally. This is due to the fact that such motion takes place in an ultra-short time scale; for example, an electron moves around the Bohr orbit in about 150-as (1 as = 10^{-18} s), and pulses much shorter than this limit are not currently available to probe such fast dynamics. In recent years, an isolated single attosecond pulse has been produced by extracting the *cutoff* of harmonic spectrum driven by a laser pulse as short as ~ 5fs (1fs =10^{-15} s). But, these pulses are still too long in order to make the dream come true. Here, we study the possibility of generation of a much shorter and wavelength tunable *single* attosecond pulse by using polarization gating.

In the experiment, we compressed ~30fs pulses from the laser amplifier down to ~6fs and characterized them. These linearly polarized pulses were converted to ellipticity varying pulses, and by exploiting the property of the strong dependence of the harmonic signal with the ellipticity of the laser, an XUV supercontinuum was produced in the harmonic spectrum which could support 60-as pulses. The bandwidth of such a supercontinuum, and therefore the duration of the attosecond pulses, is limited mainly by the currently available energy of the driving laser pulses at few cycle limits. In this project, we present an approach which allowed us to scale up the energy of such pulses by a factor of 1.5 in "*Hollow Core Fiber / Chirped Mirrors Compressor*".

Finally, in order to temporarily characterize the attosecond pulses we designed and built an "A*ttosecond Streak Camera*". Most of such cameras to date are limited to measuring a 1 dimensional energy spectrum and have only a few degrees of acceptance angle. Our camera is capable of measuring 2d momentum of the photoelectrons with large acceptance angle, for example ~ 65^{o} at the photoelectron of energy ~15 eV. Recently, we observed the sidebands in addition to the main peaks in their laser assisted XUV photoelectron spectrum. The single attosecond pulses, after being characterized with this high speed camera, can be used to explore the dynamics of electrons at the attosecond scale.

STUDY ON GENERATION OF ATTOSECOND PULSE WITH POLARIZATION GATING

by

SHAMBHU GHIMIRE

B.Sc., Tribhuvan University, Nepal, 1997
M.Sc., Tribhuvan University, Nepal, 2000
M.S., Kansas State University, 2003

A DISSERTATION

submitted in partial fulfillment of the requirements for the degree

DOCTOR OF PHILOSOPHY

Department of Physics

College of Arts and Sciences

KANSAS STATE UNIVERSITY
Manhattan, Kansas

2007

Approved by:

Major Professor
Zenghu Chang

Abstract

It is still a dream to image the dynamics of electrons in atoms and molecules experimentally. This is due to the fact that such motion takes place in an ultra-short time scale; for example, an electron moves around the Bohr orbit in about 150-as (1 as = 10^{-18} s), and pulses much shorter than this limit are not currently available to probe such fast dynamics. In recent years, an isolated single attosecond pulse has been produced by extracting the *cutoff* of harmonic spectrum driven by a laser pulse as short as ~ 5fs (1fs =10^{-15} s). But, these pulses are still too long in order to make the dream come true. Here, we study the possibility of generation of a much shorter and wavelength tunable *single* attosecond pulse by using polarization gating.

In the experiment, we compressed ~30fs pulses from the laser amplifier down to ~6fs and characterized them. These linearly polarized pulses were converted to ellipticity varying pulses, and by exploiting the property of the strong dependence of the harmonic signal with the ellipticity of the laser, an XUV supercontinuum was produced in the harmonic spectrum which could support 60-as pulses. The bandwidth of such a supercontinuum, and therefore the duration of the attosecond pulses, is limited mainly by the currently available energy of the driving laser pulses at few cycle limits. In this project, we present an approach which allowed us to scale up the energy of such pulses by a factor of 1.5 in "*Hollow Core Fiber / Chirped Mirrors Compressor*".

Finally, in order to temporarily characterize the attosecond pulses we designed and built an "A*ttosecond Streak Camera*". Most of such cameras to date are limited to measuring a 1 dimensional energy spectrum and have only a few degrees of acceptance angle. Our camera is capable of measuring 2d momentum of the photoelectrons with large acceptance angle, for example ~ 65^{o} at the photoelectron of energy ~15 eV. Recently, we observed the sidebands in addition to the main peaks in their laser assisted XUV photoelectron spectrum. The single attosecond pulses, after being characterized with this high speed camera, can be used to explore the dynamics of electrons at the attosecond scale.

Table of Contents

List of Figures

Acknowledgements

Any work of this magnitude would not be possible by my solo effort. It includes the contribution of a group of scientists, students, and staff. I am highly indebted to my major professor, Dr. Zenghu Chang for his guidance and support throughout the course of this work.

During the period of these five years, our research group grew up significantly from 7 members to 15 members currently and everyone has contributed to this work. Thank you all the past and present group members. I am happy to have Dr. Ximao Feng working together with me in this experiment. I believe that we made a good team not only when the experiment worked out well but also when it did not.

Most of the experiments were born in Al Rankin's PC in the form of Cadkey drawings. Thank you Al and other support staff of J.R. Macdonald lab for being so helpful to accomplish this scientific work. Sometimes, the data acquisition system and electronics acted like the frustrating part of the experiment. But, Dr. Kevin Carnes's expertise and his answers to my every question about electronics made the data acquisition and analysis successful in our every beam time.

A most senior person of this lab has spent many continuous hours in the setup regardless of his busy schedule and taught me how to take control over the experiment many times. That is Dr. Lewis Cocke. Thank you very much Lew and your group members for supporting my experiment. I would like to thank Dr. Uwe Thumm and Dr. Shuting Lei for their time and suggestion as my supervisory committee member. I would like to thank Dr. Kenneth Carpenter for conducting my final exam and providing me suggestions on my dissertation. I take this opportunity to thank Carol Regehr for correcting my grammar in various papers and reports including this dissertation.

I am grateful to my wife, Jyoti for her support to make my graduate study successful. Our eight month old son, Safal, I look forward to seeing you walking to my graduation commencement.

Finally, I am grateful for the financial support provided by the J. R. Macdonald Lab and the Physics Department for my graduate study.

Dedication

To my parents

CHAPTER 1 - Introduction

A shorter exposure time with a faster shutter speed is desired in photography in order to capture fast motions such as a spinning football. Rapid advances in laser technology over the past two decades have made it possible to *"photograph"* the rotational and vibrational motions in an atomic system as these motions occur on time scales from a few fs [1 fs = 10^{-15} s] to several hundreds of fs. Much scientific effort has been put forward for the generation of shorter and shorter light pulses in order to track even faster fundamental processes. Electron dynamics are much faster in time scale. Typically an electron takes ~150 as [1 as = 10^{-18}s] for a complete rotation in the Bohr orbit. One needs a pulse shorter than this period for tracking dynamics of the electrons in atomic orbits. The study of the dynamics of electrons could be a key for next-generation technology. For example, the study of the dynamics of electrons or holes in a semiconductor is likely to have an impact for developing faster electronic devices in the future.

A typical Chirp Pulse Amplification (CPA) based Ti-Sapphire Laser system can produce laser pulses as short as ~20 fs [1,2] with pulse energy capable of performing strong field (intensity from 10^{15} to 10^{18}W/cm^2) experiments. The duration of a pulse from such a system is mostly limited by the finite width of the gain of the amplifier material and gain narrowing during the amplification process. So, a CPA system requires an additional pulse compression scheme in order to produce pulses less than 10 fs. This additional pulse compression scheme generally consists of nonlinear propagation followed by dispersion compensation. The Hollow Core Fiber/Chirped Mirror Compressor has become the most standard way of producing pulses in this limit. So far, the output pulse energy obtained with this scheme is less than 1 mJ [1,3,4]; however, many experiments such as the measurement of harmonic generation with polarization gating in a single shot, must be carried out with higher pulse energy in order to increase the XUV flux. Thus, the studies leading towards the possibilities of increasing the energy of *few cycle pulses* are important. Here, we study and present a novel approach for scaling up the energy of *a few cycle pulse*.

During the last few years, significant efforts have been put forward for compressing laser pulses directly from the oscillator [5] as well as after CPA[1,3,4]. However, there is a natural limit on how short one can compress these laser pulses. For example, in a Ti-Sapphire laser

system (wavelength of 780 nm) one cycle is 2.6 fs long and that sets the limit. Thus, in order to obtain even shorter pulses needed for probing the motion of an electron, one has to consider shorter wavelengths such as the XUV range. For example, at the photon energy of 35.6 eV, corresponding to the 23rd harmonic of the Ti-Sapphire laser, one cycle lasts as short as 35-as. Thus, XUV range could be the appropriate spectral range for generation of a pulse less than 1-fs.

Many XUV sources such as x-ray tubes cannot be used for generating sub-fs pulses because of the lack of coherence of the emitted wavelengths. So far, high-order harmonics generation (HHG) in noble gases has been proved experimentally to be the most promising route for producing attosecond pulses [6, 7]. Under an intense linearly polarized laser field, the valence electron in an atom/molecule can tunnel through the Coulomb barrier, and oscillates in the field. The freed electron has a certain probability to be driven back to its parent ion and recombine with it and release the accumulated energy in the form of bursts of electromagnetic waves, which has been known as HHG. This process occurs every half cycle of the laser field and produces an attosecond pulse train when the driving pulse has many cycles. The interference of these attosecond pulses results in a frequency comb with an interval of twice the driving field photon energy.

When an ultra-short few-cycle driving field is used for HHG, the *cutoff* of the spectrum may become a continuum which corresponds to one re-collision at the peak of the driving field. By selecting the *cutoff* of the spectrum, an isolated single attosecond pulse of duration ~250 as [6, 7] has been generated. However, a much broader continuum is desired in order to further shorten the pulse in the time domain. This requires producing a continuum not only at the *cutoff* but also at the *plateau* of the harmonic spectrum. But only one recombination out of many has to be allowed per driving pulse. Here, we explored the possibilities of controlling the trajectories of the re-scattering electrons experimentally by using "*Polarization Gating*" [8, 9]. Furthermore, a broader XUV supercontinnum can support a shorter pulse in real time. Thus, studies for extending the supercontinnum are very important. Here, we studied the possibility by polarization gated HHG in a mixture of noble gases.

In order to image the dynamics of electrons in real time, a time-resolved measurement is required. In such a measurement the motion of the electron has to be first initiated (pump) and then probed with attosecond resolution. With current technology, precise timing in the attosecond scale between the pump and probe is only possible by using a CE phase stabilised

laser timed over temporarily characterized attosecond pulses. The real time characterization of the attosecond pulses in this wavelength range is however very challenging. It is mainly because the standard techniques of autocorrelation for pulse characterization are impossible to be applied here because of the lack of suitable optical materials at these wavelengths and of efficient nonlinear processes at the provided intensities. A conventional streak camera is an alternative for the characterization of x-ray pulses but the resolution of this method is limited to ~300 fs [11]. It has been understood that the limit of resolution is mainly caused by the rise time (60-ps) of the deflecting field and transit time dispersion for the electron beam in the streak camera. Limitation of the deflecting field can be avoided by using a laser field as the deflecting field which has much faster rise time, for example ~650 as for Ti-Sapphire. Another limitation of transit time dispersion can be avoided when the photoelectrons are streaked by the IR field as soon as they are born.

In this method, the electron replica of the XUV attosecond pulse is produced by photoionization of Ne gas, and it receives a streak from the electric field of laser with the amplitude and direction depending upon the value of vector potential of the laser when the electron is born. Thus, the change in momentum of photoelectrons in the laser field depends on the delay between XUV and IR and the intensity of IR. By measuring the momentum shift for several delays it is proposed to trace the electric field of IR as well as the complete temporal characteristics of the XUV pulses. In recent years, a few such high speed cameras have been built [6, 7] but they are limited to 1d energy measurement and have an acceptance angle of a few degrees only. Here, we designed and built one which is capable of measuring a 2d momentum spectrum with much larger acceptance angle.

In my dissertation I cover important aspects of increasing the energy of few cycle pulses, their characterization, and their application in XUV supercontinuum generation and our design of the attosecond streak camera for the time-resolved measurements. The dissertation is organized as follows. In chapter 2, I discuss our novel approach for increasing the energy of few cycle pulses. I also report on the characterization of such pulses in both the spectral and time domains using SHG-FROG. In chapter 3, I present our experimental method of converting this linear pulse into a pulse having time dependent ellipticity and thus using it for producing an XUV supercontinuum. I also discuss a method for obtaining a broader supercontinuum by exciting a mixture of noble gases with such pulses. Chapter 4 of the dissertation contains the

detail of designing the attosecond streak camera for studying time- resolved absorption spectroscopy. It includes the recent progress we made by observing side bands in the laser dressed XUV photoelectron spectrum. Finally, in chapter 5, I summarize my contribution and present a general description of future possibilities in attosecond science based on the effort presented here. The appendices at the end of the dissertation contain important reference material cited in the text, a brief description of the light source used in the experiment, a brief description of some of the most important electronic modules, and the reconstruction codes used in the analysis of the data collected in the time-resolved measurement.

CHAPTER 2 - Generation and Characterization of Few Cycle Laser Pulses

2.1 Introduction and Previous Work

High-order harmonic generation in noble gases using laser pulses of duration ~40 fs directly from a CPA system has been used to produce a train of attosecond pulses of duration 250-as on every half laser cycle (T/2 = 1.3-fs)[12]. The time interval between these pulses is so short that many physical, chemical, or biological processes do not have sufficient time to be completed and get to the initial state. So, in most of the pump-probe studies using a train of pulses, the following pulses do not really get a chance to initialize these processes from the initial states. Therefore, the train of pulses imposes severe restrictions on the study of fast physical processes. This called for producing a *single* attosecond pulse. Generation of a *single* attosecond pulse has been done, either by filtering the *cutoff* of the harmonics spectrum [5, 6] or by controlling the trajectories of returning electrons using polarization gating [7]. Both of these approaches require that the pulses from the CPA system have to be further compressed and made no longer than 5-8 fs. Such short laser pulses are called "*few cycle laser pulses*" and of course by name they have only a few carrier cycles within the pulse. For example 6-fs pulses from the Ti-Sapphire laser have only two laser cycles.

In the history of generation of sub-ten-fs laser pulses we can go back to 1985, when the single-mode optical fiber / grating compressor technique was used to compress the laser pulses from a mode-locked dye laser and generate a pulse as short as 8-fs [13]. Two years later, pulses were further compressed further to 6-fs by better dispersion compensation using the combination of a prism and a grating. Even though the pulses obtained by this technique were short, the use of single-mode fibers were limited to low energy (nJ) due to possible damage of the material and appearance of high order nonlinearities.

In the last decade, the availability of mJ pulses from a solid state laser, and the requirement for higher pulse energy for strong field processes such as high order harmonic generation, called for new pulse compressor technique. In 1996 M. Nisoli *et al.* came out with a

pulse compression technique suitable for higher energy pulses [15]. In this technique a hollow core fiber filled with noble gases replaced the single-mode optical fiber for spectral broadening. This technique also exploited the high threshold intensity of noble gases for multiphoton ionization in order to propagate the high energy pulses. They compressed 140-fs pulses of energy 0.6 mJ from a Ti:Sapphire laser down to 10-fs with pulse energy of 0.24 mJ. One year later, S. Sartania *et al.* followed this measurement using shorter input pulses (20fs) and obtained a compressed pulse of duration as short as 5-fs with pulse energy up to 0.5 mJ [16]. In that measurement they replaced the traditional way of using a prism for dispersion compression with broad band chirped mirrors in order to avoid self focusing of the high energy beam on to the material of the prism.

Both theoretical [17, 18] and experimental studies [15] have been put forward to understand the constraints for obtaining higher energy pulses in this technique. It is believed that multiphoton or tunnelling ionizations and self-focusing are the two dominating factors that limit the maximum input energy on to the hollow fiber before the spatial mode of the output beam breaks. On one hand, the ionized gases can cause the laser beam to defocus mainly in the region close to the entry and inside the fiber. On the other hand, the self-focusing can transfer the energy of the pulse from the fundamental mode to higher order modes in the fiber. Some efforts have been put forward for increasing the output energy of this technique, for example, a method of using a differential pumping scheme [19], where the gas pressure was configured inside the fiber in such a way that the pressure at the entrance is lower than that at the exit. Here, we study another method of using circular polarization input to the fiber and scale up the energy of few cycle pulses significantly.

Similarly, the history of the characterization of laser pulses leads us to 1991, when the measurement of the amplitude and phase of short laser pulses (250-fs) was reported for the first time [20]. This measurement was more informative than the traditional attocorrelators as the information of the phase of the pulse used to be completely unknown otherwise. The drawbacks of this method, however, were that the method could not be easily adapted to single-shot measurements, and that a reference pulse was required in such measurements. Later in 1993, FROG (Frequency Resolved Optical Gating), capable of single-shot as well as multi-shot measurements was introduced [21] with the first time characterization of 100-fs laser pulses in self reference mode (without using any other reference pulse).

As the technology advanced, much shorter laser pulses in sub-ten-fs range became routinely available. These short laser pulses consist of at least a few hundreds of nm of bandwidth which imposed a challenge on their characterization because (i) the simultaneous up-conversion of the entire bandwidth of the fundamental pulse in the nonlinear medium was difficult to achieve; (ii) broadening of the pulse in the nonlinear medium due to dispersion confused the measurement; and (iii) the spectral response of the detector as well as the optics used in the measurement are generally not flat over the entire bandwidth. Baltuska *et al*. showed the first measurement [22] of sub-ten-fs (4.5-fs) pulses. Here, we design a single-shot SHG-FROG capable of characterizing shorted available pulses in the infrared. We study the phase matching property of BBO crystal with respect to its thickness and find the appropriate thickness capable of up-converting the entire bandwidth of the few cycle pulses almost simultaneously.

2.2 Experimental Setup

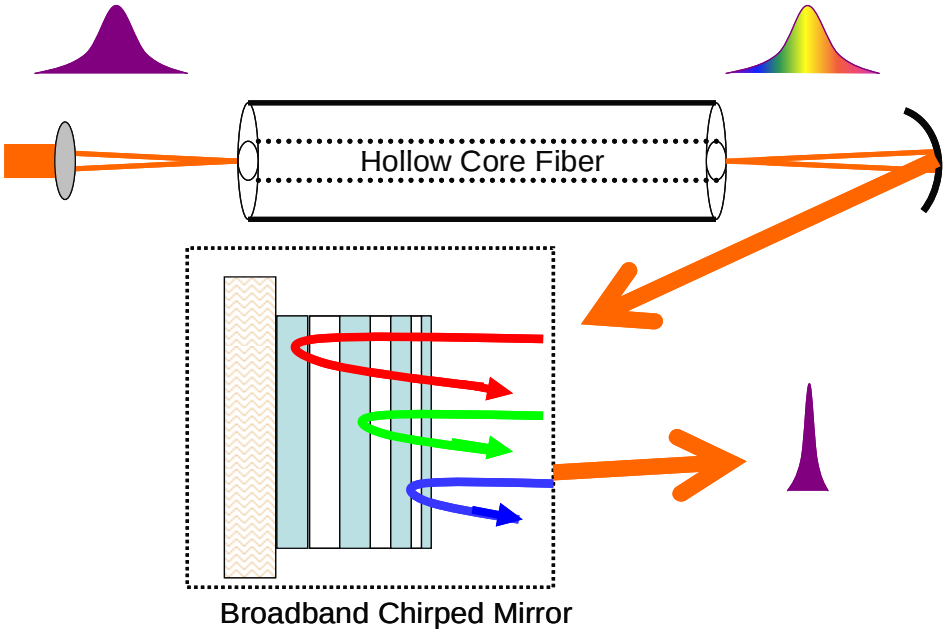

Figure 2.1. Experimental setup for generating few cycle pulses. Laser pulses of duration 33-fs and energy up to 1.5-mJ were focused using a lens of focal length 1m onto a Hollow Core Fiber of inner diameter 400 μm and length 0.9 m. The exit beam was collimated with a concave mirror of focal length 2.5m and compressed using broadband chirped mirrors.

Schematic representation of the hollow fiber/chirped mirror compressor is shown in Figure 2.1. The detail of the light source itself and its beam line to this setup are shown in Appendix A. Beam 2 from KLS was passed through a zero-order achromatic quarter wave plate in order to change the polarization state of the beam from linear to circular and vice versa. The field strength of the input circularly polarized pulses was equal in all directions with an error of $\pm$ 5%. The laser beam was focused by a plano-convex lens with a one meter focal length. The inner diameter of the hollow-core fiber was 400 μm and its length was 90 cm. The fiber was placed on a v-grooved aluminium rod kept in a pressurized chamber which was filled with Ar or Ne gas. By properly mode matching the input beam to the hollow fiber, we measured the throughput of 70-80% (after taking in to account of loss of reflection at the windows) was measured for both circular and linear polarization of the input at the condition when the fiber was evacuated. A wedge plate, mounted on a flipper mount, was used for reflecting a part of the output beam to a CCD camera for monitoring the spatial profile. One of the measured spatial profiles of the output beam was as shown in figure 2.2. The inner circle is drawn to enclose a fundamental EH_{11} mode and the outer circle encloses the complete beam profile including higher order modes. While measuring the energy, we assumed the central area of the profile covering 90% of the total energy as the fundamental mode.

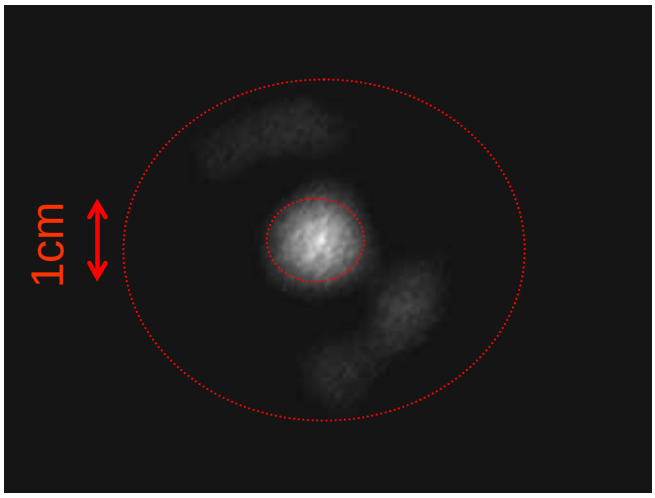

Figure 2.2. Measured beam profile of Hollow Fiber output. The outer circle encloses the full profile and the inner circle encloses 90 % of the energy of the whole profile.

The transmitted beam from the wedge plate was passed through an iris in order to control its beam size onto the power meter. The total power of the beam was measured when the iris was wide open and the power at the fundamental mode was measured when the iris was open only up to the inner circle (corresponding to the inner circle). In order to avoid the effect of laser power fluctuations in the power measurement, the input and output power were measured at the same time. This was done by splitting a few percent of the input beam and reflecting it to another power meter of the same model. Measurement was also averaged over 30 seconds using acquisition controlled by LabVIEW routines.

The input laser power and pressure of Ar gas in the hollow core fiber were optimized precisely for obtaining a sufficiently broader spectrum with a good spatial profile. Let us do a very crude estimate of the spectral broadening using 1 mJ of linearly polarized pulses of duration 33-fs in Ar gas at pressure 0.5 bar. The chirp parameter is defined as [24]:

$$b = \frac{4\pi a n_2 IL}{\lambda_o} \tag{2.1}$$

where, $a\left(=\frac{2\ln 2}{\tau^2}\right)$ is the pulse duration parameter for duration of pulse τ, n_2 is the non-linear index of refraction (its origin is described later in chapter 2.4), I is the intensity of the laser, *L* is the interaction length, and λ_o is the center wavelength of the laser. The ratio of the non-linear index of refraction of Ar gas to its pressure p is given as [15]: n_2/p = 9.8 x 10^{-20} cm^2/W-bar, and the other parameters are: τ = 33fs, λ_o = 0.78 μm, C = 0.3 $\mu m/fs$, L = 0.9 m.

Approximating the size of the beam at the entrance of the fiber as equal to its inner diameter which was 400 μm, the peak intensity of the laser was equal to 2.8 x 10^{13} W/cm^2. Using these numbers in equation 2.1 provides b = 0.011 fs^{-2}. The bandwidth after self phase modulation can be written in terms of input bandwidth as [24]:

$$\Delta f_{spm} = \Delta f_{input}\sqrt{1+\left(\frac{b}{a}\right)^2} \tag{2.2}$$

$$\Rightarrow \quad \frac{\Delta f_{spm}}{\Delta f_{input}} = 7.2$$

This implies that under these experimental conditions the spectrum should be broadened due to self phase modulation ~ 7 times that of the input spectrum. The width of the measured input spectrum was ~70 nm at $1/e^2$ of its peak value and that of the output spectrum was ~ 350 nm at $1/e^2$ as shown in Figure 2.3 which showed ~5 times spectral broadening. One of the main causes of the discrepancy between measurement and calculation is attributed to the fact that here in the calculation we considered a peak value of intensity, but in the measurement, most of the volume in the fiber has a much lower value of intensity. The measured spectrum was capable of supporting a transform limited pulse as short as 5-fs.

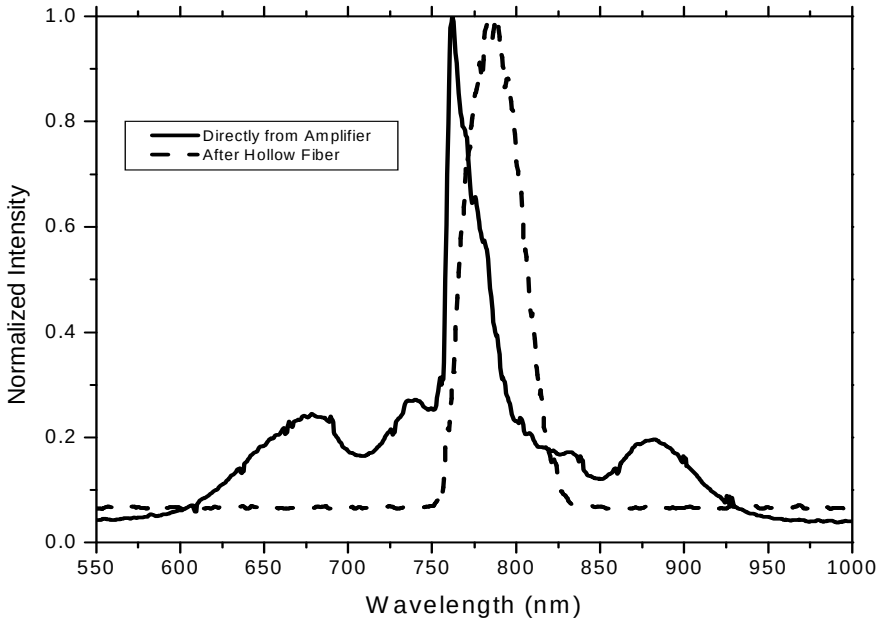

Figure 2.3 Measured spectra before and after self phase modulation. The dotted line represents the spectrum measured directly after the CPA, and the solid line represents the spectrum measured after the fiber.

The spectrally broadened pulses emerging from the fiber were compressed using the chirped mirrors. The beam was reflected back and forth on two broadband chirped mirrors. The total number of reflections was 6, which introduced a GVD of ~-300 fs^2. The amount of negative GVD introduced by the chirped mirrors was sufficient to compensate the self-phase modulation inside the fiber and the material dispersion from the output end of the fiber to the FROG. The dispersion included the exit window of the fiber chamber (0.5 mm of fused silica), 5 meters of air from the exit of the fiber to the FROG setup, a beam splitter of thickness 1.5 mm inside the FROG, and 0.5 mm of fused silica plate placed at the input of the FROG. The thickness of the plate was chosen to yield the shortest pulse. The direction of the beam was kept perpendicular to the chirped mirrors to ensure similar compensation on both s and p components of the circularly polarized pulse. After the chirped mirror, the beam was collimated with a concave mirror with a radius of curvature of 5 meters which resulted in a final beam size of ~1cm in diameter. The input laser power and pressure of Ar gas in the fiber were optimized by observing the measured spatial profile, spectrum of the pulse, and the FROG trace.

2.3 Measurement of Few Cycle Pulses

The experimental setup of SHG-FROG for characterizing few cycle pulses is shown in Figure 2.4. The beam intended for characterization was first split evenly into two parts with a broadband 50/50 beam splitter (part number BBS-790-45S-PW-1006-UV, CVIlaser) The reflected beam, after passing through a compensating plate, and the transmitted beam, were reflected off the silver mirrors M1, M2, M2 and finally overlapped spatially as well as temporally onto a nonlinear medium of a BBO crystal [10 mm x 10 mm x 0.01 mm, BBO Type I, $\theta = 29.2^o$, $\varphi = 90^o$, EKSMA Co.].

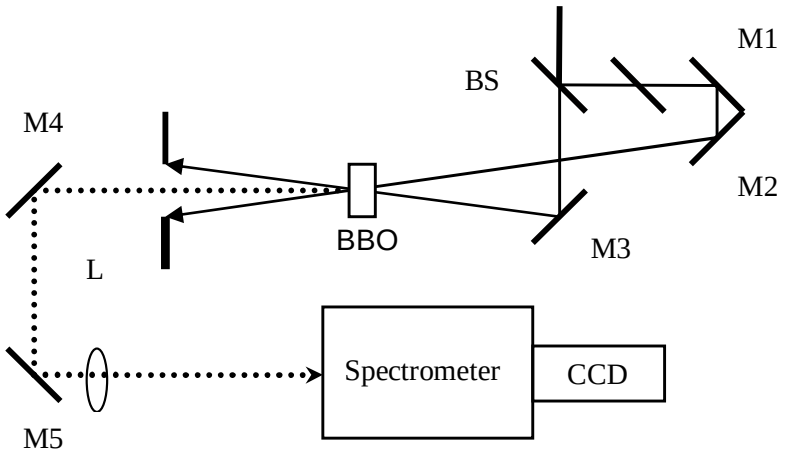

Figure 2.4. Schematics of FROG setup for measuring few cycle pulses. M1, M2 and M3 are silver mirrors, BS is a 50/50 beam splitter, L is a planoconvex lens of focal length 25 cm, M4 and M5 are aluminum mirrors.

These beams crossed each other at an angle of ~1 degree at the position of the crystal. An iris was used to spatially select the second harmonic signal perpendicular to the crystal surface. An infrared filter BG40 was used to filter out the residual fundamental beam. The second harmonic signal was then led to a spectrometer by reflecting off the aluminium-coated mirrors. A UV-CCD camera [Part Number, QICAM-UV, and Model number QIC-F-M-12-UV, Qimaging Inc.] was installed following the spectrometer as a detector. The BBO crystal was imaged with a lens of focal length 250 cm with one half of the demagnification onto the entrance slit of the spectrometer. Finally, a commercially available FROG algorithm (Femtosoft Technologies Ver. 3.1.2) was used to reconstruct the pulse shape from the measured FROG trace. The retrieved spectrum was compared with the measured spectrum obtained with a calibrated spectrometer in order to check the validity of the measurement.

Characterization of the laser pulses directly from the amplifier was relatively easier. The FROG-reconstructed spectra obtained by using a $10\,\mu m$ thick BBO crystal as the non-linear medium were in reasonably good agreement with the measured spectrum even without correcting the spectral response of the detector as shown in Figure 2.5(a). This was due to the relatively

narrower spectral width of the pulses directly from the amplifier. However, characterization of few cycle pulses which had a much broader bandwidth as a result of self phase modulation was still a challenge. One of the poor reconstructions, for example, is shown in Figure 2.5(b), where the reconstructed spectrum is significantly different from the directly measured one.

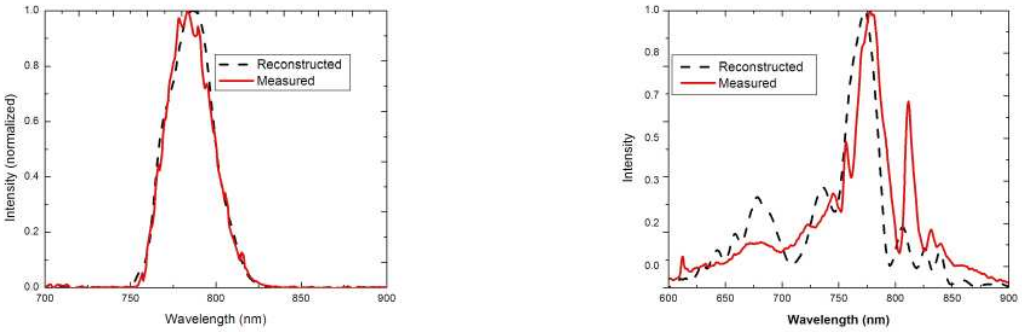

(a) (b)

Figure 2.5 Reconstructed and directly measured spectra. The solid line represents the spectrum measured with a calibrated spectrometer and the dashed line represents the spectrum reconstructed with the FROG algorithm (a) directly after CPA and (b) after hollow fiber and chirped mirrors.

We realized that in order to accurately characterize “few cycle” pulses it was required to consider (i) a non-linear medium which has a flat spectral response within the range of the broad spectrum; (ii) the spectral response of the detector; (iii) broadening of the pulse due to dispersion in the non-linear medium and (iv) spectral response of all the optics before the nonlinear medium. We corrected the spectral response of our detector, which consists of a spectrometer and a CCD camera, using a deuterium lamp and a calibrated spectrometer. A BBO crystal of thickness-5 μm which had a broader phase matching spectral range was used as a non- linear medium. With these modifications we were able to use the SHG-FROG in the few cycle limits. The spectrum obtained from the FROG agreed reasonably well with the directly measured

spectrum as shown in Figure 2.6(a). The reconstructed FROG trace also converged well to the measured trace as shown in Figure 2.6 (b) and (c). These cross checks concluded that the SHG-FROG we designed here was capable of measuring "few cycle" pulses. One of the measured pulse shapes of a 6.2-fs pulse is shown in Figure 2.6 (d), where the solid and dashed lines represent the intensity and phase of the pulse respectively.

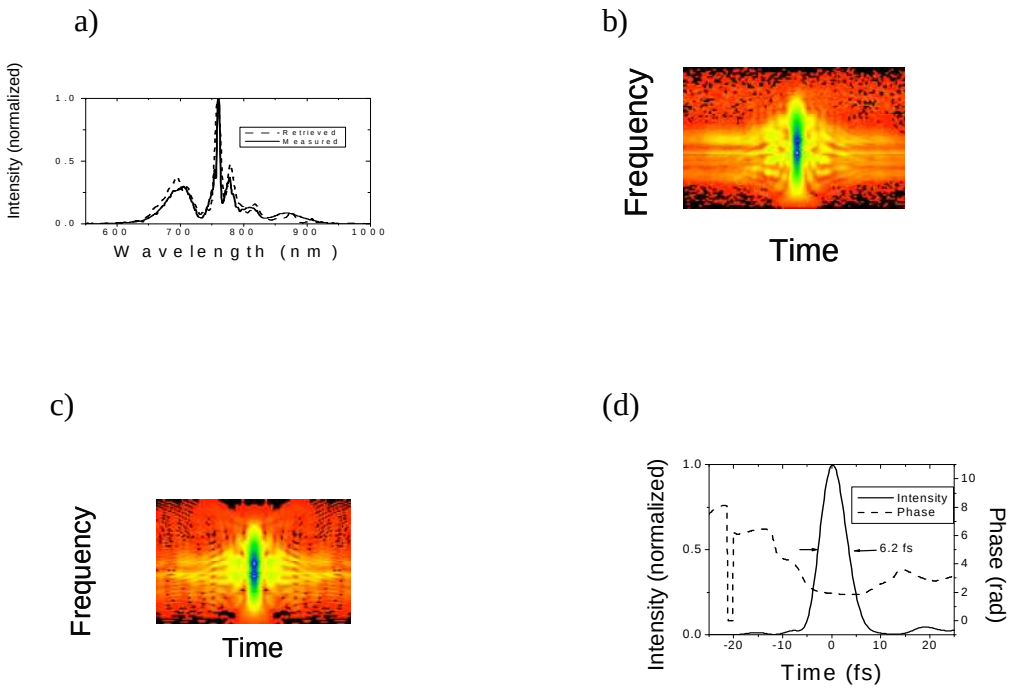

Figure 2.6 Result of measurement of few cycle pulses using FROG. (a) The solid line represents the measured spectrum, and, the dashed line represents the reconstructed spectrum, (b) the measured FROG trace, (c) the reconstructed FROG trace, and (d) the measured pulse shape in time where the solid line is the intensity and the dashed line is the phase. Ar gas of pressure 0.5 bar was used in this measurement.

2.4 Circular Polarization Input for Higher Energy Pulses

In general, the refractive index of a gas medium can be taken as a constant. However, high intensity laser light calls for an additional intensity-dependent term known as the non-linear index of refraction. It introduced a non-linear phenomenon is called the optical "Kerr effect" which can be described as [23]:

$$n(I) = n_0 + n_2 I \tag{2.2}$$

where n_o is a constant, linear part of the index, and the second term is the non-linear refractive index which is a function of the intensity of the laser *(I)*. n_2 is called the Kerr coefficient which has its value in the range of 10^{-20}cm^2/W for noble gases. As the laser intensity is a function of time and space, the total index of refraction of the medium also varies accordingly in presence of high power laser. The change in refractive index due to the Kerr effect is termed as:

$$\Delta n_{Kerr} = n_2 I \tag{2.3}$$

where I is the intensity of the laser, and its spatial profile can be represented by a Gaussian distribution as equation 2.4 [24]. Here, r is the radial distance and w is the radius of the focal spot. When a high power laser is coupled to the hollow fiber, the value of the intensity is maximum in the axial region where r = 0, I(r) = $I_{o,}$ and decreases to the wall, where r = 200 μm causing self focusing of the beam as the beam propagates.

$$I(r) = I_0 e^{-2\left(\frac{r}{w}\right)^2} \tag{2.4}$$

Let us do a quantitative estimate of self focusing in the hollow core fiber. Laser pulses of duration ~33 fs and maximum energy of 1.5 mJ were focused onto the entry of the fiber having a radius of 400 μm. With an approximation of the size of the focus spot equal to the inner diameter of the fiber, these parameters give the peak intensity of the beam inside the fiber equal to 7.2 x 10^{13} W/cm^2.

The value of Kerr coefficient for linear and circular polarization of the laser are n_{2L} = 9.8 x 10^{-20} and n_{2C} = 6.5 x 10^{-20} cm^2/W respectively [15].Thus from equation 2.3 the maximum change of index of refraction for the case of linear and circular polarization due to the Kerr effect are 7.05 x 10^{-6} and 4.7 x 10^{-6} respectively.

Similarly, the temporal profile of the laser also modulates the index of refraction and thus the phase of the pulse in time. The modulation of the phase therefore introduces new frequencies in the spectrum. This is the key for this spectral broadening. But, since both spatial and temporal effects arise from the same order of nonlinearities, one cannot get rid of self focusing and preserve the self phase modulation. Thus, self focusing has to be compensated with some other processes giving self defocusing of the beam for the same medium.

Another phenomenon contributing towards the change in refractive index of the medium for a high intensity laser is the laser-induced ionization of the medium due to multiphoton and tunnelling processes depending upon the intensity of the laser. Once the ionization occurs, the electrons are produced, resulting in plasma formation along the beam propagation. So, the index of refraction is modified in the region where the plasma is formed in the following way:

$$n = n_o - \frac{N_e}{2N_{cr}} \tag{2.5}$$

where N_{cr} is the critical electron density and is equal to $10^{21}\lambda^{-2}$ cm^{-3} where λ is in μm. For $\lambda = 0.780\ \mu m$, N_{cr}=1.64 x 10 ^{21} cm^{-3}. N_e is the free electron density. Again, $N_e = PN_{gas}$, where P is the ionization probability and N_{gas} is the number density of the gas. $N_{gas} = \rho \frac{N_{avo}}{M}$. ρ is the gas density (equal to 1.67 kg/m^3 for pressure of 1 bar and temperature of 15 ^{o}C), N_{avo} is Avogrado's number (6.022 x 10^{23} atoms per gram-mole) and M is the atomic mass equal to 39.9 amu for Ar. So, the change in refractive index due to ionization is:

$$\Delta n_e = \frac{N_e}{2N_{cr}} = \frac{PN_{gas}}{2N_{cr}} \tag{2.6}$$

This implies that even if only 1% of the gas is ionized by the laser, the change in the index of refraction (Δn_e) is equal to 1.9 x 10^{-4}, which is still 2 orders of magnitude bigger than the change due to the Kerr effect. Thus, as the high intensity laser propagates in the fiber, the effect of ionization greatly dominates in changing the refractive index of the gas.

In the experiment we studied the effect of ionization due to the laser while propagating in Ar gas, in the cases of both circular and linear polarizations. We measured (i) total output energy; (ii) output energy at the fundamental mode only; (iii) spatial profile of the beam; and (iv) resultant spectrum for both states of polarization. First, in the absence of any non-linear medium, i.e. when the fiber was evacuated, it was found that the total output power scaled linearly with the input power in both circular and linear polarization as shown in Figure 2.7 (a), and the spatial profile did not degrade with the higher power. Then, the fiber was filled with Ar gas with pressure of 0.5 bar, and the measurements were repeated accordingly. We found that at the lower input energy, the output energy again scaled linearly with the input, and the spatial profile did not degrade for both polarization states. However, for higher input energy limits the story became interesting. As we increased the input energy up to 1.5 mJ we found that the outputs did not scale linearly any more, and in addition to that the spatial mode also started to degrade. We

defined the mode as “degraded mode” if the energy inside the inner circle of the mode (Figure 2.2) contains less than 90% of the total energy of the beam. We called it a “threshold mode” if that energy is just 90% for the highest input power. In another words, at this mode the system can deliver the highest energy output keeping good spatial profile.

Figure 2.7 (b) shows the deviation of total output energy from linear scale at the higher energy limit for both polarization states of the beam. When we measured the energy of the fundamental mode relative to the total energy of the output beam as shown in Figure 2.7 (c), we found that the “threshold mode” was at 0.9 mJ of input energy in the case of linear polarization. However, this limit reached 1.4 mJ in the case of circular polarization, leading to 0.79 mJ of corresponding output energy at the fundamental mode as shown in Figure 2.7 (e). This output energy was 1.5 times higher than that with the linear polarization state. The spectra of the output pulses were comparable for the two polarization states when the output energies were close to the “threshold mode” for the linear input, i.e. 0.9mJ. More interestingly, the measured spectrum of the circularly polarized pulses at its “threshold mode”, i.e. at 1.4mJ, was much broader than that of the linear pulses at their “threshold mode”, as shown in Figure 2.7 (d), which supported a shorter pulse as characterized in chapter 2.2.2. The final output energy of the compressed pulse was 0.6 mJ.

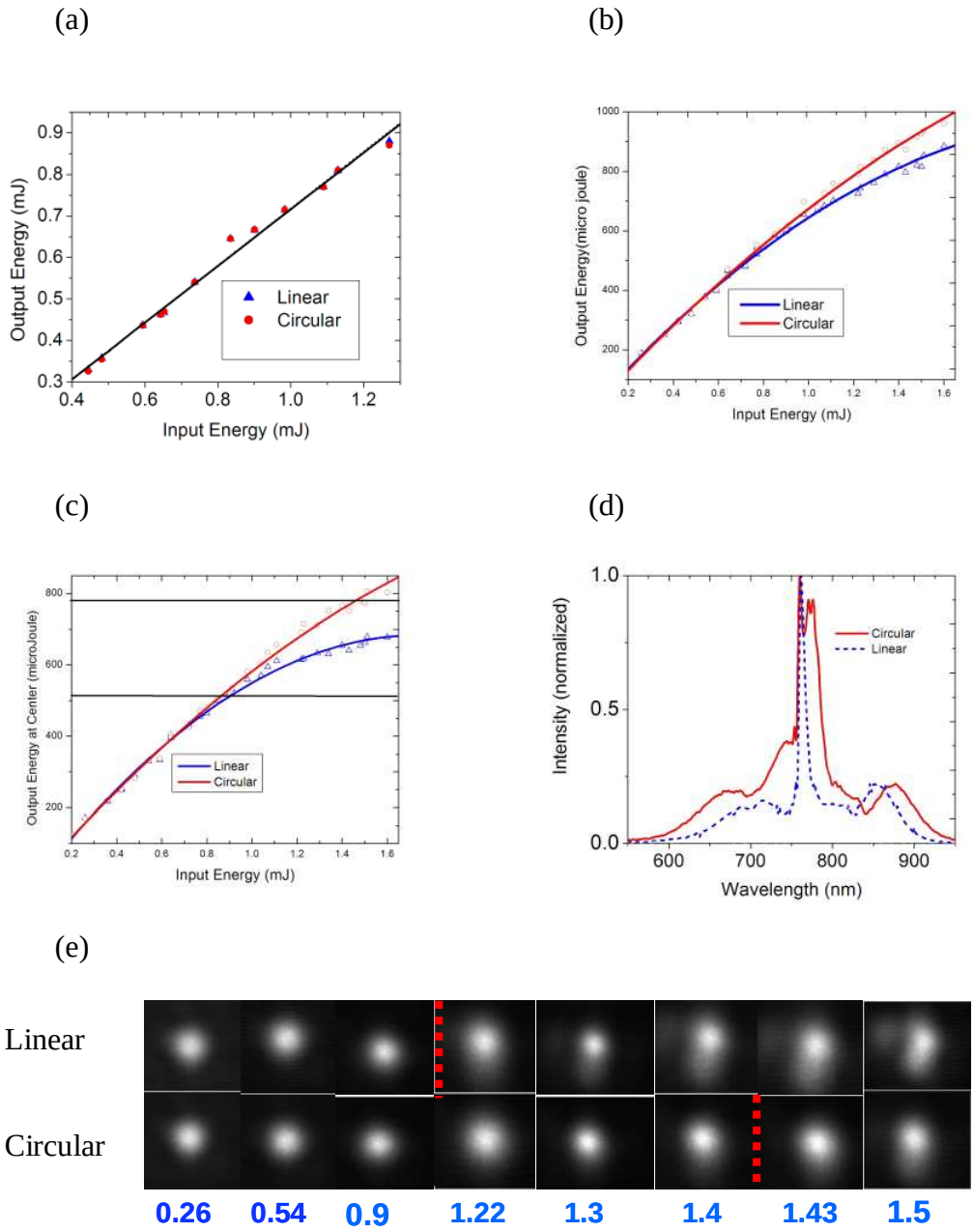

Figure 2.7 Comparison of linear and circular polarization state input. The total output energy is plotted with respect to the total input energy. The triangles and circles are the data points for linear and circular polarization states and the solid lines are fittings (a) when the fiber was evacuated; and (b) when the fiber was filled with Ar gas of 0.5 bar of pressure. The energy inside the fundamental mode is plotted with the input energy (c) for the same gas pressure. (d) The

measured spectrum of output pulse at the threshold input energies where solid and dashed lines are for circular and linear polarization states. (e)The measured beam profiles; the upper row is for the case of linear and lower raw is for the case of circular polarization input. The indicated numbers on the lower part are the corresponding input energies in mJ.

2.5 Result and Other Possibilities

We have demonstrated a simple way to scale up the output energy from the hollow-core fiber/chirped mirror compressor technique. When the fiber chamber was filled with 0.5 bar argon gas, the output energy with circular polarization was 1.5 times higher than that with linear polarization for similar spatial mode and pulse duration. The improvement can be attributed to the reduction of the ionization by using circularly polarized pulses. The maximum energy of the compressed circularly polarized pulses was more than 0.6 mJ, which was the highest energy achieved in argon with pulse duration less than 7-fs. We expect that this idea is effective for other gases, such as neon, so that an even higher energy could be obtained.

In our group, most recently, laser pulses of energy up to ~1 mJ have been obtained even with linear polarization input but using highly laser susceptible Ne gas as the non-linear medium; and thus, we anticipate that with circular polarization input, the energy of output pulse can be increased to ~1.5 mJ.

CHAPTER 3 - Generation of XUV Supercontinuum

3.1 Previous Work on Generation of Single Attosecond Pulses

High order harmonic generation in noble gases has become a well established technique for producing single attosecond pulses. Under an intense linearly polarized laser field, the valence electron in an atom/molecule can tunnel through the coulomb barrier and can oscillate in the field. The freed electron has a certain probability to be driven back to its parent ion and recombine with it to generate an attosecond burst of electromagnetic waves. This process occurs every half cycle of the laser field and produces an attosecond pulse train when the driving pulse has many cycles. The interference of these attosecond pulses results in a frequency comb with an interval of twice the driving field photon energy. When an ultrashort few-cycle driving field is used, the *cutoff* of the spectrum may become a continuum which corresponds to one emission at the peak of the driving field. Previously, an isolated attosecond pulse was obtained by selecting only the *cutoff* of the spectrum.

In 2001, Drescher *et al.* [26] showed the first evidence of an isolated XUV pulse of duration 1.8-fs. In later years, the same group followed the measurement by reporting shorter single XUV pulses: 650-as in 2002 [5] and 250-as in 2004 [27]. Since these pulses were obtained by filtering the *cutoff* of the harmonic spectrum, they were at almost fixed wavelength with a very small range of tuning ability. For time-resolved absorption spectroscopy, it is desirable to have a "*white light*" source that covers the broad, more intense plateau region of the harmonic spectrum. The broader spectrum supports the possibility of producing an even shorter pulse capable for probing electron dynamics. For producing such a supercontinuum, the duration of the driving pulse must be less than one optical cycle, which is very difficult to develop with current technology. To avoid such a technical difficulty, the polarization gating technique was proposed [28]. Here, we implemented this technique for generating an XUV supercontinuum.

3.2 Polarization Gating for Controlling Electron Trajectories

Higher-order harmonic generation (HHG) has been understood as a three-step process [30]. (i) The electron undergoes tunnel ionization. This occurs as the potential barrier of the bound electron in the atoms or molecule gets suppressed as in Figure 3.1 (a) in the presence of sufficiently high intensity laser, i. e. if $I_p < 2\ U_p$, where I_p is the ionization potential of an atom or molecule, and $U_p = E^2 / 4\omega^2$ is the quiver energy of an electron in a laser field of strength E and frequency ω. (ii) The electron acquires kinetic energy as it is driven by the electric field after leaving the atomic core. (iii) The electron recombines with the parent ion with a certain probability as the electric field reverses its direction and emits discrete energy photons. As a result of this phenomenon, over the profile of the laser pulse consisting of many cycles, the generation takes place at approximately every zero crossing of the field. It turns out that the highest energy ($I_p + 3.17\ U_p$) harmonics is produced by the electrons that are released at ~ 0.05 laser cycles after the peak of the electric field, and recombine later at 0.05 laser cycles prior to the following zero crossing of the field [31]. Four of such possible emissions within two laser cycles are shown in Figure 3.1(b). Thus, with multi-cycle laser pulses the ionization and recombination process is repeated periodically leading to not a single, but a train of pulses every half cycle in the time domain. The corresponding spectrum in the frequency domain has peaks separated by twice the laser frequency.

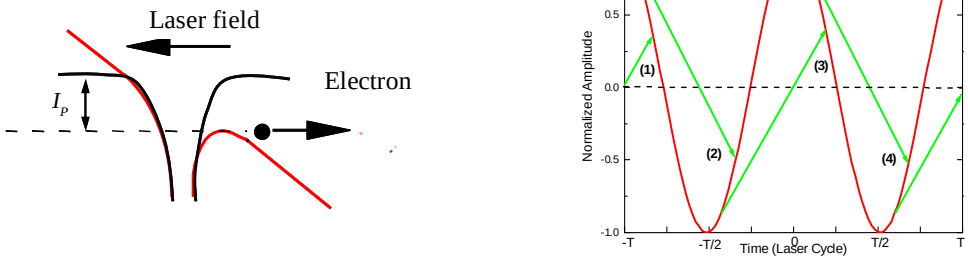

(a) (b)

Figure 3.1. The semiclassical picture of higher-order harmonic generation. (a) The black curves represent the initial Coulomb potential governed by an electron in an atom or molecule. The red curves represent its modified form in the presence of a high intensity laser. The dashed straight line represents the ionization potential. The electron tunnels through the barrier as it is suppressed by the laser electric field. (b) The red curve represents a laser cycle, and the tails and heads of the green straight lines represent one of the emissions and its corresponding recombination for producing highest energy harmonic.

In order to produce a single pulse, *ideally* it is required to turn off all other ionization and/or recombination channels except a single ionization and its corresponding recombination. One way to do that is to use *ideally* a pulse less than one-cycle, but in practice a few-cycle pulse, where the amplitude of the electric field changes dramatically from one cycle to another. In such cases the ionization corresponding to the highest harmonics is possible only during the single cycle at the peak of the envelope of the pulse for a particular CE phase $\varphi_{CE} = 0$. The single ionization at the peak of the pulse and its corresponding recombination results in a continuous spectrum at the *cutoff* of the harmonics. This continuous part of the spectrum, if filtered out, is in fact a single attosecond burst. However, one of the serious disadvantages of this method is the

very limited bandwidth of the attosecond pulse. In order to extend the bandwidth of such attosecond pulse, here we study the method of polarization gating.

In this method we used polarization of the laser for controlling the trajectories of the electrons after leaving the atomic core. When a transverse component of the electric field is introduced in the driving pulse, the electrons start to gain additional momentum in that direction as soon as they leave the atomic cores and thus while returning they most likely miss the parent ion, depending upon the amplitude of the transverse component of the electric field. The electric field of an elliptically polarized beam propagating along the $\hat{y}$ direction can be written as:

$$\vec{E}(t) = \hat{z}\,E_{oz}\cos\omega t + \hat{\mathrm{x}}\,E_{ox}\sin\omega t \tag{3.1}$$

where E_{oz} and E_{ox} are the amplitudes of the electric fields along the $\hat{z}$ and $\hat{x}$ directions.

The ellipticity of such a beam is defined as:

$$\xi = \frac{E_{ox}}{E_{oz}} \tag{3.2}$$

For laser intensity ~10^{14} W/cm^2, ξ ~0.1 can produce a transverse displacement of ~10 -15^{o}A [32] on an electron when it returns, thus the recombination with the parent ion might be prohibited as shown in Figure 3.2 (a). In our measurement we varied the ellipticity of the laser pulse by rotating a half wave plate over a fixed quarter wave plate placed on a linearly polarized beam. The intensity of the 45th harmonic was measured for various ellipticity for randomly oriented Ar atoms, and it was found that the signal dropped by an order of magnitude as the ellipticity was increased to 0.2, as shown in Figure 3.2 (b). Then, it allowed us to assume that the recombination is prohibited, and therefore no harmonics are produced for laser pulses having ellipticity equal to or greater than 0.2. This is the key for using polarization gating to produce a single attosecond pulse.

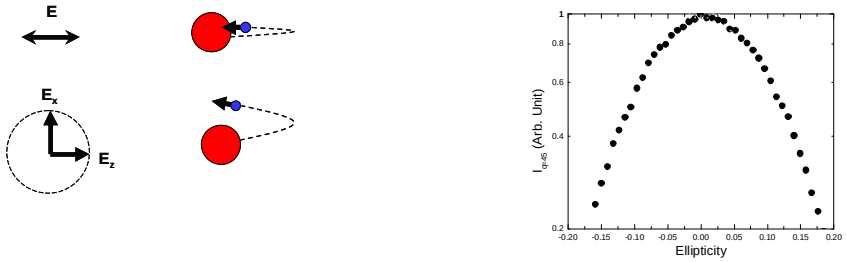

(a) (b)

Figure 3.2 Using laser polarizations for controlling trajectories of the electrons. (a) In the case of a linearly polarized laser field, the electron is driven back towards the parent ion; but in the case of a circularly polarized laser field, the electron is driven away from the parent ion. (b) Measured harmonic signal for 45 th harmonic by changing the ellipticity of the laser.

It was proposed that a pulse with its polarization changing from circular to linear and then to circular again can be constructed by combining a left circularly polarized pulse and a delayed right circularly polarized pulse [33] as shown in Figure 3.3 (a) and (b). The expression for the electric field of a left circularly polarized light which arrives at time $T_d/2$ earlier than a reference time and propagates along the $\hat{y}$ direction can be written as:

$$\vec{E}_l(t) = E_0 e^{-2\ln(2)\left((t-T_d/2)/\tau_p\right)^2}\left[\hat{z}\cos(wt+\varphi)+\hat{x}\sin(wt+\varphi)\right] \tag{3.3}$$

Similarly, that for a right circularly polarized light which arrives at time $T_d/2$ later than the reference time and propagates in the same direction can be written as:

$$\vec{E}_r(t) = E_0 e^{-2\ln(2)\left((t+T_d/2)/\tau_p\right)^2}\left[\hat{z}\cos(wt+\varphi)-\hat{x}\sin(wt+\varphi)\right] \tag{3.4}$$

where, E_o is the peak field amplitude, τ_p is the duration of the pulse, φ is the CE phase of the pulse, and T_d is the time delay, which is an integer multiple of the laser cycle. These two expressions can be combined to represent the electric field of the composite pulse:

$$\vec{E}(t) = \hat{z}\,E_0\left[e^{-2\ln(2)\left((t+T_d/2)/\tau_p\right)^2} + e^{-2\ln(2)\left((t-T_d/2)/\tau_p\right)^2}\right]\cos(wt+\varphi) + \hat{x}\,E_0\left[e^{-2\ln(2)\left((t-T_d/2)/\tau_p\right)^2} - e^{-2\ln(2)\left((t+T_d/2)/\tau_p\right)^2}\right]\sin(wt+\varphi) \tag{3.5}$$

According to the above described definition of ellipticity we can write the time dependent ellipticity of the composite pulse as:

$$\xi(t) = \frac{\left|\left[e^{-2\ln(2)\left((t-T_d/2)/\tau_p\right)^2} - e^{-2\ln(2)\left((t+T_d/2)/\tau_p\right)^2}\right]\right|}{\left|\left[e^{-2\ln(2)\left((t-T_d/2)/\tau_p\right)^2} + e^{-2\ln(2)\left((t+T_d/2)/\tau_p\right)^2}\right]\right|} = \frac{\left|1-e^{-4\ln(2)\left((t+T_d/2)/\tau_p\right)^2}\right|}{1+e^{-4\ln(2)\left((t+T_d/2)/\tau_p\right)^2}} \tag{3.6}$$

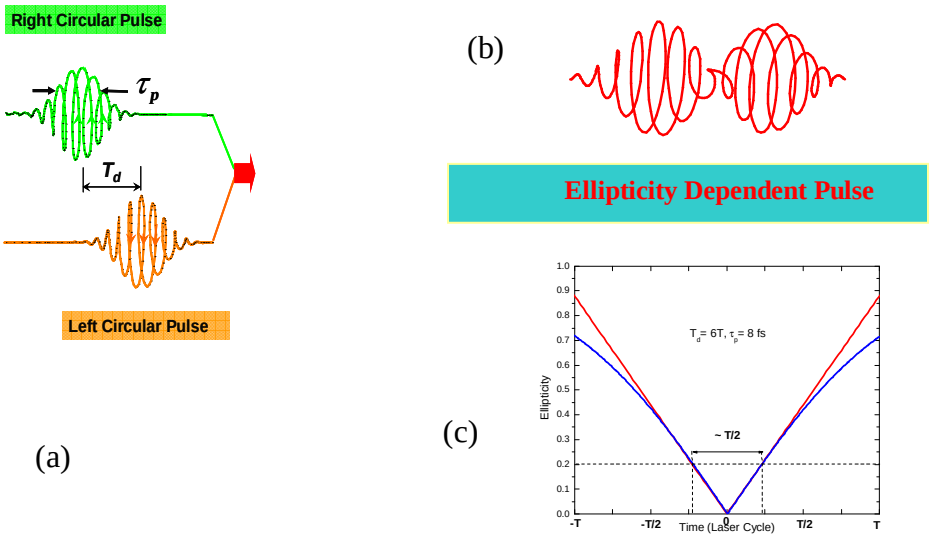

Figure 3.3 Principle for producing ellipticity varying pulse. (a) Left and right circular pulses are delayed with respect to each other. (b) They are combined and formed an ellipticity varying

pulse. (c) The ellipticity is plotted with respect to time. The blue curve plots the exact values and the red curve is an approximation.

The time dependent ellipticity from equation 3.6 is plotted in blue in Figure 3.3 (c) for the value of T_d = 6 laser cycles and τ_p = 8 fs. It is found that the amplitude of ellipticity is less than 0.2 for the duration of *a half cycle* near t = 0. At this time limit, an approximation $\xi(t) \approx \left| 2.\ln(2) \frac{T_d}{\tau^2_p} .t \right|$ is tested by plotting in red in Figure 3.3 together with the exact expression in blue. It indicates that the approximation is excellent in the limit of $\xi(t) \leq 0.2$ which leads to a simple and user friendly physical relation:

$$\tau_{eff} = 0.3 \frac{\tau^2_p}{T_d} \tag{3.7}$$

where τ_{eff} is the *gate- width* which allows harmonic emission. It should not be much longer than a half cycle to ensure a single recombination only. Using this relation, a proper delay, T_d can be calculated for a given pulse duration, τ_p or vice versa to calculate the *gate-width,* τ_{eff} .

Experimentally, such an ellipticity varying pulse was constructed using birefringence optics by a unique method as illustrated in Figure 3.4. The linearly polarized input pulse was evenly divided by a quartz plate into an o-ray and an e-ray by setting the optic axis of the quartz plate 45 degrees with respect to the input polarization. Therefore, two pulses with orthogonal polarizations were formed. Because of the birefringence property of the quartz, the o-pulse and e-pulse travelled at different group velocities v_o and v_e in the plate. After passing through the plate, the o-pulse and the e-pulse were separated in time. The delay was proportional to the plate thickness L. The pulse durations of the two pulses were almost the same because the difference of the group velocity dispersion is small in the two polarization orientations. After the quartz plate, a quarter wave plate was placed with its optic axis along the initial input laser polarization direction. This plate converted the o-pulse and e-pulse into left- and right-circularly polarized

light. The superposition of these two pulses produced an ellipticity varying pulse. The method is simple, robust, and almost energy lossless. It avoided the difficulties of spatial and temporal overlap of a Mach-Zehnder interferometer type conventional delay line. Furthermore, there was no additional delay drift induced by the mechanical vibration and the air turbulence of the interferometer.

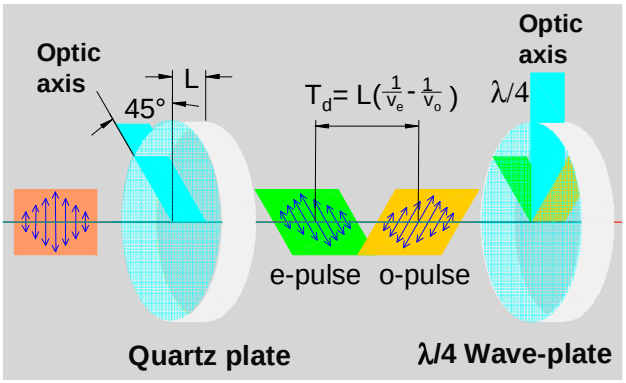

Figure 3.4 Experimental methods for producing ellipticity varying pulse. A quartz plate was set with its optics axis 45 degrees to the initial laser polarization direction and a quarter wave plate was set along the initial laser polarization direction.

3.2 Experimental Setup for generating XUV Supercontinuum

Figure 3.5 shows the experimental setup for generating an XUV supercontinuum using the ellipticity varying pulse. Part of the output beam from the *Kansas Light Source* laser system was focused into a hollow-core fiber with a lens of focal length 1m. The fused silica fiber had an inner diameter of 0.25 mm and a length of 1.6 m. It was filled with Ar gas with a pressure gradient from ~ 10^{-1} Torr at the laser entry to ~ 1 atm at the exit. The collimated output beam from the fiber was apertured to a beam size of ~ 8 mm to block the ring structure of the high-

order modes. The pulse passed through two pairs of chirp mirrors and became negatively chirped with a center wavelength at 750 nm. This chirp was compensated by a fused silica compensating plate so that the pulse duration became tunable by adjusting the plate thickness. The ellipticity varying pulse was then produced with a delay of 15 fs induced by a 0.5 mm quartz plate. Finally the pulse was focused by a parabolic mirror (f = 250 mm) into an argon gas jet with a local density of ~ $10^{18}/cm^3$. The pulse energy was ~ 260 μJ which yielded an intensity of ~1.5×10^{14} W/cm^2 on the target for the linear portion of the pulse. The generated HHG signal, after being separated from the fundamental by an Al filter, was reflected by a grazing incident mirror and dispersed by a transmission grating (2000 l/mm), and recorded by a microchannel plate detector and a cooling CCD camera.

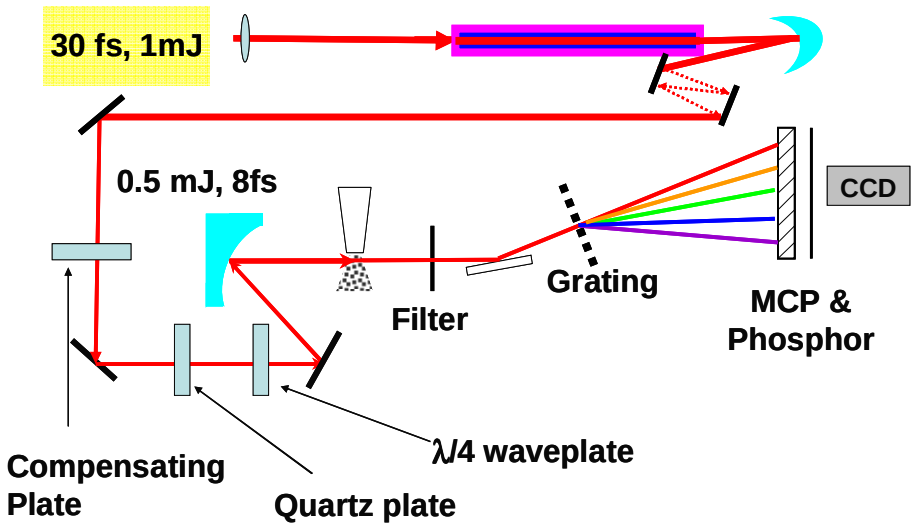

Figure 3.5 Overall system layouts for XUV supercontinum generation. 0.5 mJ of 8fs pulses were focused by a parabolic mirror onto the Ar gas jet. The fundamental beam was filtered out, and the harmonics were then dispersed using a grating on to the MCP/Phosphor. A cooled CCD camera recorded the spectra.

3.3 Result and Other Possibilities

The harmonic spectra were measured for different values of the *gate width* (τ_{eff}) in order to find the shortest width to allow a single recombination and thus produce an XUV supercontinum in the *plateau* of harmonics. The duration of the initial linearly polarized pulse (τ) was measured with FROG as a function of the compensating plate thickness as shown in Figure 3.6 (a). The pulse duration could be tuned from 15-fs to 8-fs. Keeping the delay (T_d = 15-fs) fixed, the harmonics spectrum was measured for several pulse durations (τ) as shown in Figure 3.6 (b). The measured HHG spectra from (i) to (vii) were for the compensating plate thicknesses of 2.3, 2.5, 2.8, 3.0, 3.3, 3.5, and 3.7 mm respectively. In first picture from top (i) the seed pulse duration was of duration ~ 9 fs and the estimated polarization gate was relatively wide ~ 1.6 fs. Therefore the HHG spectrum peaks were still resolved in that case. By decreasing input pulse duration with increasing the plate thickness, the HHG peaks gradually merged as shown in subsequent sections in the picture. In the fourth picture (iv) the thickness of the fused silica fully compensated the frequency chirp, resulting in an 8-fs input pulse and a ~1.3 fs of *gate width*. The HHG spectrum showed a supercontinuum from ~28 eV to ~50eV corresponding to the harmonic order of 19^{th} to 31^{st}. This result indicates a single attosecond pulse was generated over the *plateau* as well as in the *cutoff* region. Further increasing the compensator plate thickness, the input pulses became longer again. Accordingly, the *gate width* became wider so that the discrete peaks in the HHG spectrum gradually reappeared as we go further down in the picture, which implies multiple re-combination processes happened.

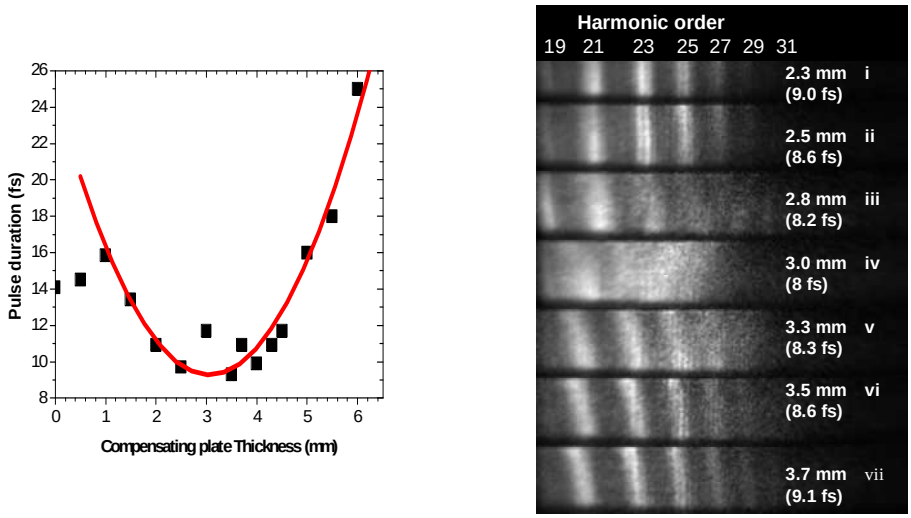

(a) (b)

Figure 3.6 Measured XUV supercontinuum at HHG plateau and cutoff. (a) Measured input pulse duration vs. compensating plate thickness. The red line is the curve fitting of the measured points in the black squares. (b) (i) to (vii) are measured HHG spectra with the compensating plates of different thickness (i) 2.3 mm; (ii) 2.5 mm; (iii) 2.8 mm; (iv) 3.0 mm; (v) 3.3 mm; (vi) 3.5mm, and (vii) 3.7 mm. The corresponding input pulse durations were labelled in the figure.

The lineout of the spectra in Figure 3.6(b)(i) and (iv) are shown in Figure 3.7 (a) and (b) respectively. Their corresponding Fourier transforms with an assumption of their flat phase are shown in Figure 3.7 (c) and (d). The discrete spectrum of the first lineout (a) resulted in three attosecond pulses with a time interval of a half cycle of the driving field. The supercontinuum in Figure 3.6 (b) (iv)/Figure 3.7 (b) yielded a single attosecond pulse with the transform limited pulse duration of 190-as as shown in Figure 3.7 (d).

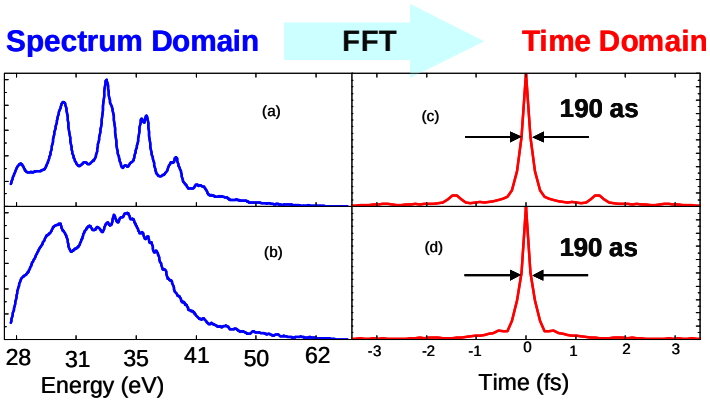

Figure 3.7 Lineout of the measured XUV spectrums and their FFT. (a) Lineout of a discrete energy spectrum (b) lineout of a supercontinuum spectrum (c) FFT of (a) assuming phase flat and (d) FFT of (b) assuming phase flat

In order to support an even shorter single attosecond pulse it is required to further extend the bandwidth of the supercontinuum. One way towards this goal is to extend the *cutoff* of harmonics [34] either by choosing laser parameters or by choosing a gas which is susceptible to ionization by laser. Here, we study another way which is using a mixture of two noble gases having different ionization potentials. In this method, the smaller ionization potential contributed to the lower energy and the higher ionization potential to the higher energy on the supercontinuum spectrum. We used a mixture of Ar and Ne gas as the target and obtained a much broader spectrum. It extended from ~28 eV to ~ 80 eV as shown in Figure 3.8. The lower part of the spectrum containing the discrete harmonic was measured for the purpose of the calibration of the energy spectrum. It was done simply by rotating quartz plate from 45 degrees to 0 degree with respect to the initial laser polarization direction. The intensity of the laser was kept similar by observing the *cutoff* of the harmonic spectrum and controlling the intensity by a reflective neutral density filter. The lineout of the supercontinuum as well as the discrete

harmonics spectra are plotted in Figure 3.9 (a) The Fourier transform of this supercontinuum yielded a single attosecond pulse with the transform limited pulse duration of 60-as as shown in Figure 3.9 (b). This is the broadest XUV supercontinuum reported to date as of our knowledge. We anticipate that upon availability of higher energy few cycle pulses, even broader spectra can be obtained by exciting more laser susceptible gases like He. These measurements were originally done with the laser system without CE phase stabilization. Therefore every spectrum was integrated for a few minutes.

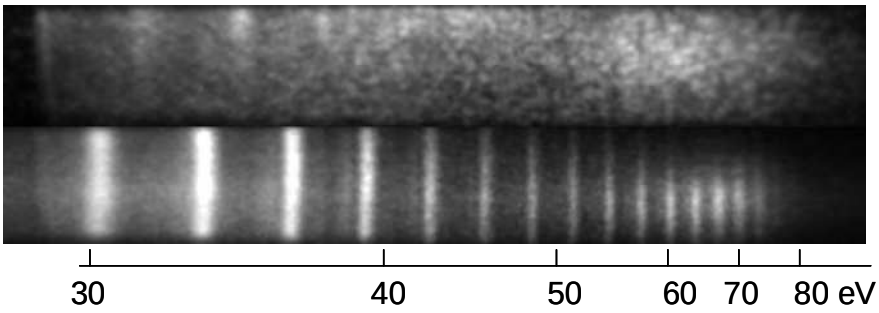

Figure 3.8 Measured XUV supercontinuum using mixed gases. The upper part is the supercontinum on the harmonics spectrum at *cutoff* and plateau from mixture of Ar and Ne gas. The lower picture was the measured discrete harmonics spectrum without polarization gating for calibration purposes.

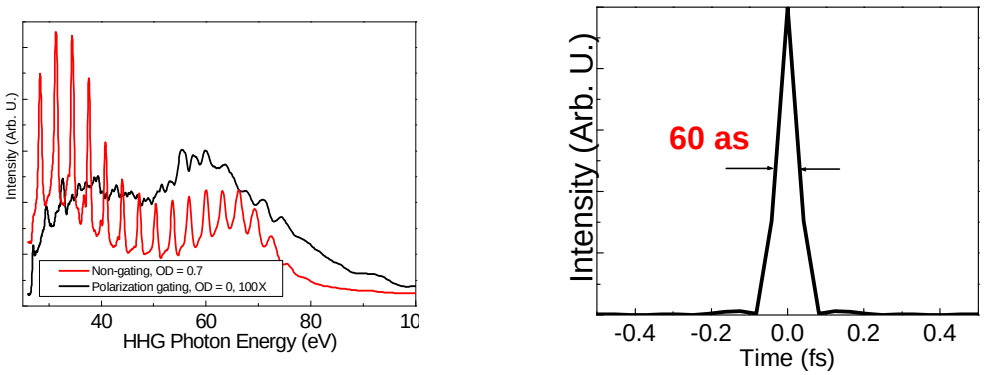

(a) (b)

Figure 3.9 Lineout of the measured XUV spectra from mixed gases and their FFT. (a) The black curve is the lineout of the measured supercontinuum with polarization gating, and the red curve is the lineout of that without polarization gating. (b) FFT of black curve in (a) with assumption that the phase is flat over the entire bandwidth.

CHAPTER 4 - Time-Resolved Measurements

4.1 Motivation for Time-resolved Measurement

Capturing the evolution of microscopic processes in *real time* is generally referred to time-resolved spectroscopy. In this process, the *pump pulse* first drives the system into an excited state, and the *probe pulse* then illuminates the system. By measuring the optical properties of the system, such as absorption of light, the temporal evolution of the microscopic process can be reconstructed. The duration of the pulse and precision in the measurement of delay between the *pump* and *probe pulse* determines the temporal resolution of such measurements. An electron in a Bohr orbit of a hydrogen atom takes ~150 as for completing one rotation. So, a time-resolved measurement for tracking *electron dynamics* in atoms calls for a pulse much shorter than this value. In the previous chapter, we discussed the measurement of the XUV supercontinum and also estimated that these pulses could be as short as 60-as in time. However, a *direct measurement* of these pulses in *real time* is to follow. Knowledge of the amplitude and phase of such pulses are required in order to utilize them for time-resolved spectroscopy.

Standard techniques for characterizing light pulses such as “FROG” cannot be easily adopted for the XUV region. This is due to the lack of suitable optical materials for efficient non-linear processes at the available intensities, and the difficulty of finding suitable optics such as beam splitters. A conventional streak camera is an alternative for the characterization of the XUV pulses but the resolution of this method is currently limited to ~300 fs [11]. Adopting such a streak camera in the attosecond regime called for improving its resolution by orders of magnitude. Let us first discuss in brief the conventional streak camera in order to understand its resolution limit. A pulse subject to the characterization impinges on a photocathode and generates its electron replica. The electron pulse then enters the region of the deflection plates having fast ramping electric field timed with the initial pulse. If the speed (v) of ramp is

comparable to the duration of the electron pulse (Δt) the lateral displacement of the electrons localized at the leading or trailing edge of the pulse are different. Thus the temporal information can be converted to spatial information $\left(\Delta t = \frac{\Delta x}{v}\right)$.Measuring this trace with a position sensitive detector (MCP/Phosphor /CCD) one can reveal the temporal information about the initial pulse. It turns out that the resolution is basically limited by (i) rise time of the deflecting field and (ii) temporal dispersion of the electron pulse during its propagation which no longer mimics the initial pulse.

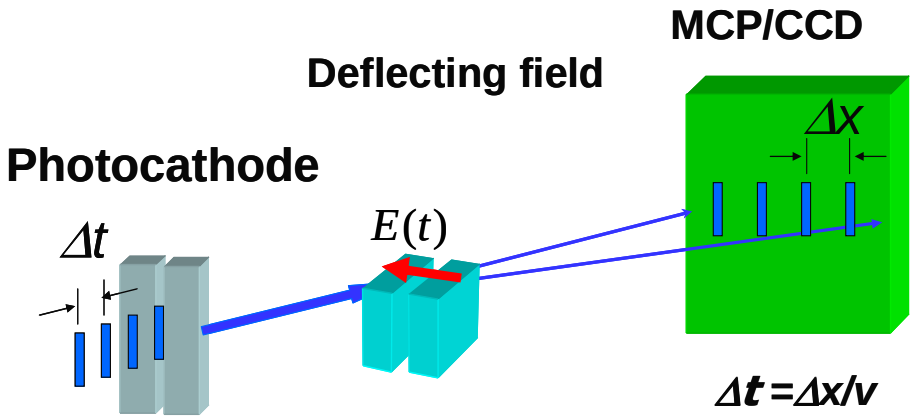

Figure 4.1 Schematic representation of a conventional streak camera. A temporal pulse impinges on the photocathode and produces its electron replica. It is then deflected by the deflecting field onto the detector consisting of MCP/CCD, and recorded as spatial information.

Dramatic modification to the streak camera has been put forward [10] and proposed for its application for the measurement of pulses shorter than 1-fs. The modification includes (i) replacing the traditional deflection plate having electric field rise time of picoseconds with a laser having electric field rise time ~650as; (ii) and replacing the standard photocathode by an atomic gas and placing it directly in the region where the measurement occurs. In this method, by precisely timing the phase of the electric field of the laser with the XUV pulse at the atomic gas

target, the laser assisted photoelectron energy and/or momentum are measured. Finally, by measuring the angular distribution of photoelectrons streaked at different phases of the ellipticity varying pulse in our case, the complete characterization of the XUV pulse as well as the *real time* measurement of the streaking field itself is expected to be revealed. In the following text of this chapter, we start with the principle of the attosecond streak camera, and present some calculations on the momentum shift on the photoelectron spectrum for different phases of the ellipticity varying pulse. We will discuss the experimental detail on the design of the newly built attosecond workstation. Finally, we report our recent progress and the challenges towards the *real time* measurement of attosecond pulses.

4.2 Principle of Attosecond Streak Camera

The XUV pulses to be characterized can imprint their temporal structure on a bunch of photoelectrons by photoionization of atomic gases. Thus, experimentally, their momentum distribution, designated as initial momentum (p_o), can be measured. With synchronized focusing of these pulses with a phase of laser results, a modified final momentum distribution *p(t)* can also be measured in the experiment. Similarly, this final momentum distribution can be directly calculated for a temporal profile of XUV pulses using known laser parameters and delay with respect to the XUV pulse. By iterating the difference between the measured and calculated final momentum distributions and looking for a minimum error, the temporal profile of the XUV pulse can be extracted as proposed by Zhao *et al*. [35].

The motion of a photoelectron in a laser field can be considered independent of the photoionization by an XUV pulse. This motion depends only upon the laser field when the electron is born in the laser field. Thus, this motion can be described by the classical equation of motion:

$$\Delta p = \int_{t_d}^{\infty} \vec{F}(t)dt = -e\int_{t_d}^{\infty} \vec{E}\ (t)dt \qquad (4.1)$$

where Δp is thechange in momentum, $\vec{F}(t)$ is the total force exerted on the electron, $\vec{E}(t)$ is the electric field of the laser, and t_d is the time of birth of the electron at the laser field. The right hand side of the above equation is nothing but the vector potential of the electric field. Thus, for a linearly polarized laser the amplitude of change in momentum of the electron is proportional to the vector potential at the time when the electron is born in the laser field. Because of the negative charge of the electron, the direction of the momentum shift is opposite to the vector potential as shown in Figure 4.2. The maximum up-shift occurs at t_d = T/4, 5T/4 ... etc., maximum downshift occurs at t_d = 3T/4, 7T/4… etc., and the minimum or no shift occurs at t_d = 0, T/2, 2T/2….. etc.

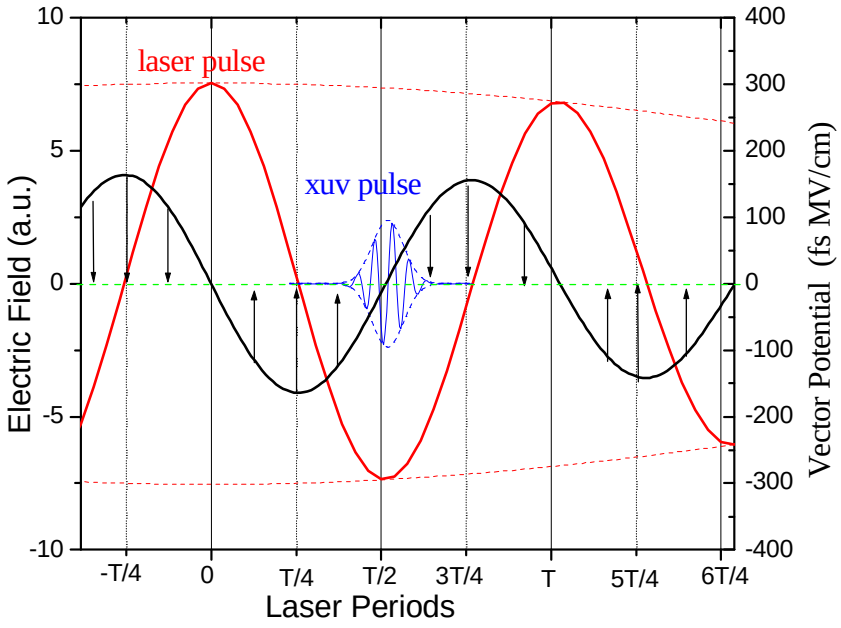

Figure 4.2 Momentum shift on the XUV ionized photoelectron due to the laser field. The red curve represents the electric field of the laser, and the black curve is for the corresponding vector

potential. The up and down arrows represent the direction and amplitude of the momentum shift at the corresponding time when the photoelectrons are born in the laser field.

In an ellipticity varying pulse after the polarization gating, the electric field has more than one component in most parts of the pulse, so the momentum shift is of course more complex in that case. Let us define the geometry of the measurement in order to better describe the momentum shifts. The propagation of the beam was along the y-axis and the detector was perpendicular to the negative z-axis as shown in Figure 4.3.

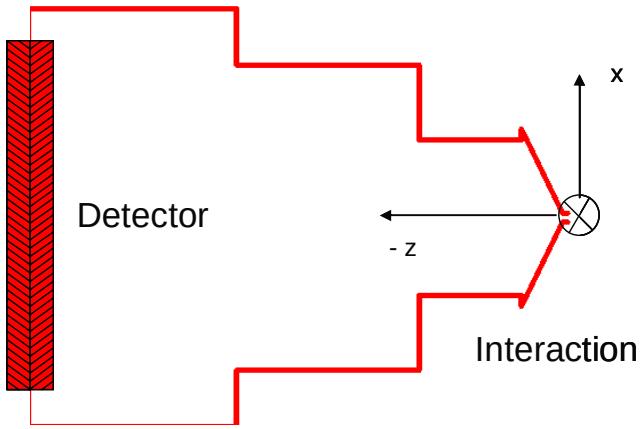

Figure 4.3 Definition of co-ordinates in the measurement.

The electric field of the ellipticity varying pulse from polarization gating can be written as:

$$\vec{E}(t) = \hat{z}\,E_0\left[e^{-2\ln(2)\left((t+T_d/2+T/8)/\tau_p\right)^2} + e^{-2\ln(2)\left((t-T_d/2-T/8)/\tau_p\right)^2}\right]\cos(wt+\varphi) + \hat{x}\,E_0\left[e^{-2\ln(2)\left((t-T_d/2-T/8)/\tau_p\right)^2} - e^{-2\ln(2)\left((t+T_d/2+T/8)/\tau_p\right)^2}\right]\sin(wt+\varphi) \quad (4.2)$$

where τ is the duration of the pulse, T_d is the delay produced by the quartz plate, and T/4 is the delay produced by the quarter wave plate. For the values of τ = 8fs and T_d = 8 fs, two components of the electric fields are plotted in Figure 4.4

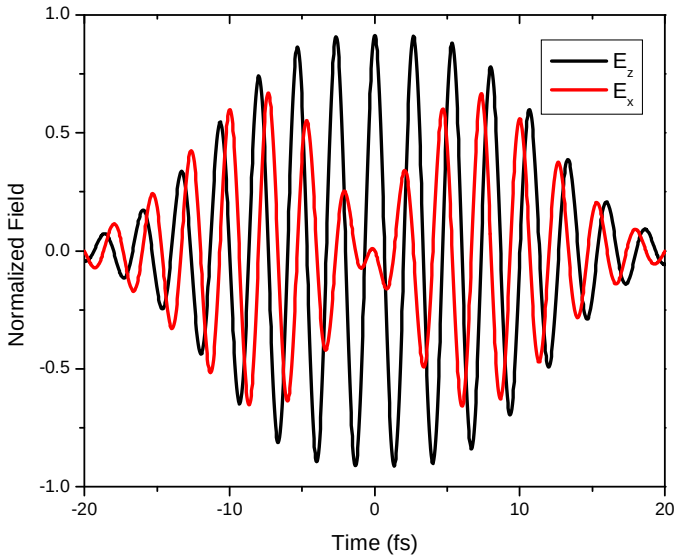

Figure 4.4 Electric field of the ellipticity varying pulse. Black and red components of the field are along z and x directions.

Similar to equation 4.1 a change in momentum along the z direction in this case can be written as:

$$\Delta p_z = \int_{t_d}^{\infty} eE_0 \left[e^{-2\ln(2)\left((t_d + T_d/2 + T/8)/\tau_p\right)^2} + e^{-2\ln(2)\left((t_d - T_d/2 - T/8)/\tau_p\right)^2} \right] \cos(wt + \varphi) dt \qquad (4.3)$$

$$\Delta p_z = \frac{e}{2\pi c/\lambda} \sqrt{I/(1.33\times 10^{-3})} \left[e^{-2\ln(2)\left((t_d + T_d/2 + T/8)/\tau_p\right)^2} + e^{-2\ln(2)\left((t_d - T_d/2 - T/8)/\tau_p\right)^2} \right] \sin\left(\frac{2\pi c}{\lambda} t_d + \varphi\right) \qquad (4.4)$$

The change in momentum along the x direction can also be written as:

$$\Delta p_x = \frac{e}{2\pi c/\lambda}\sqrt{I/(1.33\times10^{-3})}\left[e^{-2\ln(2)\left((t_d+T_d/2+T/8)/\tau_p\right)^2} - e^{-2\ln(2)\left((t_d-T_d/2-T/8)/\tau_p\right)^2}\right]\cos\left(\frac{2\pi c}{\lambda}t_d+\varphi\right) \qquad (4.5)$$

First, a measured XUV supercontinuum was used to calculate the initial momentum distribution for photoionization of Ne atoms as shown in Figure 4.5. The figure (a) represents a complete distribution and (b) represents a part of it that can be measured in the experiment due to the fixed acceptance angle of our detector, which will be discussed later in this chapter. Second, the final complete momentum distribution was calculated for different delays, in every quarter cycle up to 2 laser cycles as shown in Figure 4.6. Finally, the distribution was truncated down to the acceptance angle of the detector as shown in Figure 4.7. A transform limited attosecond pulse of duration 100-as was used in this calculation. With this calculation, it is seen clearly that the attosecond pulse can be used to trace the electric field of light in real time. The detail of the calculation including the code used for this purpose can be found in Appendix B.

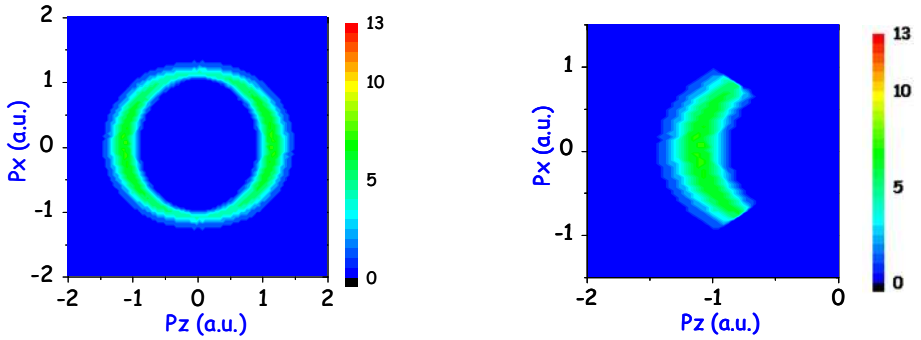

(a) (b)

Figure 4.5 Calculated initial momentum distributions of the photoelectrons. It is the multiple of the measured XUV supercontinuum with the differential cross-section of Ne gas. (a) Complete distribution and (b) A distribution confined by the acceptance angle of the detector.

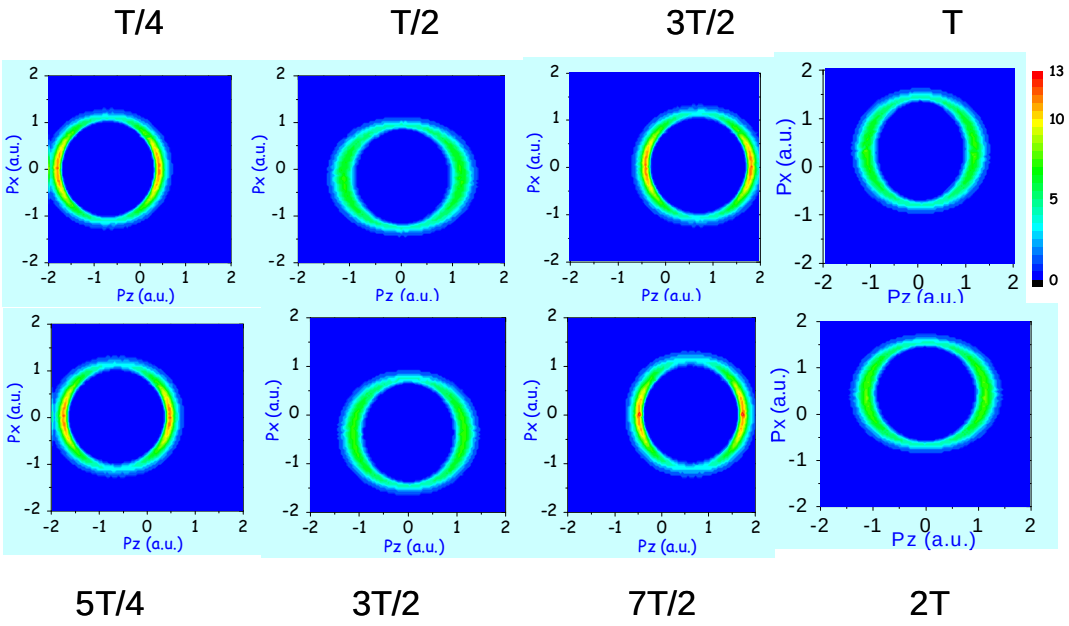

Figure 4.6 Streaking of attosecond pulse of duration 100 as with laser. Every graph shows the momentum distribution of the photoelectron spectrum in the laser field for several t_d. The time of birth was considered every quarter cycle from T/4 to 2T where T= laser cycle.

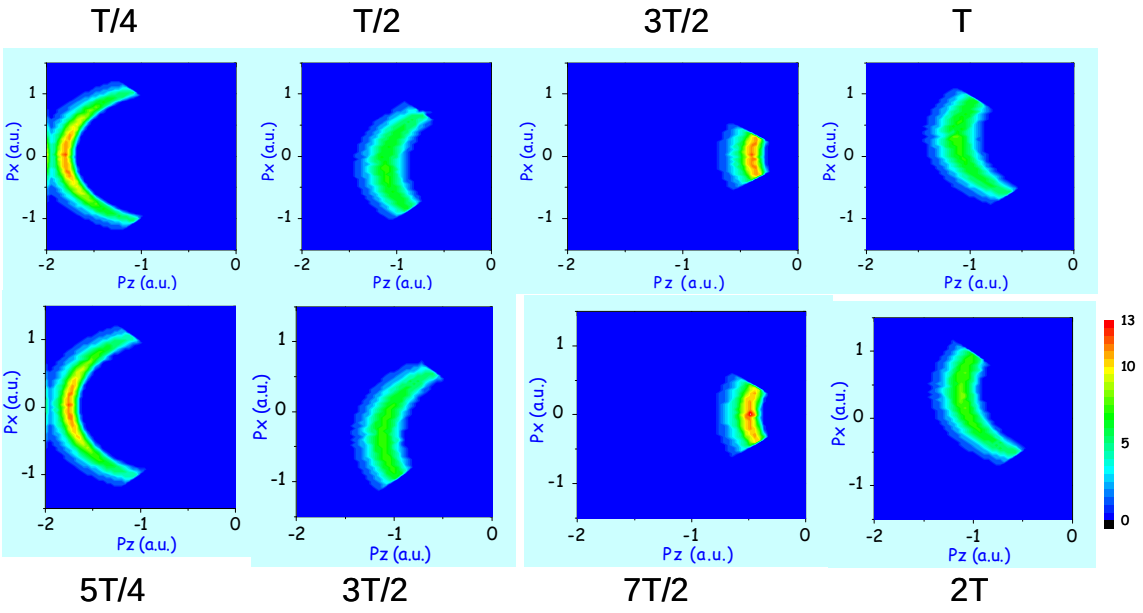

Figure 4.7 Streaking of an attosecond pulse viewed through acceptance angle of 90°. Every graph shows a section of momentum distribution of the photoelectron spectrum in the laser field for several t_d. The time of birth was considered every quarter cycle from T/4 to 2T where T= laser cycle.

4.3 Experimental Setup

4.3.1 Schematics of Experimental Setup

The schematics in Figure 4.8 depict a complete layout of the beam lines and optics in the setup for the time-resolved measurement. In the first section of the layout, the XUV supercontinum and IR beams are produced; in the second, these beams are focused into an atomic gas jet; and finally, in the third the overlap of the focal spots of XUV and IR mirrors was imaged, to study their overlap. The detail of each section will follow.

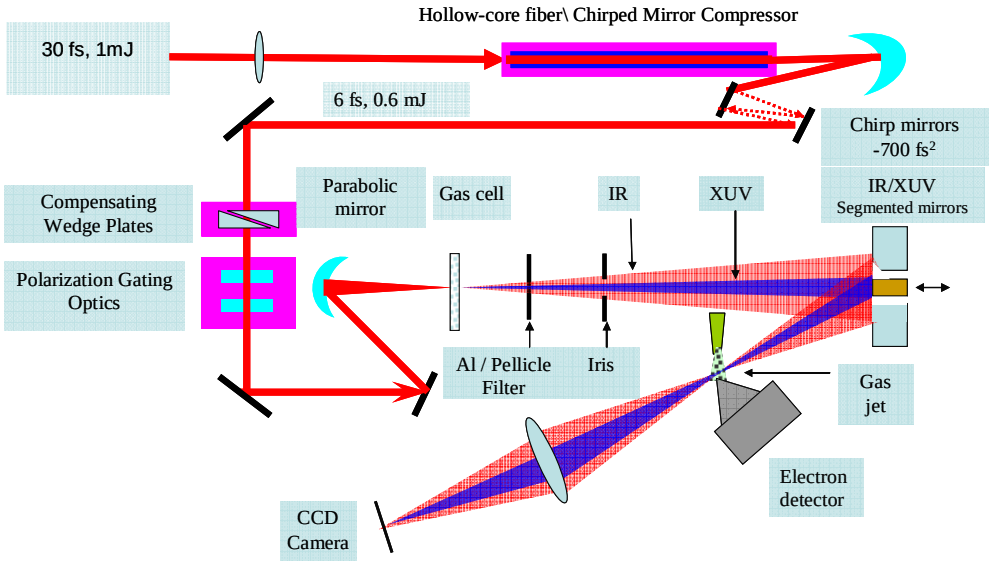

Figure 4.8 Complete layout of setup for time-resolved measurement. Most of the optics are labeled on the diagram. The beam in red color is the IR beam and that in blue is the XUV beam.

A cadkey drawing proposed for the design of the main chamber of the experiment is shown in Figure 4.9 with some dimensions. This setup was supported by a non-magnetic optical table of size 12" x 40". The section of the chamber containing the gas jet and time of flight spectrometer was enclosed in a pair of magnetic coils, each with copper wire of length 7548' and 81 turns. A measured uniform magnetic field of 10 gauss (+ 10% inside the two coils) was obtained when 0.91A of current was flowing through the coils. Most of the parts of the chamber enclosed in the coils were demagnetized by a heat treating process. Extensive care was taken on choosing bolts, nuts, and gas jet for removing residual magnetic properties.

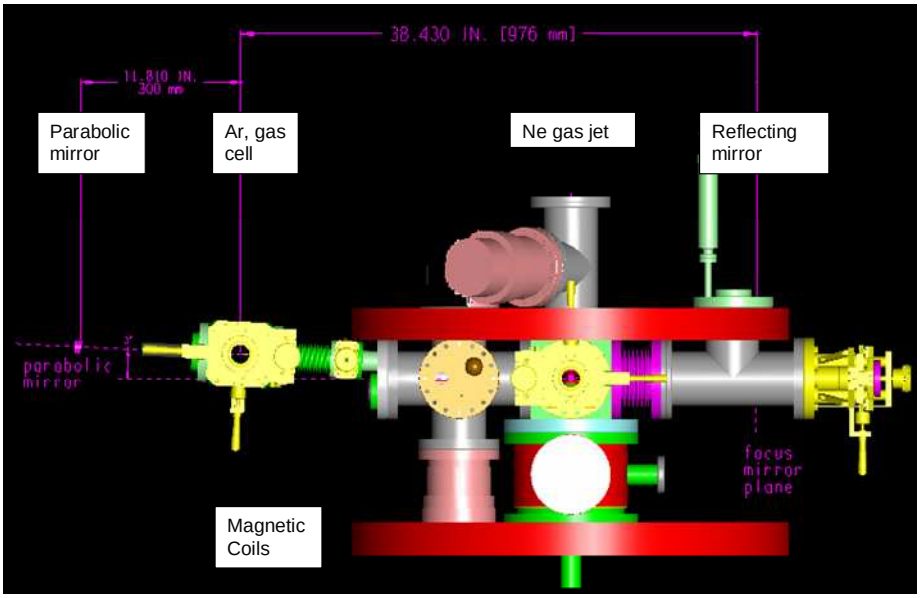

Figure 4.9 Cadkey drawing of the main chamber for time-resolved measurement.

4.3.2 Generating Harmonics

Beam 2 from KLS with pulse energy more than 1 mJ was coupled by a 1 m focal length lens onto the hollow core fiber [Part Number W38535, Glass Ware House] of inner diameter 400 micrometer enclosed in a vacuum chamber filled with Ar or Ne gas for spectral broadening. The optimized gas pressures in the chamber for a broad spectrum before the mode started to break up were 0.5 bars for Ar and 2.4 bars for Ne for corresponding input laser power of 1.2 and 2 mJ respectively. The spectrally broadened pulses were then compressed using chirped mirrors of total GDD of -700 fs^2 [paired mirrors part numbers : 251-300:2 bounces on each,300-251:1 bounce each, 261-299:1 bounce each and one single mirror part number 275, Femtolasers Produktions.]. Two fused silica wedge plates, mounted facing each other's wedge surface, was

moved counter linear in the beam line perpendicular to the beam for proper dispersion compensation without changing the direction and power of the laser beam. The beam then passed through the polarization gating optics, consisting of a quartz plate and an achromatic quarter wave plate. A glass tube of inner diameter 1.4 mm was put at the focus of the parabolic mirror of focal length 30 cm. The laser beam was used for drilling on the entrance and exit walls of the glass tube. The focal spot of the laser was measured by reflecting a few percentage of the beam to a CCD camera using an uncoated BK7 mirror substrate. The measured profile is shown in Figure 4.10 (a) and its lineout along with Gaussian fit in Figure 4.10 (b). The diameter of the profile was ~51 μm measured at $1/e^2$ of the peak intensity.

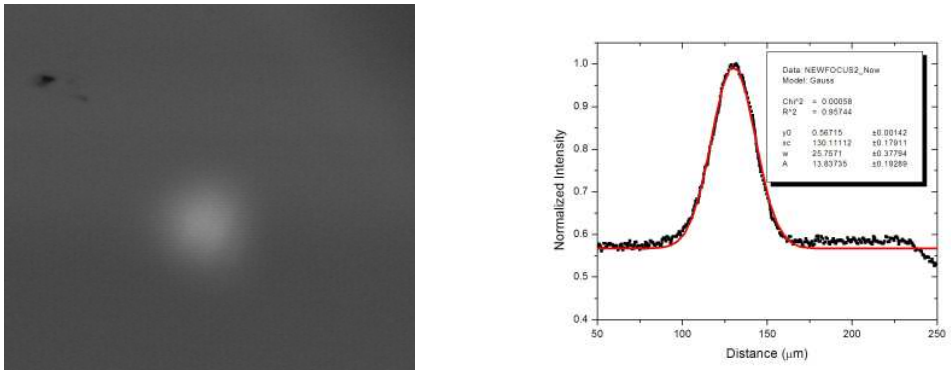

(a) (b)

Figure 4.10 Measured focal spot on the harmonic generation target. (a) Measured image of the focal spot. (b) Its lineout in black dots and corresponding Gaussian fit in red curve.

The backing pressure and the position of the gas cell with respect to the laser focus were optimized for maximum radial intensity of the harmonic beam profile. The XUV beam profile was measured with a detector consisting of an MCP (Part number 1391-0020, Galileo Co.)/Phosphor and a CCD camera in the beam line after the Al filter (Part number 0.1-Al-M-L1.0, Lebow Company) which blocked the residual IR. The measured profile of the harmonics is shown in Figure 4.11 (a) and its lineout in (b). The Gaussian fit of the line out provided the half angle divergence equal to 13.5-mrad. This divergence of the harmonics was one of the keys for determining the size of filter and focusing mirrors afterwards in the beam line.

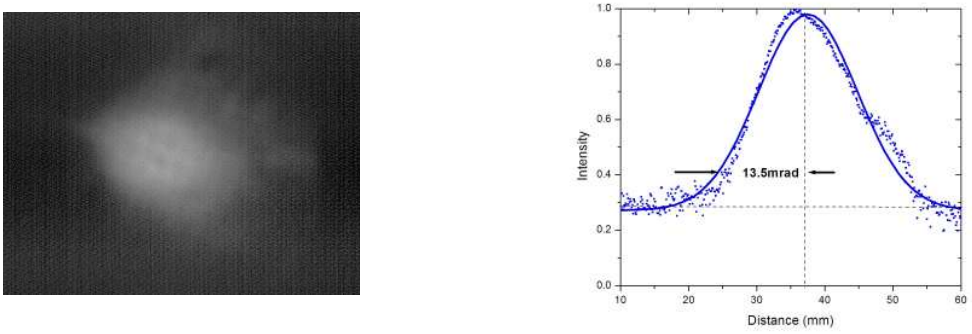

(a) (b)

Figure 4.11 Measured profile and divergence of XUV beam. (a) Beam profile without any aperture on the beam. Positive voltages of 2kV and 5kV were applied on the MCP and Phosphor screen respectively for this measurement. (b) The lineout and a Gaussian fit for the image.

4.3.3 Generating Twin (IR/XUV) Beams

Following harmonic generation, the XUV and the residual IR co-propagate in the vacuum chamber. In order to spatially separate them for the pump/probe application, we designed a

spatial filter consisting of aluminum and pellicle as shown in Figure 4.12 (a). The design progressed in the following way. First, a 2 μm thick pellicle was glued on an optically flat frame of thickness 1.5 mm, ID = 21 mm and OD = 24 mm. Then, a hole of diameter 2.5 mm was drilled at the center of the pellicle. Finally, a 0.2 μm thick, 3.5 mm diameter aluminum supported on a 70 lpi Ni mesh was epoxy mounted on the pellicle surface so that the hole was completely covered with aluminum. After installing this filter in the beam line at 20 cm from the first laser focus, the apertured XUV beam was measured at a position very close to the focusing XUV mirror, and the diameter of the beam was verified to be equal to the mirror (1.3 cm) as shown in Figure 4.12 (b) and (c). It was estimated that more than 50% of the total XUV beam was passed through the filter after considering the area of the filter and its transmission at ~40eV. The pellicle portion of the filter transmitted the IR beam only. Its beam size was controlled with an iris mounted after the filter.

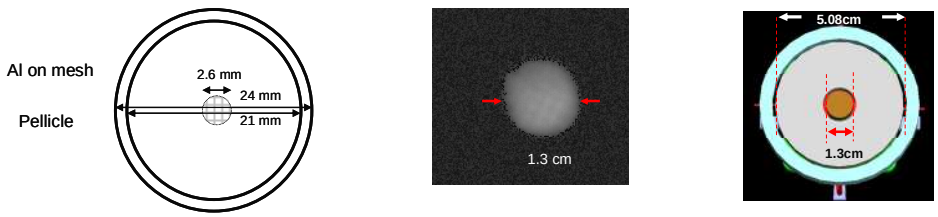

(a) (b) (c)

Figure 4.12 Generating twin (XUV/IR) beams.(a) Design of Al / Pellicle filter (b) Measured XUV beam through the filter and (c) Schematics of XUV(center) / IR(annular) mirrors for matching projection of filter and beam sizes.

4.3.4 Focusing IR and XUV beams

Both the IR and the XUV beams were incident on the respective focusing mirrors after propagation of 98 cm from the first focus. There was an off-axis angle of 2.5 degree (measured in full) introduced on the incoming beam with respect to the plane of the mirrors. This off-axis angle was big enough to keep the incoming XUV beam 1 cm away from the Ne gas target, and small enough to preserve the symmetry of the focal spot due to off-axis aberrations. This configuration was required to ensure that the plane of the detector was parallel to the propagation direction of the reflected beam. The IR beam was focused using an Ag coated *annular* mirror of focal length 25 cm. The mirror was 5.08 cm in diameter and had a hole of diameter 1.9 cm at its center. This hole was enough to secure the 1.3 cm diameter XUV mirror at its center with some free space between two mirrors in order to avoid possible collision during alignment. The focal spot of the annular mirror was measured using an imaging system which will be discussed later in this chapter. The measured focal spot of IR with full beam and its lineout are shown in Figure 4.13 (a) and (b) respectively. The black dots represent the original lineout, and every peak is fitted for Gaussian profile in green lines. The side peaks on the beam profiles were result of diffraction caused by the aperture on the beam created by the inner diameter of the annular mirror. The peak intensity of the highest side peaks were ~40% of that of the main peak. The main peak had diameter of 18 μm measured at $1/e^2$ of the peak intensity.

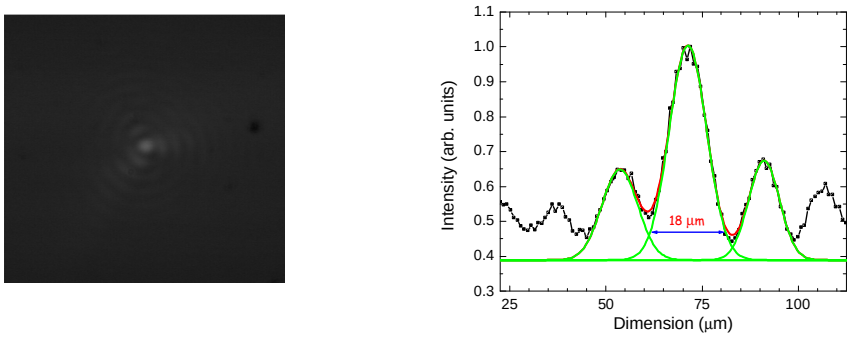

(a) (b)

Figure 4.13 Measured focal spot of IR beam on second target (a) The imaged focal spot with the imaging system (b) its lineout in black dots and Gaussian fits for main and side peaks.

The XUV beam was focused using a bare gold-coated mirror for the preliminary measurements, and afterwards using a Mo-Si multilayer mirror (Part Number BBM-19-35-MS1, NTT, and Japan) of the same focal length of 25cm.The calculated average reflectivity of the mirror in our energy is shown in Figure 4.14. The amplitude of the average reflectivity was ~ 8% from 35 to 65 eV. The phase of the reflection was close to linear. This bandwidth can support a pulse as short as ~15as in the time domain. The estimated focal spot for the XUV was ~1 μm in diameter ($2\omega = \frac{f.\lambda}{D} = \frac{25cm \times 0.025\mu m}{1.3cm} \approx 1\mu m$) which is much smaller than the focal spot of the IR. It ensured that the intensity of the IR was uniform over the XUV focus.

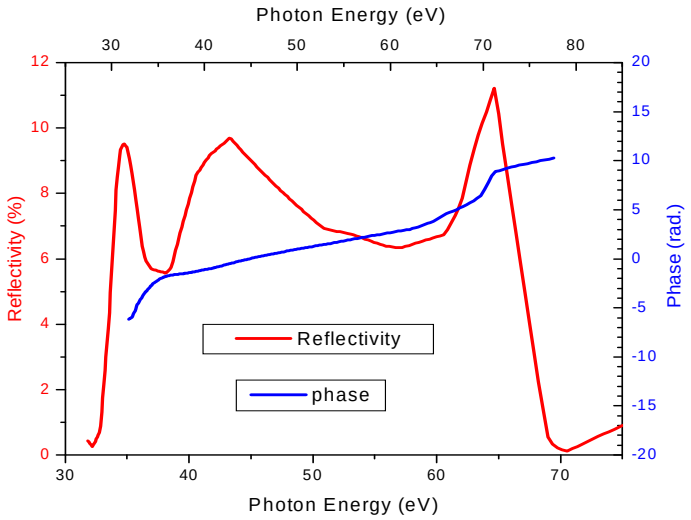

Figure 4.14 Reflectivity of XUV mirror. Red and blue curves represent amplitude and phase respectively.

The mounting of the XUV and IR mirrors is shown in Figure 4.15. First, the XUV mirror was glued on the end of the PZT rod with high vacuum compatible Torr-Seal so that it could be translated back and forth along the direction of the incident beam in fine steps of 40-as in time. The total voltage range of PZT (from 0 to 150 V) produced a maximum delay of 60-fs between the two beams. Second, the PZT rod on a support of 1” in diameter was secured on the custom-designed picomotor driving mirror mount (Part Number 8817-6-V, New Focus) which had three knobs for controlling mirror position. Finally, the IR mirror was mounted on a rigid mount coaxial to the XUV mirror.

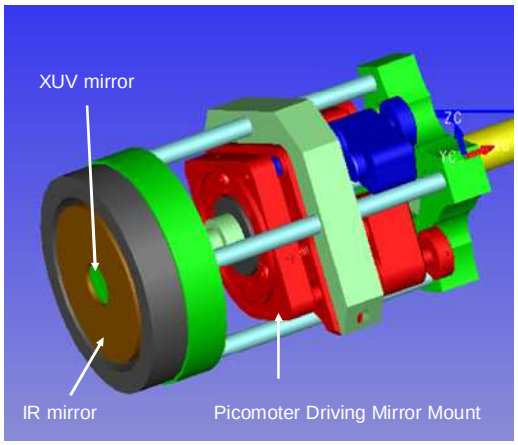

Figure 4.15 XUV and IR mirror mounts.The IR mirror was fixed. The XUV mirror was mounted on a mirror mount shown in red color which could be driven with a picomoter for coarse adjustments, and with PZT for fine translation relative to the IR mirror.

4.3.5 Overlap Monitoring

The temporal and spatial overlap of the focal spots of two mirrors was monitored by an imaging system. For simplicity, the IR beam was shined on the both mirrors, without filter in the beam line. A 2" mirror was installed at 45 degrees to the reflected beams at a distance of 18 cm from the focus of the parabolic mirror so that the beam was reflected out of the vacuum chamber through the window. A 2" biconvex lens of focal length 20.1 cm, installed after the window, imaged the focal spots onto the microscope objective in front of the CCD camera. The magnification of this system was measured by imaging the gas jet of known size and found to be equal to 1.48. After the alignment, several circular, bright and dark interference fringes were observed with transverse motion of the PZT as shown in Figure 4.16 (a) and (b).

(a) (b)

Figure 4.16 Overlap of focus spots of XUV and IR mirrors by shining IR on both. The measured (a) bright and (b) dark fringe obtained by translating XUV mirror with a PZT.

4.3.6 Vacuum and Differential Pressures

Significant absorption of XUV photons by a gas medium when they propagate called for high vacuum in the chamber. The maximum pressure limit of 1.5×10^{-6}Torr for safe operation of the MCP and delay line detector [36] had set a similar limitation for the background gas pressure. The number density of the gas at the target however had to be increased to several Torrs for a sufficient number of atoms at the interaction regions. Several differential pumping schemes had been implemented to achieve these conditions. First, the laser-drilled holes on the gas cell served for pressure differentiators at the harmonic generation section of the chamber. As in the experiment, the glass tube was put 2.5 mm after the focus as shown in Figure 4.17 (a) and performed drilling. Since the measured diameter of the laser spot at the focus was ~50 μm, the size of the spots and thus the size of the corresponding holes at the tube were of diameter ~60 and ~80 μm at its entrance and exit respectively. Second, the spatial filter discussed above for generating the XUV/IR beam was sealed with an o-ring on a VAT valve shown in Figure 4.17 (b)) and inserted in (/out) to the beam line. It served another other pressure differentiator by isolating the harmonic generation section of the chamber from the rest, and thus allowed a

pressure increase at the rate of (~1mTorr/s) up to ~200 Torrs in the former. When the VAT valve was closed, the background pressure on the harmonic generation section of the chamber increased up to ~50mTorr for the backing pressure of ~50 Torr measured near the gas cell. Hence, roughly up to 3 orders of magnitude of difference of pressure was created at the interaction region of the harmonic generation. The third and final pressure differentiation was introduced between the photoionization section and the detector section of the chamber by a cone as shown in Figure 4.17 (c). The cone was machined with a hole of 3-mm in diameter at its tip. It was measured that this hole was small enough to provide a pressure difference of 2 orders of magnitude between the two sections of the chamber when the gas jet was put at ~1mm far from the hole. The detector section of the chamber was evacuated with a turbo of speed 210 lit/s. The photoionization section of the chamber had two turbos of speed 230 lit/s. The harmonic generation section was evacuated with a roughing pump during the experiment.

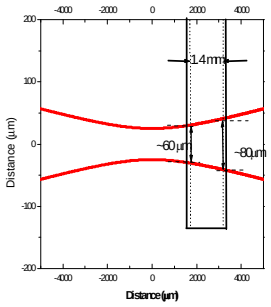

(a)

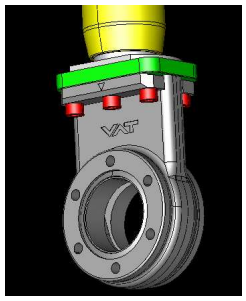

(b)

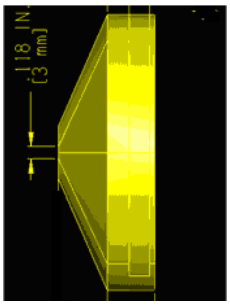

(c)

Figure 4.17 Three schemes for creating differential pressures (a) Using laser drilled glass tube having holes of diameters 60 μ m and 80 μ m at the entrance and exit walls respectively. (b) Vat valve for supporting Al/Pellicle filter which separated the harmonic generation chamber from the rest. (c) A small hole of 3 mm on the tip of the cone which separated the pressure of interaction chamber from that of the detector chamber.

4.4 Electron Detection and Measurement

4.4.1 Electron Time of Flight Spectrometer

A time of flight spectrometer was designed, installed, and operated for detecting the electrons emitted from the interaction region. The following was the geometry of the spectrometer in reference to the direction of the beam. The laser propagation direction was along the y-axis (perpendicular to the paper) and the detector was perpendicular to the z-axis as shown in Figure 4.18.

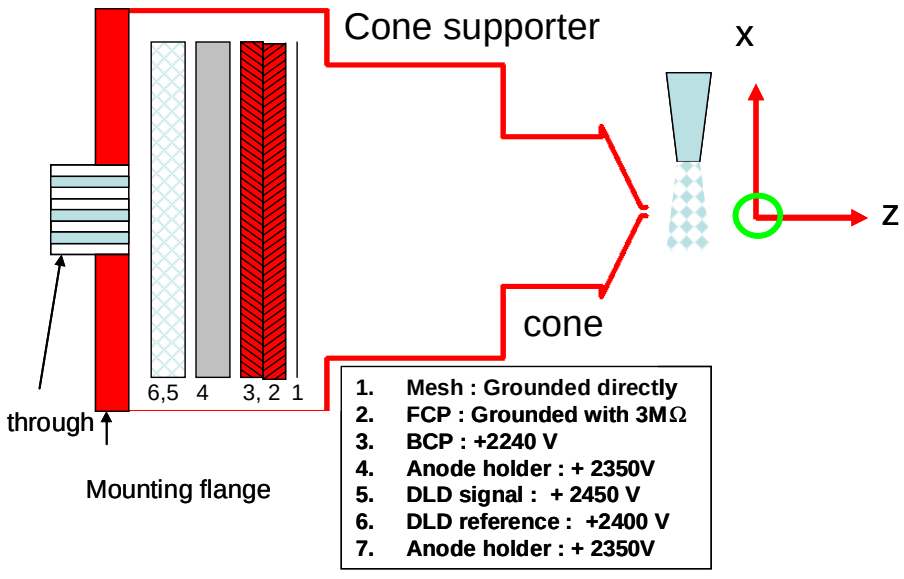

Figure 4.18 Schematic representation of electron time of flight spectrometer. It consisted of a stack of MCP and Delay line anode, DLD 120. Each part of the detector was applied with ascending positive potentials away from the interaction region.

The electrons from the interaction were guided by an external magnetic field applied along the z-axis. The electrons had to travel a minimum distance of 15.3 cm in order to hit the front micro channel plate which was applied with a small positive voltage (~300 V). Once the electrons impact the channel plate surface, secondary electrons were created and multiplied in the micro- channels. The back channel plate was biased with +2240 V which provided ~ +2040 V of difference potential across two channel plates. The electron shower then accelerated towards the delay-line anode which was at higher positive potential with respect to the back channel plate. A voltage of 2350 V was applied to the anode holder and ensured an optimized spatial spreading of the electron shower until the shower propagates to the delay-line anode. The delay-line anode consisted of the reference and signal wires which were biased with 2400V and 2450 V respectively. There were 8 cables from the delay line anode, 1 cable from the anode holder, 1 cable from each channel plate and 1 cable from the mesh, so a total of 12 cables were wired to the feed through cable and accessed to the outside of the vacuum chamber.

4.4.2 Reconstruction of Position

The position of the detected electron was encoded in two dimensions by two sets of orthogonal signal and reference wires in the delay-line detector as shown in Figure 4.19 (a). The electron shower, created by the electron impact on the MCP, induced an electric pulse in the delay line at time $t = t_o$. This pulse was propagated toward the end of the wires in both directions

as shown in Figure 4.19 (b) and arrived at the two ends at times $t = t_1$ and $t = t_2$ respectively. If l_1 and l_2 are the distances to the ends of the wires from the position of the hit, t_1 and t_2 for the x and y directions are written as:

$$t_{x1} = \frac{l_{x1}}{v}, t_{x2} = \frac{l_{x2}}{v} \tag{4.6}$$

$$t_{y1} = \frac{l_{y1}}{v}, t_{y2} = \frac{l_{y2}}{v} \tag{4.7}$$

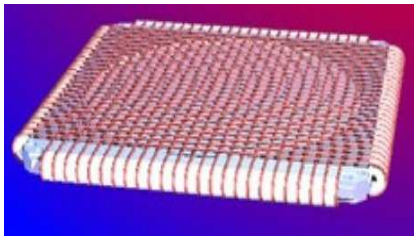

(a)

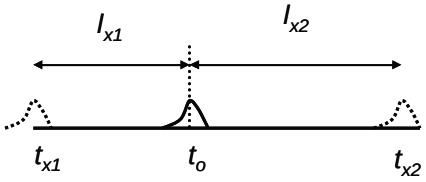

(b)

Figure 4.19 Position encoding with Delay Line Anode. (a) Orientation of two dimensional wires in Delay Line Anode. (b) Recording an event on one of the wires.

Adding t_1 and t_2, and subtracting the time taken by electron to reach to the channel plate (t_{mcp}) and time taken by the electron shower from channel plate to the delay line anode (t_d), gives the net time that was taken by the electric pulse to travel from one to the other end of the wire in the delay line. This time is a constant for a set of detector due to the fixed length of the wires (l_x and l_y) and termed as the time sums:

$$t_{sumx} = (t_{x1} + t_{x2}) - 2t_{mcp} - 2t_d \tag{4.8}$$

$$t_{sumy} = \left(t_{y1} + t_{y2}\right) - 2t_{mcp} - 2t_d \tag{4.9}$$

The measured values were t_{sumx} = 141.1 ns and t_{sumy} = 136.6 ns respectively. In and ideal case, the plot of the time sum with time has to be a delta function; however in practice it does have a finite width which was roughly the resolution of our measurement. The profile of measured time sums plotted in Figure 4.16 (a) and (b) had width at FWHM of 3 ns for both the x and the y positions. It corresponded to the energy resolution of 1.3 eV for measuring photoelectrons produced by the 23rd harmonics on Ne gas (I_p = 21.6 eV) for the flight distance of 0.152 meter.

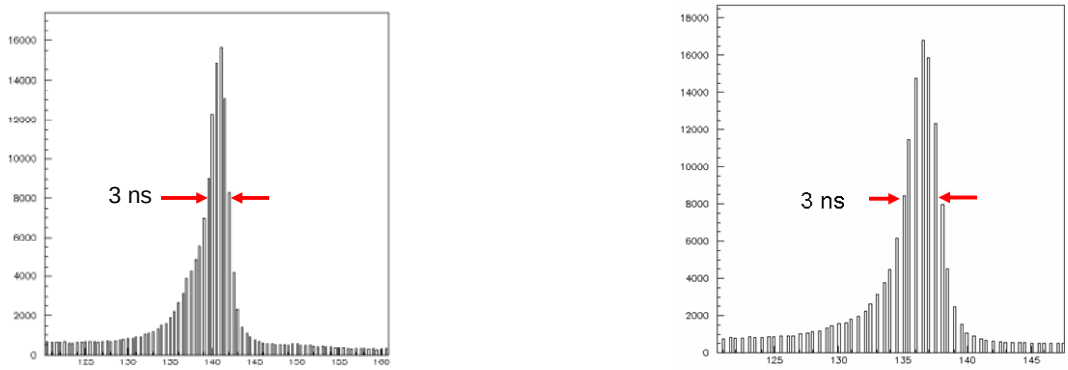

(a) (b)

Figure 4.20 Time sums for x and y signals. (a) x and (b) y

Similarly, subtracting t_2 from t_1 provides the x and y position information of the hit as follows:

$$x = g_x(t_{x1} - t_{x2}) = g_x\left(\frac{l_{x1} - l_{x2}}{v}\right) \tag{4.10}$$

$$y = g_y(t_{y1} - t_{y2}) = g_y\left(\frac{l_{y1} - l_{y2}}{v}\right) \tag{4.11}$$

where g_x and g_y are calibration factors to be determined by proper calibration procedures (e.g. a mask for position calibration). We obtained these numbers from the manufacturer which were; g_x = 0.79365 mm/ns and g_y =0.83333 mm/ns. If $t_{x1} = t_{x2}$, which means the signals take equal amount of time to reach the end of the wires, then position (x, y) = (0, 0), or in other words the hit was at the center of the detector.

4.4.3 Electronics and Signals

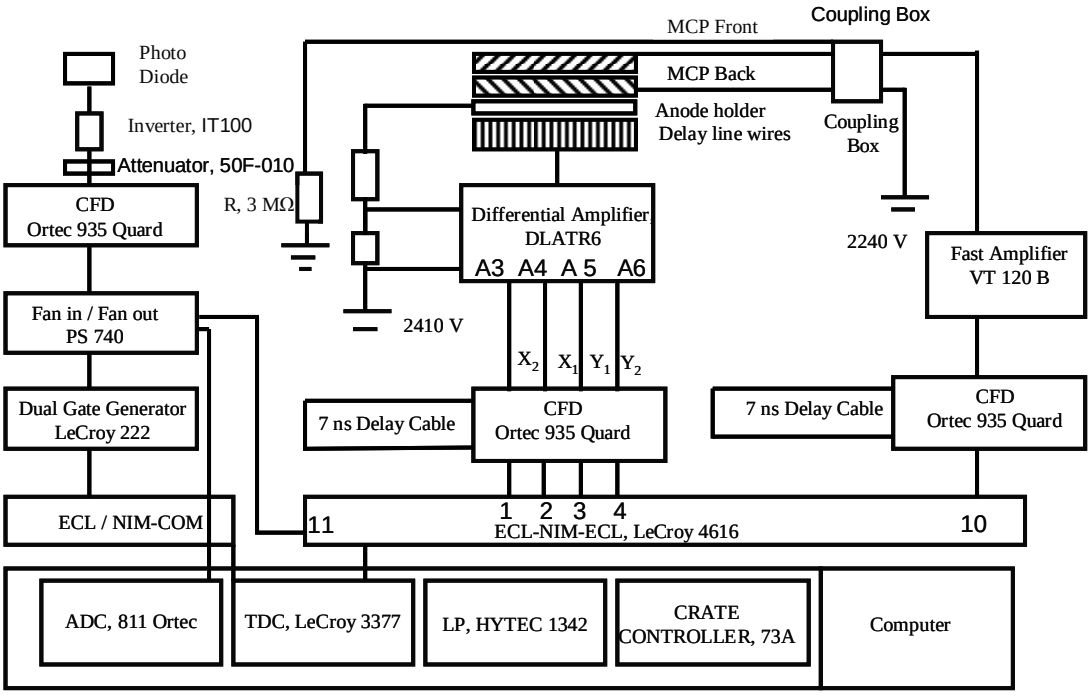

Figure 4.21 Block Diagram of the electronics in the data acquisition system. The system was initiated with a laser signal from the photo diode. The time as well as position of the hit of the electron on the detector was evaluated by extracting and digitalizing the signals from the MCP and the delay line anode.

The time of flight and the position of the hit of the electrons were obtained using the signals from the channel plate and delay-line anode respectively. The schematic in Figure 4.21 depicts the electronics used to successfully digitize these raw signals. In order to obtain the time of flight of the particles, in general, one needs a start signal which initiates the measurement, and waits until the particle to be measured hits the detector, and the hit itself acts as a stop signal and provides the time of flight after subtracting time zero. The procedure for measuring time zero and its origin in the measurement will be discussed later.

In the experiment, the laser signal taken from a photo diode, after being inverted by an Ortec inverting transformer IT100 and attenuated by 50F-010, was used as a start signal to initiate the system. It was first sent to a constant fraction discriminator, Ortec CFD 935, for accurate timing (discussion on use and operation of CFD is presented in Appendix B) and then split into three parts with a divider, logic Fan in / Fan out LeCroy Model 429A . The first part was led to an ECL-NIM-ECL converter and then to the TDC, LeCroy 3377 (discussion and its use and operation are presented in Appendix C) to serve as the start signal. The second signal directly strobed the ADC, Ortec ADC, model AD811 for possible future use. The third signal was led to a dual gate generator, LeCroy 222, and created a time window. This NIM signal after being converted to ECL by an ECL/NIM converter triggered the TDC .This window of time was set to 1 μs meaning that after starting the clock with the start signal the system would wait until then for registering the stop. If for instance a stop signal did not appear at all for a corresponding start signal within this window, the measurement is reset for another start signal.

The signals from the MCP and delay line anode stopped the clock and provided the time and position information. The MCP was biased using a dc-coupling box (shown in Figure 4.23 (a) where the back channel plate was supplied with +2240 V using power supply PS350 Stanford

Research System, and the front channel plate was grounded with a 3 MΩ resistor. This was to ensure a potential difference of slightly more than 2000V across the channel plates and ~ +300V on the front channel plate since the MCP stacks had resistance of ~40 MΩ measured in high vacuum at this voltage. The signals measured directly from the MCP are typically weak, in our case they were of amplitude 5 to 10 mV, and thus were subject to amplification. We used a fast amplifier, Ortec VT120 B, which has an inverting gain of 200 for this purpose. The measured signal from the front channel plate after amplification was as shown in Figure 4.22 (a). This signal was led to one of the channels of the constant-fraction timing circuit (CFD), Quard 935 which incorporates four separate and independently adjustable timing discriminators. The purpose of using this module again was to select timing instant on each input pulse independent of its mostly fluctuating amplitude. When properly adjusted, the generation of the output pulse corresponds to the point on the leading edge of the input pulse where the input pulse has risen to 20% of its maximum amplitude. The details on the CFD and its uses in the measurement of fast timing signals are presented in Appendix B. The amplified signal of the channel plate had a small after-pulse with amplitude ~10% of the main signal, which was eliminated by the CFD as in Figure 4.22 (c). These NIM signals were converted to ECL signals afterwards by the ECL-NIM-ECL converter, LeCroy 4616, and finally led to the TDC. The TDC digitizes these stop signals from the channel plate as well as the start signal from the photodiode, and provides the time difference as the time of flight.

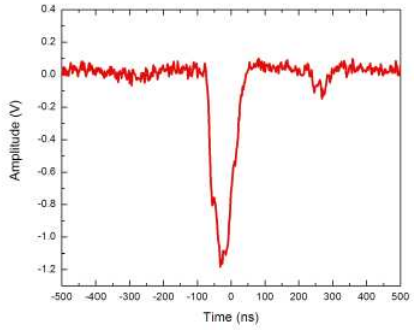

(a)

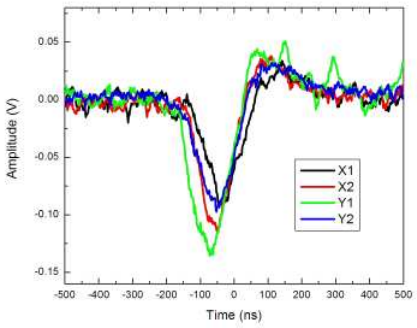

(b)

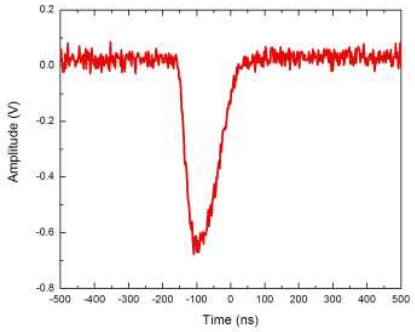

(c)

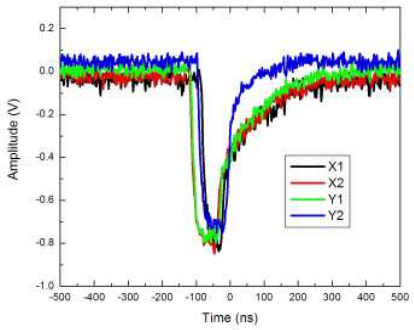

(d)

Figure 4.22 The fast timing signals from MCP and DLD. (a) Time signal from front channel plate (b) Position signals from Delay Line Detector (c) Signal from front channel plate after CFD and (d) Signals from Delay Line Detector after CFD

Signals from the delay line anode were used for measurement of the position of the electron hit. The bias voltage to the signal, reference, and anode holder was applied from a single

power supply using a voltage divider circuit as shown in Figure 4.23 (b). The 4 pairs of signals from the signal and reference were differentially amplified using DLATR6. This unit hosts 6 channels and provides DC-signal de-coupling on its own. We used channels A3-A6 for applying voltage to and obtaining and amplifying signals from the delay-line anode. The measured 4 position signals after amplification were as shown earlier in Figure 4.22 (b). These signals were also fed into the CFD, Ortec 935. The measured delay line signals after the CFD are plotted in Figure 4.22 (d). The properly timed NIM signals were then converted to an ECL signal using the NIM-ECL-NIM converter, LeCroy 4616, and fed to the TDC.

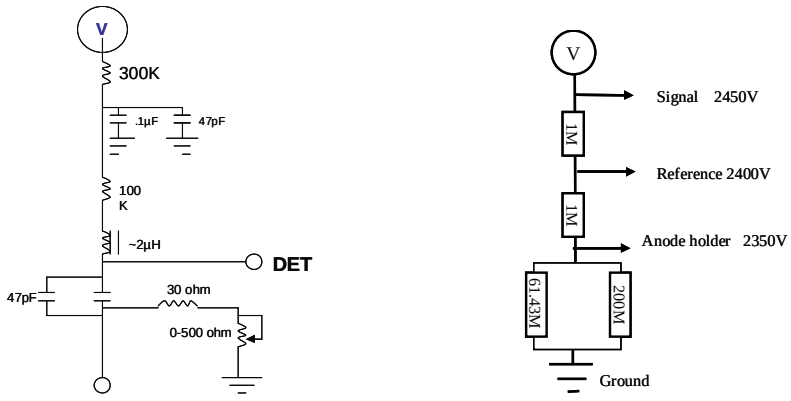

(a) (b)

Figure 4.23 DC coupling circuit for MCP and voltage divider circuit for DLD

A list processor, HYTEC LP 1341, was used to buffer all the digitalized time signals from the TDC and sending them finally to the computer. A LabVIEW routine was used for online monitoring of the detector image, time of flight spectrum and wiggle spectra etc. The offline data analysis was performed in the Physics Analysis Workshop (PAW) software.

4.4.4 Data Analysis with PAW

The analysis began with the collected raw signals and led towards plotting the final 2d momentum spectrum and total energy spectra. Six timing signals were fed to 6 out of 32 channels of the TDC. Out of six, four were from the delay line anode for position information and one was from the channel plate for time of flight information, and the last one was the master clock signal called the "bunch marker" obtained from the photo diode. We will see later in this section that the essential parameters for the momentum/energy calculation include the distance of flight (t_{mcp}), absolute time zero (t_o), cyclotron frequency (ω) of an electron in the magnetic field, and time-to-position conversion factors (g_x and g_y) for each dimension of the position sensitive detector. The flight distance was measured during the assembly of the spectrometer. The magnetic field strength was also measured using a Gauss meter. For more precise calculations, however, most of the parameters were deduced from the measured data by using unique characteristics of the motion of discrete energy photoelectrons in the uniform magnetic field.

a) How to deduce the time zero (t_o) and cyclotron frequency (ω) from the measured data:

Prior to discussing a procedure to calculate (t_o), it is worth mentioning how it is introduced in the time of flight measurement. In an ideal case, as in the upper half of Figure 4.24, the time of flight would be simply the difference of the time when electron hits the detector (t_{stop}) with the time when it was born (t_{born}) at the interaction region. In a real measurement however, the born time (t_{born}) cannot be read directly. Instead, a reference signal was created by splitting the laser beam which served as a master clock and thus allowed us to replace (t_{born}) with (t_{start} -

t_o) as displayed in the lower half of Figure 4.24. The value of (t_o) depends upon the time taken by the start signal to reach the detector with respect to (t_{born}) .

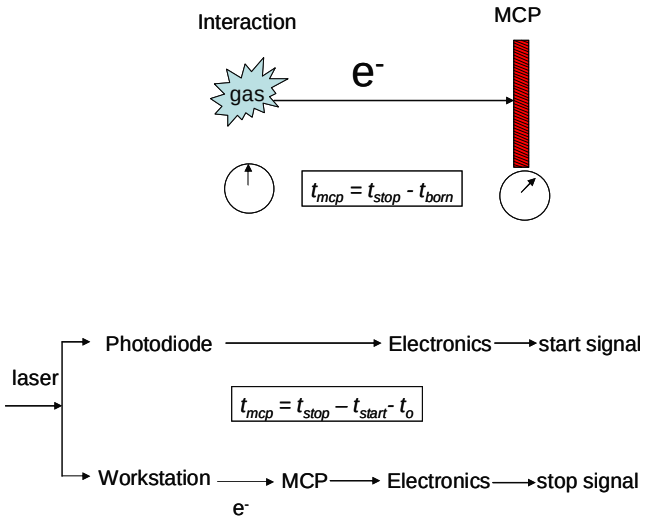

Figure 4.24 Introduction of time zero in the time of flight measurement. The upper picture shows the ideal case of time of flight measurement, and the lower part is its realization in practice which introduces time zero.

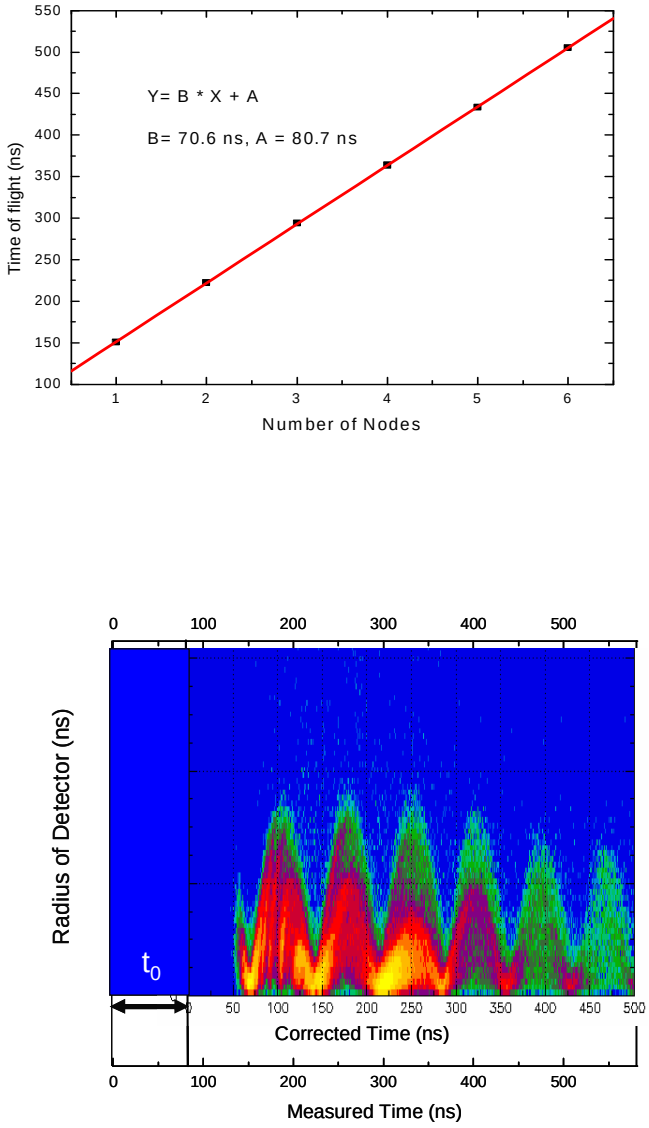

Figure 4.25 Evaluating time zero and cyclotron frequency. The upper graph shows the plot of time of flight with respect to the nodes of the wiggles spectrum. The slope of the linear fit provided the cyclotron period (T), and the intercept on time of flight axis gives t_o. The lower graph shows the spectrum before and after subtracting t_o.

The measured wiggles spectrum is shown in the lower graph of Figure 4.25. The lower horizontal axis in this graph is the time of flight before subtracting t_o. There are 7 nodes in the time range shown. The time of flight at the nodes was plotted with the number of nodes as shown in the upper half of this figure, and a linear fit was performed. The slope of the line measured the cyclotron period (T) of 70.6 ns in this particular case. It corresponds to the angular frequency ($\omega = 2\pi/T$) of 0.0889 GHz. The intercept made by this linear fit corresponded to the measured value of t_o, which was equal to 80.7 ns in this case. The time scale was corrected by subtracting this value for further analysis. The value of time zero and angular frequency were subject to change, the former with possible change in cable length, electronics modules, laser focus position and gas jet position, and the latter when a different strength of magnetic field was applied.

b) How to reconstruct each component of momentum and total energy of the electrons:

The following exercise is to obtain the expression of each component of momentum and finally the total energy as a function of the position of the hit on the detector and the time of flight. Let us first consider a standard case in which the initial momentum of the electron is along the positive X-direction. The electron, under the action of a magnetic field pointing orthogonally into XY plane, follows a counterclockwise circular path in the XY plane as shown in Figure 4.26.

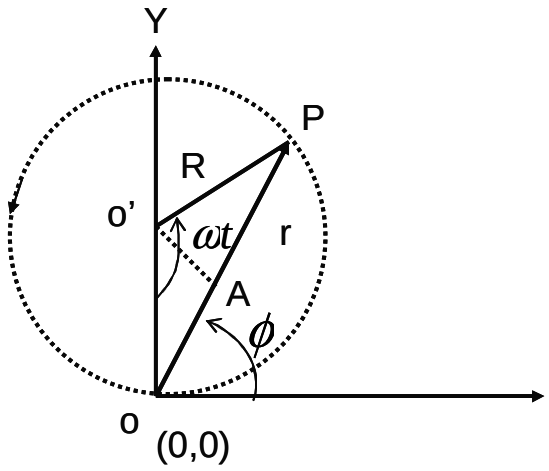

Figure 4.26 Cyclotron motion of electron in magnetic field, standard case

In ΔO'AP, $\sin\left(\frac{\omega t}{2}\right) = \frac{AP}{O'P} = \frac{r/2}{R}$, where R is the radius and ω is the angular frequency of the cyclotron motion, and r and ϕ are polar coordinates for describing the position of the electron. This implies:

$$R = \frac{r}{2\sin\left(\frac{\omega t}{2}\right)} \tag{4.12}$$

From Newton's equation of motion, the motion of an electron in a uniform magnetic field of strength (B) is described as:

$$BeV = ma = m\frac{V^2}{R} = mV\frac{V}{R} = mV\omega \tag{4.13}$$

$\Rightarrow \qquad \omega = \frac{eB}{m}$ and $p_\perp = mV = BeR$ where, $p_\perp$ is the momentum in the XY plane

which is perpendicular to the direction of the initial laser polarization. It can be written in terms of r, ω and t (= t_{mcp}) which are all measured parameters.

$$p_\perp = \frac{m\omega r}{\left|2\sin\left(\frac{\omega t_{mcp}}{2}\right)\right|} \tag{4.14}$$

The other component of momentum, $p_\parallel$ which is parallel to the initial laser polarization (perpendicular to XY plane) is not affected by the magnetic field. So, it can be directly given by the time *(t_{mcp})* and distance of flight (s).

$$p_\parallel = p_z = \frac{ms}{t_{mcp}} \tag{4.15}$$

Let us now consider a more general case when the initial velocity of the electron is making an arbitrary angle α with the X axis as shown in Figure 4.27.

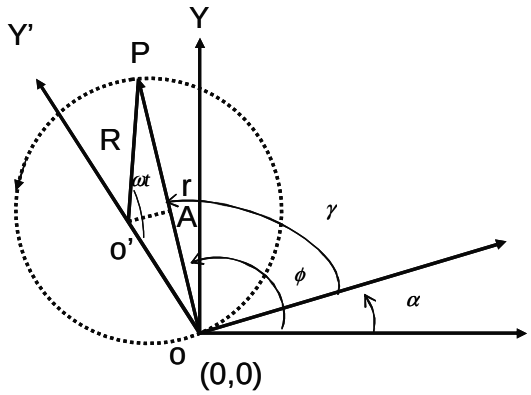

Figure 4.27 Cyclotron motion of electron in magnetic field, general case.

The angles are defined in such a way that $\alpha = \phi - \gamma$. From the geometry, $\angle$ *O'OX'* = $\angle$*O'O*P $+\angle\ \gamma = \left(\frac{\omega t}{2}\right) + \angle O'OP$ which implies that $\gamma = \frac{\omega t}{2}$. Thus:

$$\alpha = \phi - \frac{\omega t}{2} \tag{4.16}$$

Now, the X and Y components of momentum p_x and p_y can be expressed as follows:

$$p_x = p_\perp \cos\alpha = p_\perp \cos(\phi - \gamma) = p_\perp (\cos\phi\cos\gamma + \sin\phi\sin\gamma)$$

$$p_x = \frac{m\omega}{\left|2\sin\left(\frac{\omega t_{mcp}}{2}\right)\right|}\left(X\cos\left(\frac{\omega t_{mcp}}{2}\right) + Y\sin\left(\frac{\omega t_{mcp}}{2}\right)\right)$$

$$p_y = p_\perp \sin\alpha = p_\perp \sin(\phi - \gamma) = p_\perp (\sin\phi\cos\gamma - \cos\phi\sin\gamma)$$

$$p_y = \frac{m\omega}{\left|2\sin\left(\frac{\omega t_{mcp}}{2}\right)\right|}\left(Y\cos\left(\frac{\omega t_{mcp}}{2}\right) - X\sin\left(\frac{\omega t_{mcp}}{2}\right)\right)$$

OR,

$$p_x = \frac{m\omega}{2}\left(X\ \cot\left(\frac{\omega t_{mcp}}{2}\right) + Y\right) \tag{4.17}$$

$$p_y = \frac{m\omega}{2}\left(Y\cot\left(\frac{\omega t_{mcp}}{2}\right) - X\right) \tag{4.18}$$

$$\Rightarrow \qquad p_\perp = \sqrt{{p_x}^2 + {p_y}^2} \tag{4.19}$$

The expressions in 4.15 and 4.19 were used for obtaining parallel ($p_\parallel$) and perpendicular ($p_\perp$ or p_z) components of momentum respectively. The components of momentum p_x and the p_y were obtained using expressions 4.17 and 4.18. The total energy of the electron was calculated using the following expression.

$$E = \frac{1}{2m}\left(p_{\parallel}{}^{2} + p_z^2\right) \tag{4.20}$$

4.4.5 Acceptance Angle

The ionization of a Ne atom by linearly polarized XUV photons results in emission of the electrons in almost all directions with some angular distribution discussed below. The angular distribution depends upon the differential cross-section as follows:

$$\frac{d\sigma}{d\Omega}(\theta) = \frac{\sigma}{4\pi}\left[1 + \beta\left(\frac{3}{2}\cos^2\theta\right) - \frac{1}{2}\right] \tag{4.21}$$

Where σ is the total cross-section, Ω is the solid angle, and β is the angular distribution parameter. For 2p sub shell ionization of Ne atoms with ~40 eV of photon energy, where σ = 8 Mb (1 Mb = 10^{-18} cm^{-2}), and β = 0.9, the differential cross-section is calculated and displayed in the red curve in Figure 4.28. Here, θ = 0 represents the direction of polarization of the XUV beam.

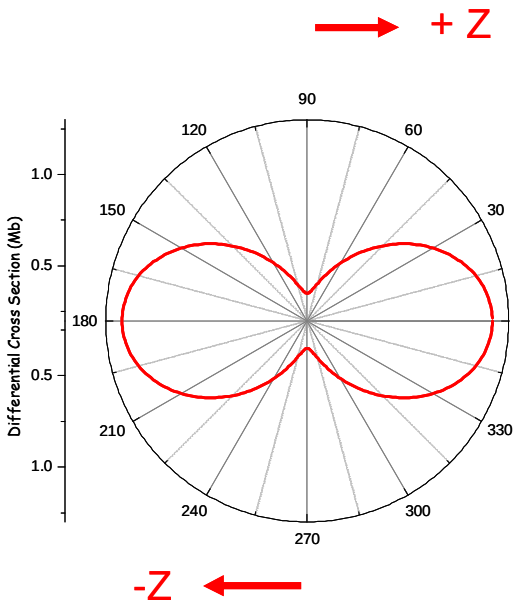

Figure 4.28 Differential scattering cross-sections for Ne gas at 40eV.

In our measurement the electrons initially flying away from the detector (towards + z) do not retain any probability to be accepted at the detector. But those initially flying towards the detector (-z), after being guided by the external magnetic field may hit the detector. The amplitude of the magnetic field and the geometrical acceptance angle of the time of flight spectrometer determined the actual acceptance for the electrons of certain energy. Increasing the magnetic field increases the acceptance angle but it cannot be increased above a certain value, otherwise the resolution of the measurement worsens as most of the electrons hit the small area of the detector. The following calculation was done in addition to the measurement which allowed us to see the trajectories of the electrons in the spectrometer. It provided us information about whether the electrons were blocked on their way to the detector and helped in improving the setup in order to accept maximum possible angular distribution of the electrons and find the appropriate magnetic field.

Equation 4.15 can be re-written as:

$$r = \frac{2 p_{\perp} \sin\left(\frac{\omega t_{mcp}}{2}\right)}{m\omega} \tag{4.22}$$

The schematic of the chamber enclosing the spectrometer is shown in Figure 4.29 in order to see which part of it may block the electrons. The angle θ for this purpose is defined as the half acceptance angle. With this angle, the perpendicular component of momentum ($p_{\perp}$) can be written in term of the total momentum (p) as:

$$p_{\perp} = p \sin\theta \tag{4.23}$$

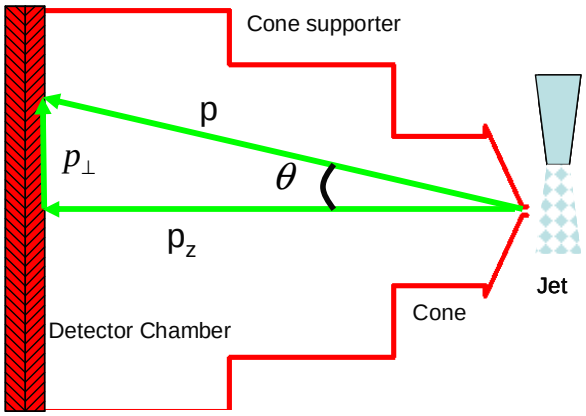

Figure 4.29 Defining an acceptance angle in the time of flight spectrometer.

Similarly,

$$p_z = p\cos\theta \tag{4.24}$$

From the basic principle of the photoelectric effect, the total energy of an incident photon is equal to the sum of the ionization potential of the atom and the energy of the photoelectron after the photo-ionization. In our case, by considering the ionization 2p sub shell of a Ne atom, the total momentum in can be written in terms of the harmonic order (N) as follows:

$$p = \sqrt{2m[N\times 1.55 - 21.6]/27.2}\times 1.99\times 10^{-24} \tag{4.25}$$

Using equations 4.16, 4.22, 4.23 and 4.24 in equation 4.21, and replacing ω with $\frac{2\pi}{T}$, we can re-write the trajectories of the electrons as follows:

$$r = \frac{Tp\sin\theta}{m\pi}\sin\left(\frac{\pi s}{Tp\cos\theta}\right) \tag{4.26}$$

Using equations 4.25 and 4.26, the trajectories of electrons corresponding to different order of harmonics are calculated for different value of θ.

After initial installment of the spectrometer, the acceptance angle was measured as shown in Figure 4.30 (a) and found to be ~30^{o} in full angle for the photoelectrons from the 23^{rd} harmonics. In order to study the possibility of further increasing the acceptance angle some calculations were made using equations 4.25 and 4.26, and the results were as shown in Figure 4.30 (b). This figure shows trajectories of the discrete energy electrons in the spectrometer for ~ 3.7 gauss of magnetic field. It can easily be seen from this calculation that the angle was specially limited by two places in the spectrometer which are indicated by two red circles in the diagram; the first was the entrance angle at the cone and the second was the limitation introduced by the cone supporter. Then, the setup was modified in order to make it able to accept a larger angle. The most recent version is as shown in Figure 4.30 (c) where those two limitations were avoided. The calculation showed a maximum of ~80 degrees of acceptance angle in full for the photoelectrons produced by the 23^{rd} harmonics. In the real measurement we found that the angle was ~65 degrees as shown in figure 4.30 (d). During the measurement, it was also realized that the position of laser focus relative to the cone, which is not very easy to measure precisely, also changes the measured acceptance. From the calculation it was found that the new limitation on the acceptance angle is now set at the end of the cone supporter, indicated by the red circle in Figure 4.30 (c). So far, this was the maximum possible acceptance angle without a dramatic change in the setup, and is already a wide one of this kind in the literature.

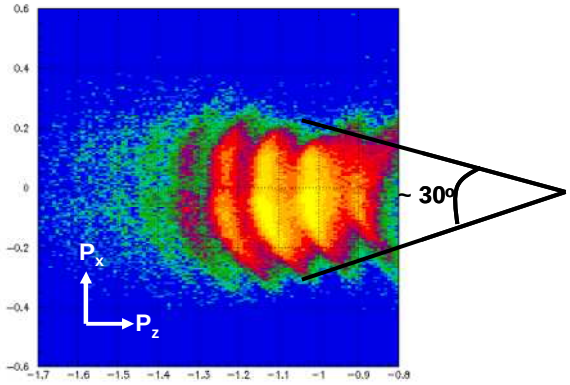
~ 30°
P_x
P_z

(a)

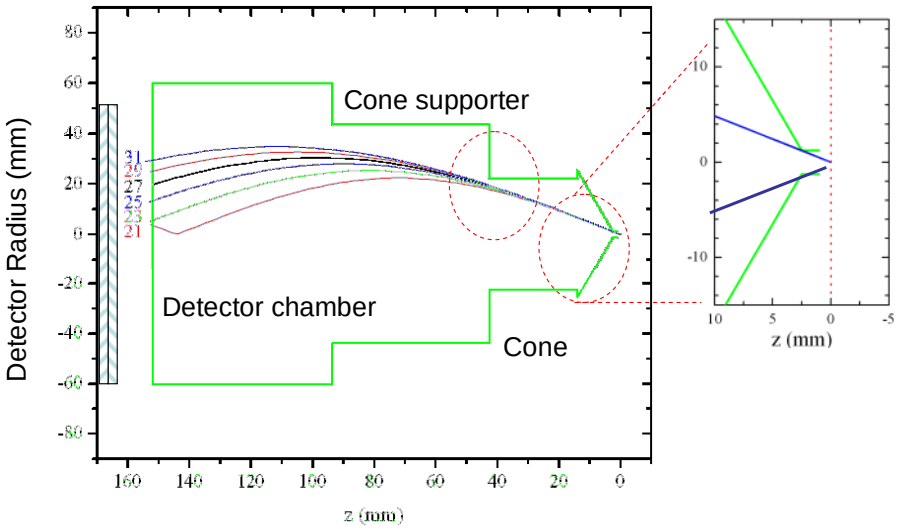
Cone supporter
Detector chamber
Cone
Detector Radius (mm)
z (mm)

(b)

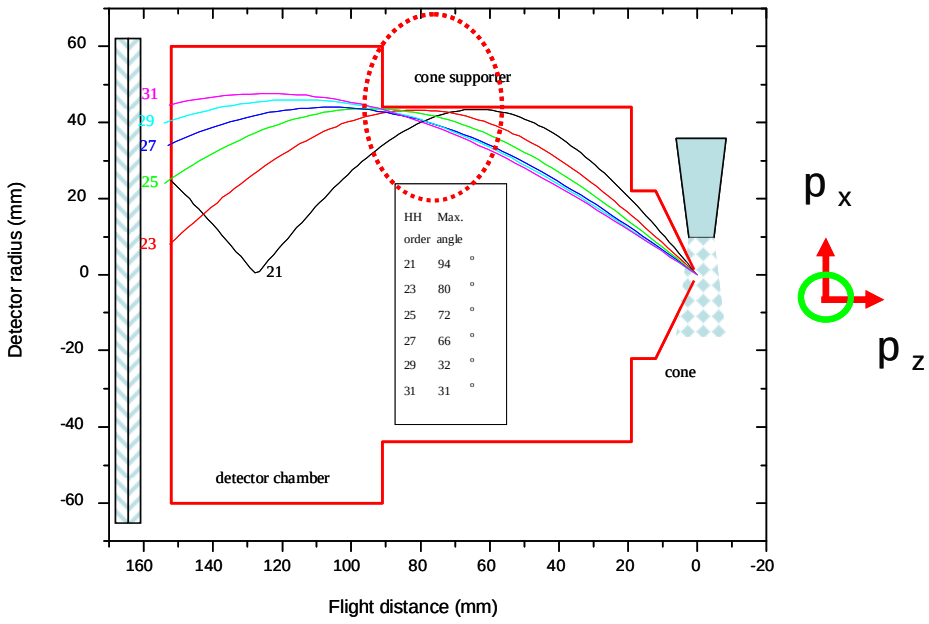

(c)

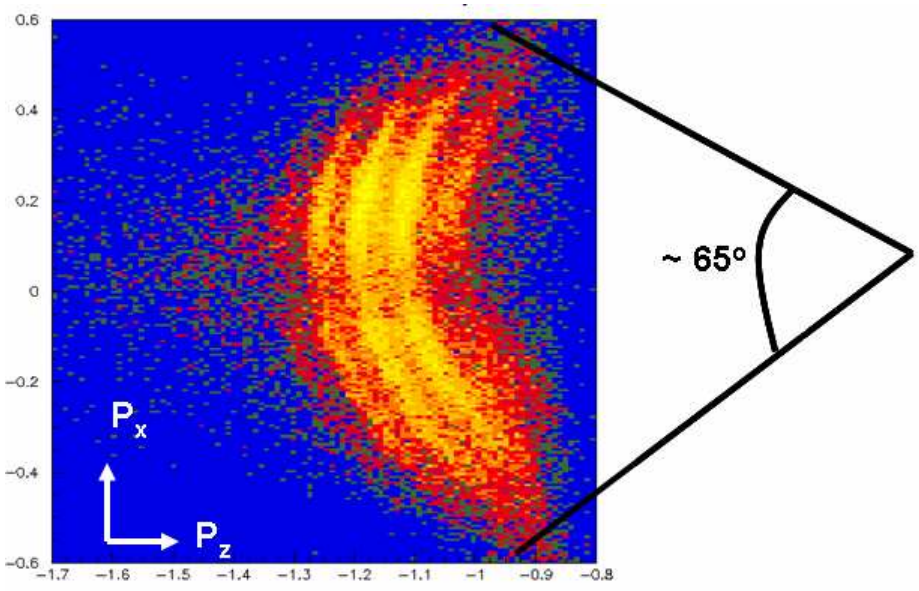

(d)

Figure 4.30 Calculated and measured acceptance angles. (a) Measured momentum spectrum showing the acceptance angle for previous version of the setup. (b) The corresponding calculated

electron trajectories. (c) The calculated electron trajectories for new version of the setup. (d) The corresponding measured momentum spectrum showing the acceptance angle.

4.5 Measured ATI spectrum

When the laser intensity is high enough, the atoms or molecule may absorb more photons than they require during ionization. This process has been known as above threshold ionization (ATI) and the energy of an electron produced during the process is given by the following equation:

$$E(ev) = nh\upsilon - (I_p + U_p) \tag{4.27}$$

where n is the total number of photons absorbed, I_p is the ionization potential of the gas (13.5 eV for Kr in the following measurement), and U_p is the pondermotive potential which can be calculated as:

$$U_p = 9.33\times10^{-14} I(W/cm^2)\ \lambda(\mu m)^2 \quad \text{eV} \tag{4.28}$$

In our experiment, while performing XUV-IR pump-probe measurement, we would like to obtain enough intensity of IR at the target so that the XUV photoionized electrons could be streaked by the strong IR laser field. At the same time if the intensity is too high, direct ionization of atoms may occur and produce excessive ATI electrons. The ATI electrons can easily destroy the resolution in the measurement of XUV photoionized electrons. Therefore, the goal here is to suppress the ATI process but obtain enough intensity for streaking. In order to estimate the lower limit of the laser intensity which can lead to ATI process in our experiment, we performed the measurements of the ATI spectrum for different laser intensities. The following measurement was for the lowest laser intensity for which we performed the measurement.

In this measurement, laser pulses of energy of 33 μJ and duration of 33 fs were focused onto Kr gas using a focusing lens of focal length 25 cm. The measured focal spot was of diameter 50 μm at $1/e^2$ of the peak intensity. It corresponds to the peak laser intensity of 1 x 10^{14} Watt/cm^2 at the interaction region. Here, I = 1 x 10^{14} W/cm^2, λ=0.78 μm give U_p= 5.7 eV and $(I_p + U_p)$ = 19.2 eV $\simeq$ 12 photons of energy 1.55 eV. So, absorption of more than 12 photons by Kr atoms leads to the ATI process.

The measured spectra are shown in Figure 4.31. The first picture (a) is the reconstructed detector image. The measured wiggle spectrum and time of flight spectrum are shown in (b) and (c) respectively. There are nodes formed in the wiggle spectrum due to cyclotron motion of the electrons in the magnetic field at ~70, 142, 214 ns etc. with period of 72 ns. The time of flight spectrum also has peaks at these nodal positions. In our measurement these peaks are not subject to any physical interpretation. However, the peaks between two consecutive nodes, for example between the first and second nodes, correspond to the discrete energy ATI electrons. There are peaks at 76.8, 82.6, 91.3, 103.5 and 122.2 ns observed in the time of flight spectrum. For flight distance of 16 cm for this measurement, 76.8 ns corresponds to 12.4 eV of energy which is equal to the energy of 8 photons (i.e. 1.55 x 8), 82.6 ns corresponds to 10.65 eV which is close to the energy of 7 photons and so on. The 2D momentum images in (d) also show the corresponding discrete structures in momentum. For example, there is a discrete structure at 0.95 au of p_z at $p_{||}$ = 0 which corresponds to the total energy of 12.27 eV. It is equal to the energy of 8 photons. Similarly the other 5 discrete structures between two nodes (at 1 and 0.5 au) also check out the energies of 7, 6, 5 and 4 photons. This way all the observed peaks in the time of flight spectra are understood and interpreted as ATI electrons with energy or momentum separated by one photon.

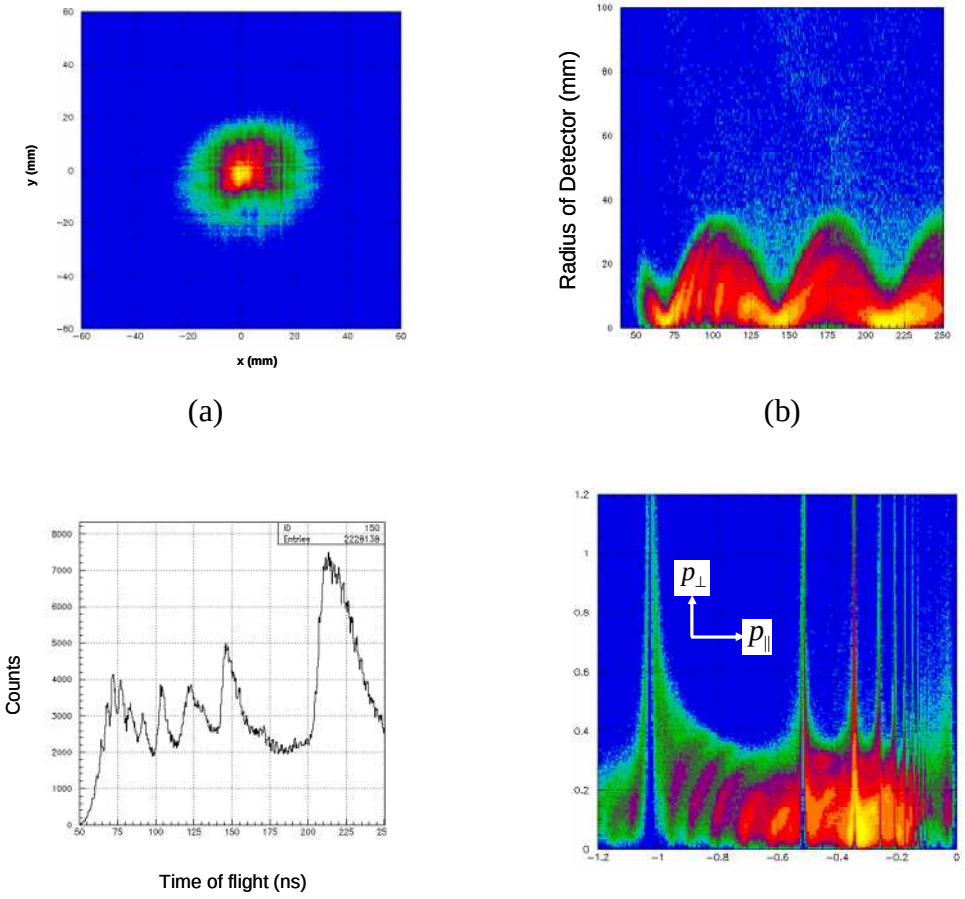

(a) (b)

(c) (d)

Figure 4.31 Measurement of ATI electrons. (a) Detector image (b) Wiggles spectrum (c) Time of flight spectrum and (d) 2d momentum spectrum. A laser of intensity 1 x 10^{14}W/cm^2 was used in this measurement and the laser polarization was along the z direction.

4.6 Laser Assisted Photoelectron Spectrum

The modification in the primary photoelectron spectrum in the presence of a laser field has been studied extensively in the past few years [12, 38, and 39]. It is believed that this modification is due to the momentum transfer between the emitted photoelectrons and the strong laser field. Prior to further describing this process in detail, we categorize it into two parts depending on the duration of photoelectron emission (τ_x) relative to the duration of the laser cycle (T_l). (1) $\tau_x >> T_l$ or long pulse limit and (2) $\tau_x << T_l$ or the short pulse limit. Let us discuss the laser assisted photoelectron spectrum in these two limits.

4.6.1 Long Pulse Limit

It has been well explained in the literature [12, 38, and 39] that in this limit in addition to the main peaks, sidebands are produced on the laser assisted photoelectron spectrum. This effect has been understood as free-free transition: the electron absorbs or emits one photon from or to the IR during the photo ionization process and goes from one free-state to another. In addition, the total spectrum shifts towards lower energy due to an increase in the binding energy of the atoms in the presence of the laser. The energy of a sideband is given by the following:

$$E_s = h\gamma_{xuv} \pm h\gamma_{IR} - I_P - U_p^{IR} \tag{4.29}$$

where $h\gamma_{xuv}$ is the energy of the XUV photons, $h\gamma_{IR}$ is the energy of the IR photons, I_P is the ionization potential of the interacting medium, and U_P^{IR} is the pondermotive energy. The laser assisted photoelectron spectrum has been explained with the *interference picture* [39] which works for wide range of duration of the XUV pulse. In this picture it is considered that the sidebands are due to the interference effect of the photoelectron wave packets that are produced

over the XUV pulse (longer than a laser cycle) and kicked off by different phase of IR. The coherent superposition of all contribution leads to formation of sidebands in long pulse limit.

In our experiment we used the observation of the sidebands as a tool to optimize the temporal and spatial overlap of IR and XUV pulses and finally determine the intensity of IR on the second target by observing the pondermotive shift. In the experiment instead of using long pulses directly from the amplifier, we used the same beam delivery system as described in Figure 4.1 but without any nonlinear medium in the hollow core fiber in order to turn off the self phase modulation. It allowed us to use a better spatial profile of the beam after the hollow core fiber in comparison to that directly from the amplifier. Moreover, it was easy to go into the short pulse configuration when required without changing any significant alignment, i.e. just by introducing the gas into the fiber.

The measured primary photoelectron energy spectrum is shown in the first row of Figure 4.32. Here, in all of these spectra: in Figure 4.32(a) the wiggle spectrum, (b) the total energy spectrum and (c) the 2d momentum picture, the discrete harmonic peaks starting from the 23^{rd} harmonics to the cutoff were observed which were separated by twice the IR photon energy. The solid lines on the wiggle spectrum are the corresponding calculated discrete harmonics. The dashed lines in the total energy spectrum are the locations of calculated discrete harmonic energy peaks. There was good agreement between the calculation and the measurement with the consideration that in the wiggle spectrum the observation of the complete trajectories was limited by the acceptance angle of the system.

In the presence of IR, for a particular delay, the spectrum was modified as shown in the second row of Figure 4.32. First, clear evidence was that the whole spectrum shifted towards lower energy by 0.5 eV. We estimated the laser intensity by using the following relation:

$$U_P^{IR} = 9.33\times10^{-14} I(W/cm^2)\lambda(\mu m)^2 \qquad \text{eV} \qquad (4.30)$$

This relation implied laser intensity equal to 8.2 x 10^{12} W/cm^2. Second, the sidebands were produced on either side of the main peaks. We optimized the temporal and spatial overlap of the XUV and IR foci for obtaining maximum possible intensity of the sidebands relative to the main peaks.

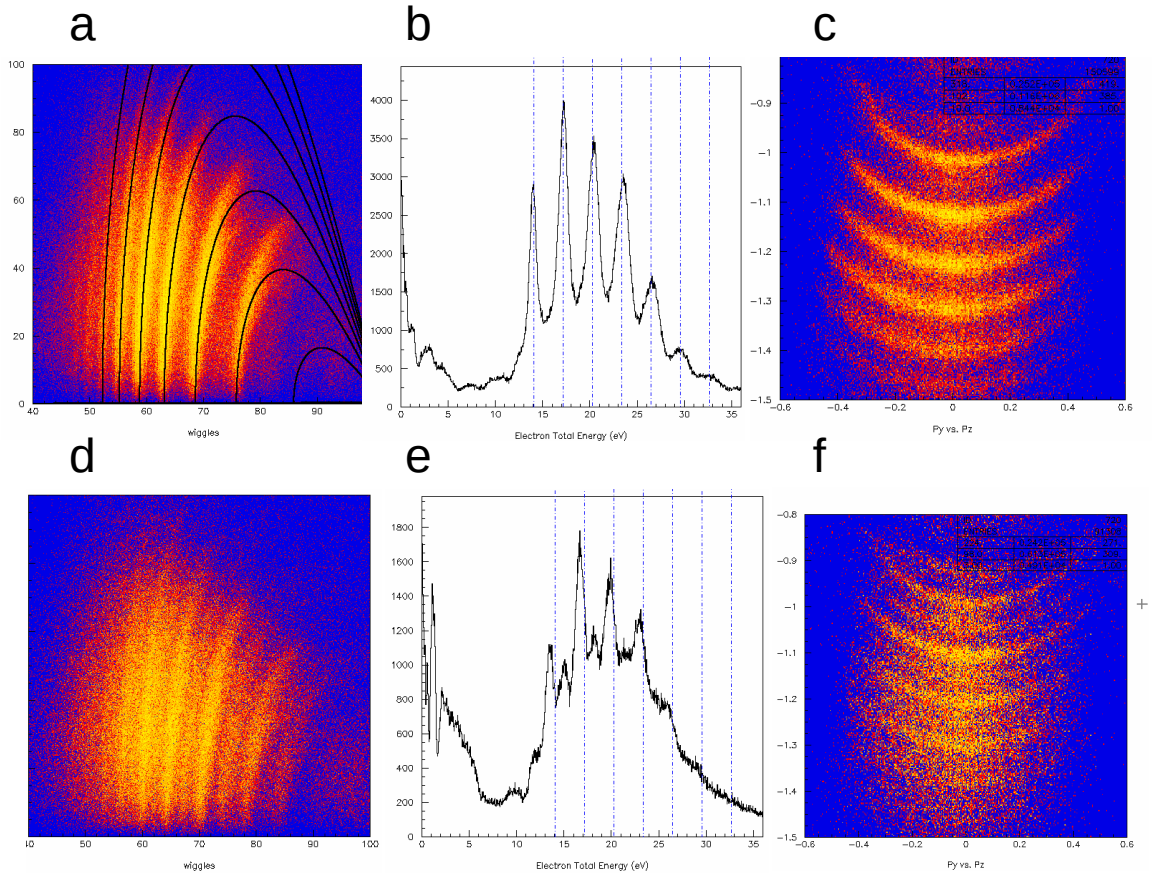

Figure 4.32 Laser assisted photoelectron spectrum in long pulse limit. Primary photoelectrons spectrum is displayed in the first row: (a) the wiggle spectrum (b) the total energy spectrum, (c)

the 2d momentum image. The Second row has laser assisted photoelectron spectrum in long pulse limit: (d) the wiggle spectrum (e) the total energy spectrum (f) the 2d momentum images.

4.6.2 Short Pulse Limit

When the duration of photoelectron emission is shorter than the laser cycle ($\tau_x << T_l$), the final energy or momentum of the electron depends more sensitively upon the delay between the electron emission and the laser field's oscillations. This effect can be utilized for attosecond resolution in the measurement. For example, Drescher *et al.* [39] showed in calculation for the auger decay that if $\tau_x \leq T_l/5$, no sidebands but the oscillations (up and down momentum shifts) are produced in the spectrum depending upon the delay between the XUV and IR pulses.

The first row of Figure 4.33 has the measured primary photoelectron spectra in the case of short pulses of duration ~ 8 fs. (a), (b) and (c) are the measured wiggle spectrum, total energy spectrum and 2d momentum representations respectively. The corresponding laser assisted spectra are on the second row of the same figure. In this short pulse limit, every harmonic peak in the primary spectrum was broader than the IR photon energy of 1.5 eV, and thus it was difficult to distinguish between the possible structures of sidebands or oscillations (up and down shift) in the laser assisted spectra. Some oscillation or sidebands like structures were observed on the laser assisted 2d momentum picture, and much broader peaks were observed on the energy spectrum.

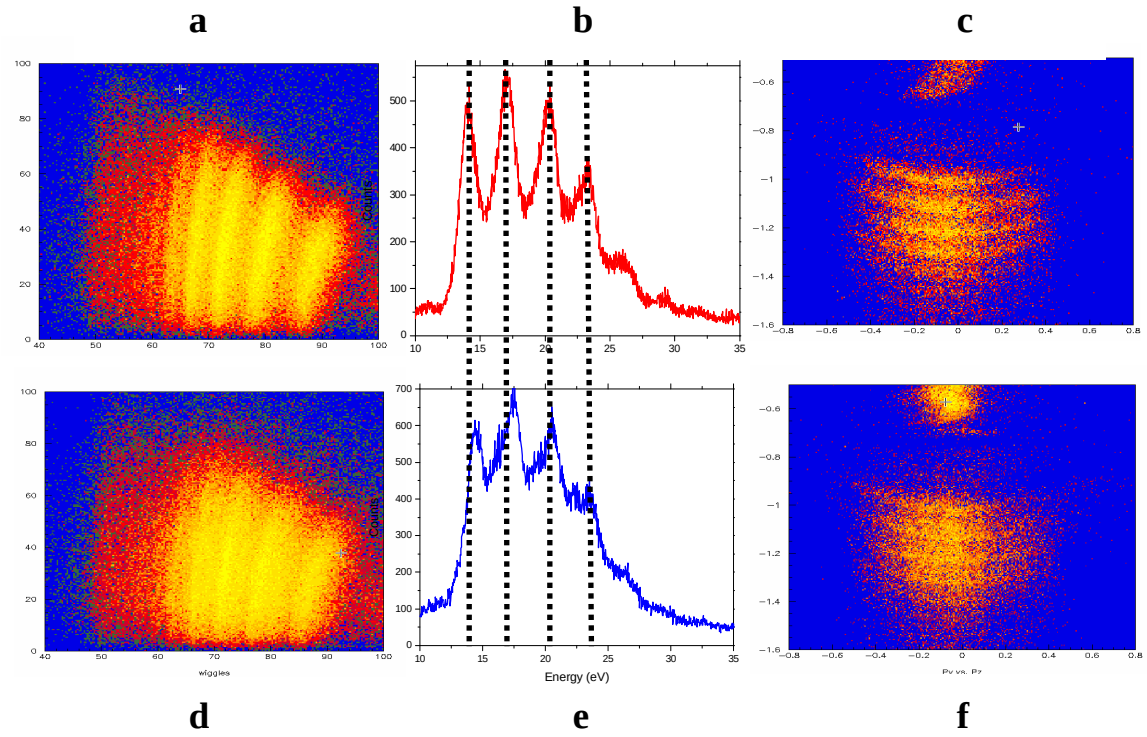

Figure 4.33: Laser assisted photoelectron spectrum in short pulse limit. Primary photoelectrons spectrum is displayed in first row: (a) wiggle spectrum, (b) total energy spectrum, (c) 2d momentum picture. Second row has laser assisted photoelectron spectrum in (d), (e) and (f) respectively.

4.7 Effect of Polarization Gating on Photoelectron Spectrum

We studied the effect of polarization gating on the XUV photoelectrons measurement. In this measurement, a quartz plate of thickness 0.41 mm and a quarter wave plate were used for polarization gating of the higher order harmonic spectrum. Figure 4.34 (a) was the measured total energy spectrum without gating and (b) was that with polarization gating. This comparison showed that a supercontinum was produced in the energy spectrum while using polarization gating.

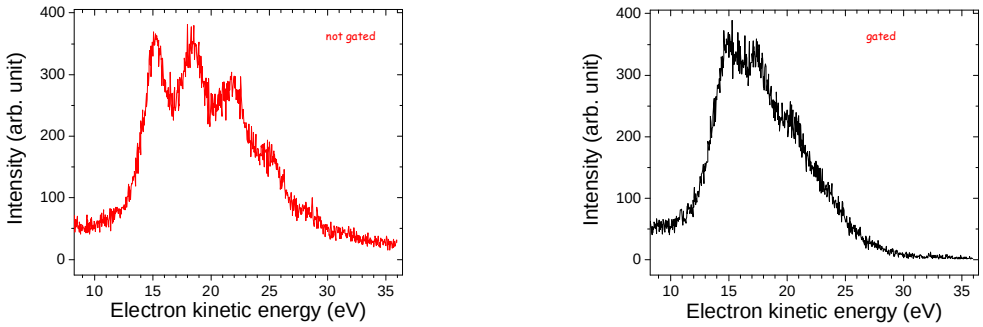

(a) (b)

Figure 4.34 Effect of polarization gating on photoelectron spectrum. Measured total energy spectrum of photoelectron (a) without polarization gating (b) with polarization gating.

After changing from the not gated to the gated condition, the electron count rate decreased by more than factor of 5. The lower count rate requires longer data acquisition time. But, there is always a time limit for stabilizing the CE phase [40] in the real measurement. Thus, in our experiment we put forward all possible efforts to maximize the electron counts. While using ~0.6 mJ of laser energy as a driving pulse, ~50 Torr of backing pressure on the first target, and ~1 x 10^{-4} Torr of background pressure on the second target, we measured a maximum photoelectron count rate of ~150 in the case of polarization gating. The bias voltages applied on the MCP and DLD were 2410 and 2240 V respectively. With that condition, the integration time of 10 to 20 minutes was enough to see the nature of the photoelectron spectrum.

4.8 Attosecond Streaking and Challenges

The magnitude and direction of the streak on the photoelectrons due to the laser depend upon the vector potential of the laser at the time when the photoelectrons are born in the laser

field. The amplitude of maximum streak for several laser intensities is plotted in Figure 4.35. For example, a maximum streak of 10eV along the z direction is estimated for laser intensity of 1.5 x 10^{13} W/cm^2 at 0.667 fs from the zero delay of the pulse.

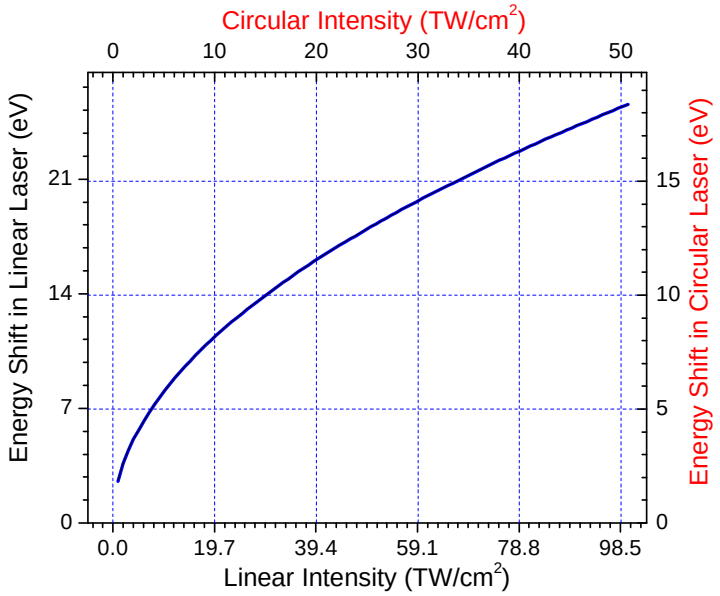

Figure 4.35 Maximum streaks on energy spectrum with ellipticity varying pulse. The pulse was produced by one left and one right circular pulse of duration 8-fs, which were delayed by 8-fs before their recombination. One of the maximum streaks was at 0.667 fs from the zero delay of the pulse.

In the measurement, first the XUV photoelectrons were measured using smaller iris size so that only the XUV, but no laser, was passed through it. Then, the iris was opened wider in order to introduce the IR along with XUV at the interaction region. When the iris was opened fully, the ATI electrons were produced in a much larger number than the XUV photoelectrons at the interaction region. Moreover, the energy of some of the ATI electrons is so high that they even reach the same energy scale as that of the XUV photoelectrons. The counts from lower

energy ATI was beyond the capacity of our measuring system. This introduced a challenge in the measurement. One way to overcome this challenge would be to increase XUV photon flux and another way would be to reduce the ATI electrons. Presently we are working on deflecting the lower energy ATI electrons away from the detector by applying small negative voltage in front of it. In the future we might want to work towards optimizing the gas target, for example using a rectangular gas jet which would allow us to enhance the XUV photoelectron counts and decrease the ATI electron count. Installing such a jet, with its length along the laser propagation direction and width along the z – direction, should in principle sufficiently suppress the ATI counts and even increase the XUV photoelectron count. It is because the focal spot of the XUV beam should be much smaller than that of the IR beam along the transverse direction of propagation. But this idea is yet to be tested and implemented.

4.9 Result and Other Possibilities

A workstation for time-resolved measurement was designed and built which can be used for real time characterization of a single attosecond pulse and then to explore the dynamic behavior of the inner-shell electron in atoms and molecules on the attosecond time scale. Linearly polarized pulses of duration ~30 fs were used for producing a discrete harmonic spectrum from Ar gas. The XUV beam was focused onto the Ne gas jet and 2d momentum spectrum of XUV photoionized electrons was collected at an acceptance angle as large as ~65 degree. By focusing the IR together with the XUV onto the gas target, a laser assisted photoelectron spectrum was measured. The laser assisted spectrum had sidebands on either side of the main peaks. The temporal overlap between XUV and IR pulses was further optimized using short IR pulses of duration ~10 fs. By using the ellipticity varying pulse from polarization

gating as the driving pulse, a supercontinuum was measured in the photoelectron energy spectrum with count rate as high as ~150 counts per second on average. This is the current status of this project. In the future, it is expected to streak the supercontinum with different phase of ellipticity varying laser pulses, and to measure the attosecond pulse in real time.

CHAPTER 5 – Conclusion and Outlook

In this dissertation, we showed an experimental method to compress laser pulses from ~30fs to ~6fs, and mainly focused on how to obtain higher energy pulses with this technique. Recently, some further progress towards increasing the energy of few cycle pulses has been made in our research group. This has been done by using highly laser susceptible Ne gas as the non-linear medium. Similarly, a new pulse compression method, the liquid crystal phase modulator, is under construction and will possibly replace the chirped mirrors in the future. This method, which is based upon a genetic algorithm, will allow more flexibility in the amplitude of the group velocity dispersion and can also compensate the higher order dispersion.

Using these sub-ten-fs pulses, we studied the method of polarization gating for producing an XUV supercontinuum in high-order harmonics. By measuring the spectrum, we showed that this method allows using a relatively longer pulse of ~8fs to produce a single attosecond pulse in the XUV region. This method has been proved as a simple way of producing ellipticity varying pulses in comparison to the conventional way of using the Mach-Zehnder interferometer.

We designed and built an attosecond streak camera with a much larger acceptance angle in comparison to the recently reported ones and capable of measuring the 2d momentum spectrum of laser assisted XUV photoelectrons. This is a beginning towards characterizing and using attosecond pulses. We expect that such a high speed camera will make the dream of experimentally capturing the motion of electrons in atoms and molecules come true in the future.

CHAPTER 6 – References

[1] S. Sartania *et al.* Opt. Lett., 22, 20, 1562, (1997)

[2] B. Shan, S. Ghimire and Z. Chang, Phys. Rev. A, 69, 021404(R)(2004)

[3] S. Sartania *et al*. Opt. Lett. 22, 20, 1562 (1997)

[4] A. Verhoef *et al.* Applied Physics B, 82, 513-517 (2006)

[5] L. Xu *et al*. Opt. Lett. 21(16),1259-1261 (1996)

[6] E. Goulie *et al*., Science, 305, 1267 (2004)

[7] G. Sansone *et al*., Science, 314, 443 (2006)

[8] Z. Chang, Phys. Rev. A, 70, 043803 (2004)

[9] B. Shan, S. Ghimire and Z. Chang, Phys. Rev. A., 69,021404(R)(2004)

[10] E. Constant *et al*., Phys. Rev. A, 56, 3870-3878 (1997)

[11] M. M. Shakya and Z. Chang, SPIE Proceeding, 5534, 125-131 (2004)

[12] P. M. Paul *et al*. Nature, 292, 1683(2001)

[13] W. H. Knox. *et al.* App. Phys. Lett., 46, 12, 1120 (1985)

[14] R. L. Fork *et al.,* Opt. Lett. 12,7, 483 (1987)

[15] M. Nisoli *et al.,* App. Phys. Lett., 68 (20), 2793 (1996)

[16] S. Sartania *et al*. Opt. Lett., 22, 20, 1562 (1997)

[17] M. Nurthuda et al., Riken Rev., 49, 10 (2002)

[18] G. Fibich and A.L. Gaeta, Opt. Lett., 25, 5, (2000)

[19] M. Nurthuda *et al*., Riken Rev., 49, 10 (2002)

[20] Juan L.A. Chilla and Oscar E. Martinez, Opt. Lett, 16, 1, 39 (1991)

[21] Daniel J. Kane and Rick Trebino, Opt. lett., 18, 10, 823 (1993)

[22] A. Baltuska *et al.*, Opt. Lett., 23, 18, 1474 (1998)

[23] R.W. Boyd, Nonlinear Optics, Academic Press (2003)

[24] A. E. Siegman, Lasers, University Science Books (1986)

[25] F. A. Ilkov *et al.*, J. Phys. B, AMO Phys., 25, 4005 (1992)

[26] M. Drescher *et al*., Science, 291, 1923 (2001)

[27] R. Keinberger *et al*., Nature, 427, 817 (2004)

[28] P.B. Corkum, N. H. Burnett and M. Y. Ivanov, Opt. Lett., 19, 1870 (1994)

[29] B. Shan, S. Ghimire and Z. Chang, J. of Mod. Opt., 52, 2-3, 277-283 (2005)

[30] P. Dietrich *et al*. Phys. Rev. A 50, R3585 (1994)

[31] S. Ghimire, M.S. Thesis, Kansas State University (2003)

[32] P. Dietrich *et al.* Phys. Rev. A 50, 3585(R) (1994)

[33] V. T. Platonenko and V. V. Strelkov J. Opt. Soc. Am. B 16, 435 (1999)

[34] B. Shan and Z. Chang, Phys. Rev. A, 65, 011804 (R) (2002)

[35] Z. X. Zhao, Z. chang, X. M. Tong and C. D. Lin, Proc. SPIE Vol. 59207

[36] RoentDek Handels GmbH, Manual of MCP delay line detector Version 6.2.82.7

[37] Bouhal *et al*., Phys. Rev. A, 58, 389 (1998)

[38] T. E. Golver *et al.*, Phys. Rev. Lett. 76, 2468 (1996)

[39] M. Drescher *et al.*, J. Phys. B, 38, S727 (2005)

[40] C. Li *et al*. Optics Express, 14, 23, 11468 (2006)

Appendix A- KLS and Its Beam Line to the Experiment

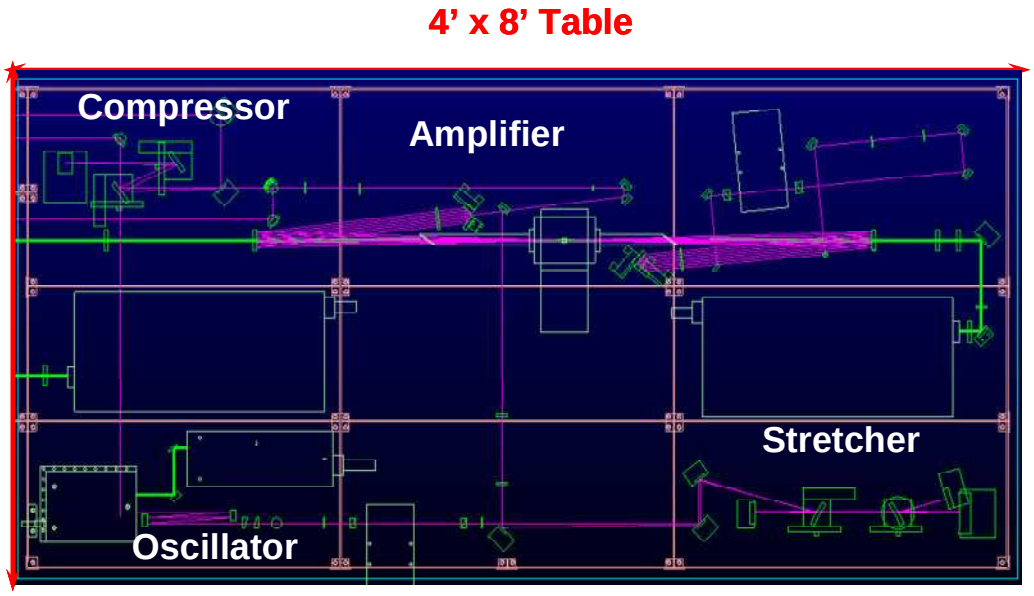

Figure A.1 Schematic representation of Kansas Light Source

The Kansas Light Source is a compact high power system resting on a 4' x 8' optical table as shown in Figure A.1. It began with seed pulses from a commercial oscillator, Femtolasers, which produces 0.5 nJ pulses at 76 MHz repetition rate. One out of every thousand pulses, selected by a pockel's cell, was first spectrally stretched using an all reflective, grating based stretcher, and then sent to the amplifier. The amplification was performed in two stages using a single crystal. First, in the pre-amplification stage, the seed pulses were focused down to the beam diameter of ~0.6 mm on the laser crystal and amplified with a gain of 10^5 to 10^6 in sevenpasses. Second, in power – amplification, the beam was first diverted and made smaller in size using a telescope, and led back to the amplifier. With the same cavity mirrors used in the first stage, the beam was focused down to the diameter of ~1.2 mm on the laser crystal. With another 7 passes, this stage provided a gain of ~100. Finally, the pulses were compressed using a pair of gratings.

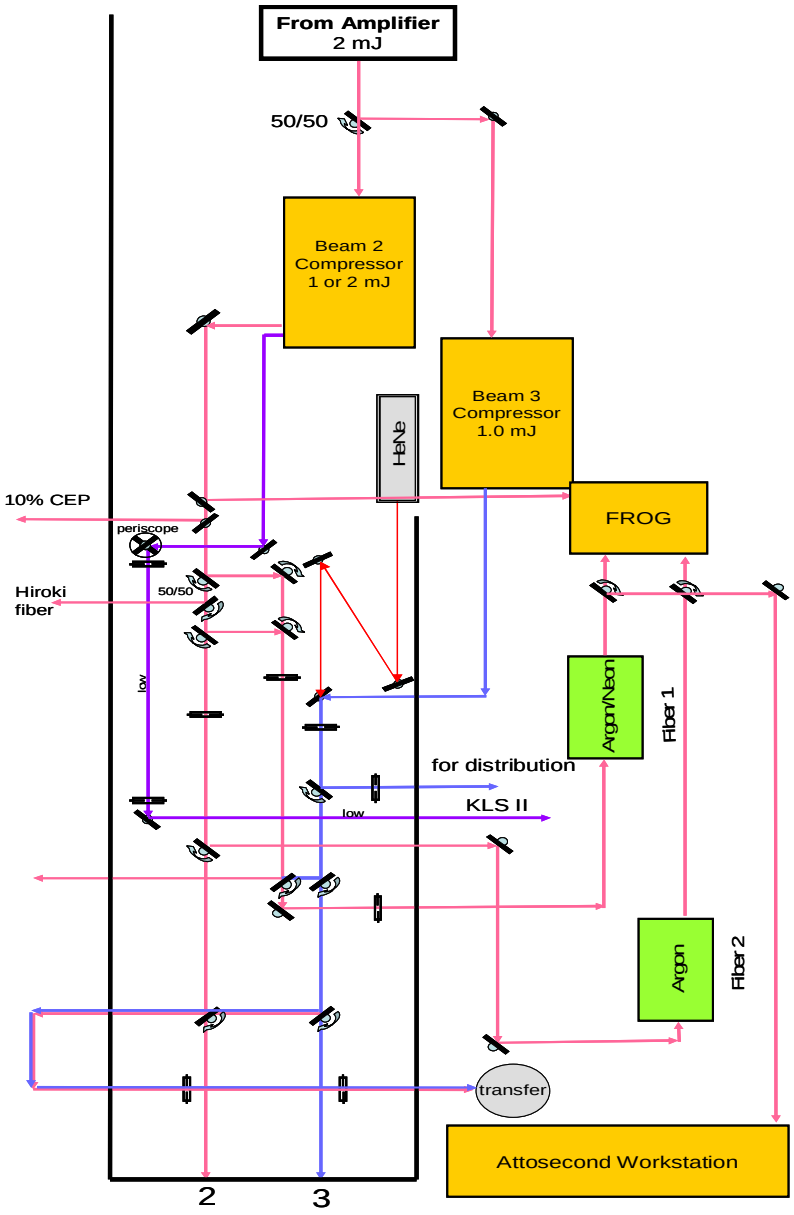

Figure A.2 Distribution of KLS beam

One half of the total output or the total output when required was delivered to fiber 1 or 2 according to the beam time schedule. Schematic representation of the complete layout for the distribution of the KLS beam is shown in Figure A.2. The output beam from the fibers was led to

the experiments, for example to the Attosecond Workstation as shown in this diagram. This beam could also be directed towards the FROG for its characterization. The entrance at the Attosecond Workstation was 5 meters away from the FROG. This distance was important for taking into consideration the dispersion caused by air. For best possible results, the chirp mirrors were installed close to the work station.

Appendix B- Detail of the Calculation on Streaking

The Streaking of the photoelectrons at different phase of the ellipticity varying laser field was done as following. First, the measured XUV supercontinuum with polarization gating, for example the fourth picture in Figure 3.6 (b) was multiplied with the scattering cross-section of the Ne gas. This resulted in to a 2d map of momentum of the photoelectron in absence of laser. Second, the final momentum of the electron after being streaked at different phase of the ellipticity dependent pulse was calculated. Since the attosecond pulse has a fixed duration, for example we supposed a duration of100 as, it needed consideration of the sum of the streaks at several points within the duration of the pulse. The following code was used for this calculation which needs the XUV supercontinum as the input file.

```
#include <iostream.h>
#include <iomanip.h>
#include <math.h>
#include <stdio.h>
#include <fstream.h>
#include <stdlib.h>
int main()
{
      double hv[1024]={0.0}, intensity[1024]={0.0}, beta[1024] = {0.0};
      double P_array[201]={0.0}; //two arrays to hold the coordinates for the
final image
      double count[201][201], count_coneLimitation[201][201];      //2d array
to hold count # [Pz_f][Py_f]
      int max_points = 100; // when changing this number, the step also needs
change so that the momentum range can be kept the same.
      for (int q = 0; q <= max_points; q++)
      {
                  P_array[q] = q*0.04 - 2.0;

                for (int k = 0; k <= max_points; k++)
            //
                  {
                  //
                        count[q][k] = 0.0;
                  }//

      }

      //input intensity (supercontinuum x-ray spectrum * CS)
      ifstream MapDataIn("xrayInt_Ne2pCS_beta.dat");        //

      for (int i = 1; i <= 1024; i++)                                     //
      {
      //
        MapDataIn >> hv[i] >> intensity[i] >> beta[i];
    }
      //
```

```
      double PI = 3.14159265;
      double e = -1.602e-19;
      double m_e = 9.1e-31; //mass of electron
      double Py_i = 0.0, Pz_i = 0.0, Py_f = 0.0, Pz_f = 0.0; // initial and
final momentum of y and z direction in a.u.

      double lamda = 800e-9; //laser wavelength
      double c = 2.9979e+8; //speed of light
      double E_0 = sqrt(3e13/1.33e-3)*100; //maximum laser electric field
envelope = sqrt(I/1.33e-3)
      //double E_0 = 0.0; // no laser --> no shift
      double tauL = 8e-15;//FWHM of laser intensity
      double T = lamda/c;
      double halfAcceptanceAngle = 45.0;

      //@@@@@@@@@@@@@@@@@@@@@@@@@@@@@@@@@@@@@@@@@@@@@@@@@@@@@@@@@@@@@
      double t_d_0 = 0.0;//  delay with no shift.                 @
      //double t_d_0 = T/8;                                         @
      //double t_d_0 = T/4; delay with maximum shift                @
      //double t_d_0 = T/2; delay with minimum shift/               @
      //double t_d_0 = 6.35e-15;//see the momentum rotation clearly @
      //double t_d_0 = 5.34e-15;//max shift in Py/                  @
      //double t_d_0 = 2.0/8.0*T; //                                  @
      //@@@@@@@@@@@@@@@@@@@@@@@@@@@@@@@@@@@@@@@@@@@@@@@@@@@@@@@@@@@@@

      double Td = 8.0e-15; // delay between the two circular laser pulses

      //double Xi = 2.56;
      //double tauX = 412e-18;//FWHM of x-ray intensity
      double Xi = 0.0; //(transform limited)
    double tauX = 150e-18;// when Xi = 0 (transform-limited)


      double omegaL = 2*PI*c/lamda; // angular velocity of laser phase
      double sigma = 2*0.693/(pow(tauX,2));
      double h = 6.626e-34;
      double h_bar = h/(2*PI);


      double shift_Py = 0.0;
      double shift_Pz = 0.0;
      double t_d = 0.0;
      double hv_chirpPulse = 0.0; // calculate energy of different
                              // places on a pulse with energy hv[i]
      double P_chirp = 0.0; // momentum corresponding to hv_chirpPulse
      double I_chirp = 0.0;  //the intensity (hv spectrum * cs) corresponding
to the hv_chirpPulse
      double beta_chirp = 0.0;

      double term1 = 0.0;
      double term2 = 0.0;


      for (i = 1; i <= 1024; i++) //1024 x-ray pulses, each with different
energies (1-1024: 34.724-60.338 eV)
      {
```

```
            for (double j = 0; j <= tauX*1e18/5; j++) // select points on
each x-ray pulse
                  //for (double j = ; j <= tauX*1e18/10; j++) // calculate
with the x-ray pulse as no duration

            {

                  t_d = t_d_0 + (j-tauX*1e18/10)*20*1e-18; // delay times for
each points

//(- 200 as) -- (+ 200 as) around the x-ray pulse peak
                  term1 = exp(-2*0.693*pow((t_d - Td/2)/tauL,2));
                  term2 = exp(-2*0.693*pow((t_d + Td/2)/tauL,2));

                  shift_Pz = -(e/omegaL)*E_0*(term1 +
term2)*sin(omegaL*t_d)/(1.993e-24); //Py shift

//for each points due to laser field

                  shift_Py = (e/omegaL)*E_0*(term1 -
term2)*cos(omegaL*t_d)/(1.993e-24);

                  hv_chirpPulse = hv[i] + 2*h_bar*sigma*Xi*(t_d -
t_d_0)/(1.602e-19);//photon energy of each point

                  P_chirp = sqrt(2*(hv_chirpPulse-21.6)/27.2); //electron
total momentum produced with hv_chirpPulse



                  //find the intensity corresponding to every hv_chirpPulse
on the x-ray spectrum
                  for (int cfi = 1; cfi <= 1024; cfi++)
                  {
                        if((hv_chirpPulse < hv[1]) || (hv_chirpPulse >
hv[1024]))
                        {
                              I_chirp = 0;
                        }
                        else
                        {
                              double difference = hv_chirpPulse - hv[cfi];

                              if (difference <= 0.0)
                              {
                                    I_chirp = intensity[cfi];
                                    beta_chirp = beta[cfi];
                                    cfi = 9999;
                              }
                        }
                  }


      ////////////////////////////////////////////////////////////////////
////
```

```
                //Calculate the final intensity of this point

                double I_xray = I_chirp*intensity[i]*exp(-
4*0.693*pow((t_d_0-t_d)/tauX,2));
                                                //chirped x-ray pulse, both
intensity and energy dependent on t_d

                for (int angle = 1; angle <= 360; angle++)
                {
                      Pz_i = P_chirp * cos(angle*2*PI/360);
                      Pz_f = Pz_i + shift_Pz;
                      Py_i = P_chirp * sin(angle*2*PI/360);
                      Py_f = Py_i + shift_Py;


                      if ((Py_f >= 0.0) && (Pz_f >= 0.0)) // in 1st
quadrant
                      {

                            for(int n = max_points/2; n <= max_points; n++)
                            {
                                  double diff_y = Py_f - P_array[n];

                                  if(diff_y <= 0.0)
                                  {
                                        for(int m = max_points/2; m <=
max_points; m++)
                                        {
                                              double diff_z = Pz_f -
P_array[m];
                                              if(diff_z <= 0.0)
                                              {
                                                    if ((Pz_i == 0.0) &&
(Py_i == 0.0))
                                                    {
                                                          count[m][n] +=
(I_xray/4/3.14)*(1 + beta_chirp*(3-1)/2);
                                                    }

                                                    count[m][n] +=
(I_xray/4/3.14)*(1 + beta_chirp*(3*Pz_i*Pz_i/(Py_i*Py_i + Pz_i*Pz_i)-1)/2);
                                                          //angular
distribytion of Ne: 0.4 @ 35 eV

                                                    m = n = 9999;
                                              }
                                        }
                                  }
                            }
                      }

                      else if ((Pz_f < 0.0) && (Py_f >= 0.0)) // in 2nd
quadrant
                      {
```

```
                        for(int n = max_points/2 - 10; n <= max_points;
n++)
                        {
                              double diff_y = Py_f - P_array[n];
                  //cout << P_array[n] << endl;

                              if(diff_y <= 0.0)
                              {
                                    for(int m = 0; m <= max_points/2 +
10; m++)
                                    {
                                          double diff_z = Pz_f -
P_array[m];
                                          if(diff_z <= 0.0)
                                          {

                                                count[m][n] +=
(I_xray/4/3.14)*(1 + beta_chirp*(3*Pz_i*Pz_i/(Py_i*Py_i + Pz_i*Pz_i)-1)/2);
                                                      //angular
distribytion of Ne: 0.4 @ 35 eV
                                                m = n = 9999;
                                          }
                                    }
                              }
                        }
                  }
                  else if ((Pz_f < 0.0) && (Py_f < 0.0)) // in 3rd
quadrant
                  {

                        for(int n = 0; n <= max_points/2 + 10; n++)
                        {
                              double diff_y = Py_f - P_array[n];

                              if(diff_y <= 0.0)
                              {
                                    for(int m = 0; m <= max_points/2 +
10; m++)
                                    {
                                          double diff_z = Pz_f -
P_array[m];
                                          if(diff_z <= 0.0)
                                          {

                                                count[m][n] +=
(I_xray/4/3.14)*(1 + beta_chirp*(3*Pz_i*Pz_i/(Py_i*Py_i + Pz_i*Pz_i)-1)/2);
                                                      //angular
distribytion of Ne: 0.4 @ 35 eV
                                                m = n = 9999;
                                          }
                                    }
                              }
                        }
                  }

                  else if ((Pz_f >= 0.0) && (Py_f < 0.0)) // in 4th
quadrant
```

```
                        {

                              for(int n = 0; n <= max_points/2 + 10; n++)
                              {
                                    double diff_y = Py_f - P_array[n];
                                    if(diff_y <= 0.0)
                                    {
                                          for(int m = max_points/2 - 10; m <=
max_points; m++)
                                          {
                                                double diff_z = Pz_f -
P_array[m];
                                                if(diff_z <= 0.0)
                                                {

                                                      count[m][n] +=
(I_xray/4/3.14)*(1 + beta_chirp*(3*Pz_i*Pz_i/(Py_i*Py_i + Pz_i*Pz_i)-1)/2);
                                                            //angular
distribytion of Ne: 0.4 @ 35 eV
                                                      m = n = 9999;
                                                }
                                          }
                                    }
                              }
                        }//close angle loop



            }//close j (points on one x-ray pulse)
            cout << i << "/1024" << endl;



      } //close i (x-ray pulses with different hv's)

      for (int o = 0; o <= max_points; o++)
      {
            for (int k = 0; k <= max_points; k++)
            {

                  if (P_array[o] > 0)
                  {
                        count_coneLimitation[o][k] = 0.0;
                  }

                  else if ((P_array[o] <= 0) && ((P_array[k]/P_array[o] < -
tan(halfAcceptanceAngle/180.0*PI)) || (P_array[k]/P_array[o] >
tan(halfAcceptanceAngle/180.0*PI))))
                  {
                        count_coneLimitation[o][k] = 0.0;
                  }
                  else
                  {
                        count_coneLimitation[o][k] = count[o][k];
                  }
```

```
		}
	}

	FILE *MapDataOut1 = fopen("zzMapData1.txt","w");// output to be saved
in this file


	for (o = 0; o <= max_points; o++)
	{
		for (int k = 0; k <= max_points; k++)
		{
			if (count[o][k] < 0)
			{
				count[o][k] = 0.0001;
			}
			fprintf(MapDataOut1,"%f\t",P_array[o]);
			fprintf(MapDataOut1,"%f\t",P_array[k]);
			//fprintf(MapDataOut1,"%f\t",count_coneLimitation[o][k]);
			fprintf(MapDataOut1,"%f\n",count[o][k]); // count[P_z][P_y]
		}
	}


	fclose(MapDataOut1);

	FILE *MapDataOut2 = fopen("zzMapData2.txt","w");// output to be saved
in this file


	for (o = 0; o <= max_points; o++) //Pz
	{
		for (int k = 0; k <= max_points; k++)
		{

			fprintf(MapDataOut2,"%f\t",P_array[o]);
			fprintf(MapDataOut2,"%f\t",P_array[k]);
			fprintf(MapDataOut2,"%f\n",count_coneLimitation[o][k]);

		}
	}


	fclose(MapDataOut2);
	cout << "Output has been stored in file: 'zzMapdata.txt'." << endl;

	return 0;
}// close main()
```

Appendix C- Constant-Fractional Discriminator

The purpose of using this module was to provide constant- fraction timing on fast signals independent of their amplitude. The front panel of this module and an optical analogy of the circuits inside this module are presented in Figure C.1. This model can incorporate 4 independent channels consisting of same circuits.

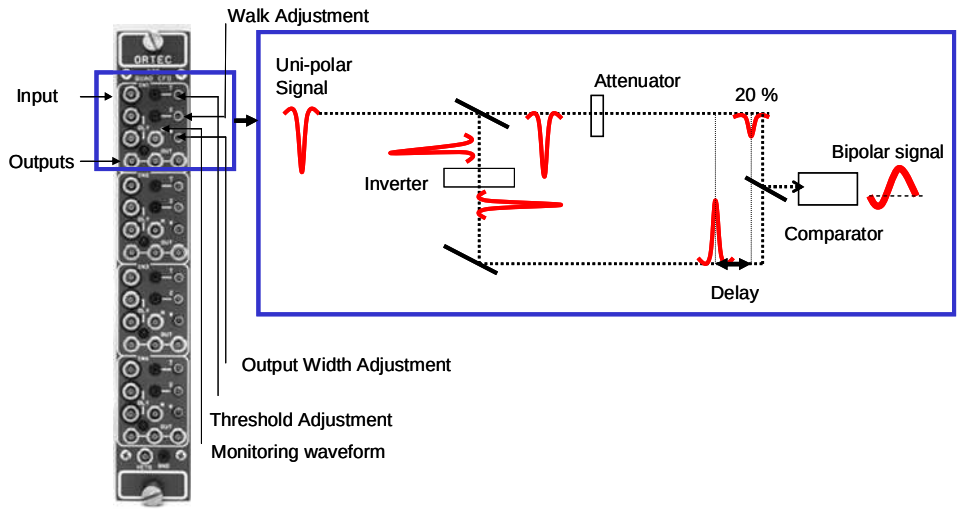

Figure C.1 Constant-Fraction Discriminator, Front panel of Model 935 and its circuit.

The original signal is split into two equal halves; one is inverted and delayed while the other half is attenuated to its 20%. After adding these two halves for a proper delay, a “zero crossing” occurs at the rising edge of the pulse. The timing of “zero crossing” can be controlled by choosing different lengths of the external delay cables in this module. We performed measurements with several delay cables and monitored the corresponding “zero crossings”. Two such waveforms for different external delays of 0.5 and 7.5 ns were as shown in Figure C.2 (a) and (b) respectively. The latter was chosen as a more appropriate delay for all of the signals from the MCP and delay-line anodes. The walk adjustment on the front panel of the CFD allowed fine

tuning of the “zero crossing”. The adjustment of the thresholds of the discriminators was done to reject low-level noise. They were adjusted by monitoring the zero crossing waveforms in such a way that the signal was triggered just above the noise level. This was critical in order to collect the most useful data. After these adjustments it was ensured that the count rate on every channel was the same with an error of $\pm$ 10%.

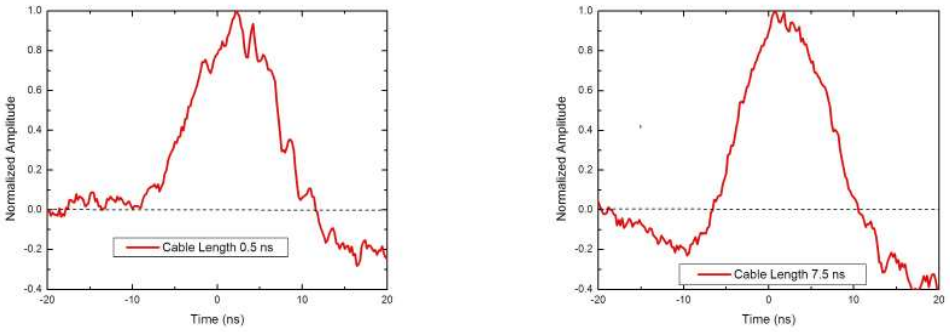

(a) (b)

Figure C.2 .Monitoring zero crossing of CFD (a) for shorter cable length ~0.5 ns (b) for a longer cable length ~7.5 ns.

Appendix D- Time to Digital Converter

A time to digital converter (TDC), LeCroy 3377 was used for digitizing all the signals, four positions from the delay line anode, and one time from the MCP. It had resolution of 0.5 ns and maximum full scale of 32 μs. It had a total of 32 channels. It was capable of recording a maximum of 16 hits at their leading edges on every channel. The dead time was 1.9 μs. The front panel of this module is shown in Figure C. The first slot out of 4 was for the common stop signal and the second slot in the rectangular box in the figure was for 16 channels. The numbers of hits on every position and time signals are shown in this figure. Most of the time there is only 1 hit on all the signals. During the acquisition, for every start signal there may or may not be all 5 stop signals. If there are, then that means no missing channels; otherwise there will be some missing channels. The last plot in this figure shows that for most of the counts, there are no missing channels. We call these good hits, but there are still significant counts for which either one or more channels are missing, which are bad hits. We discarded data which had more than 2 channels missing while re-sorting.

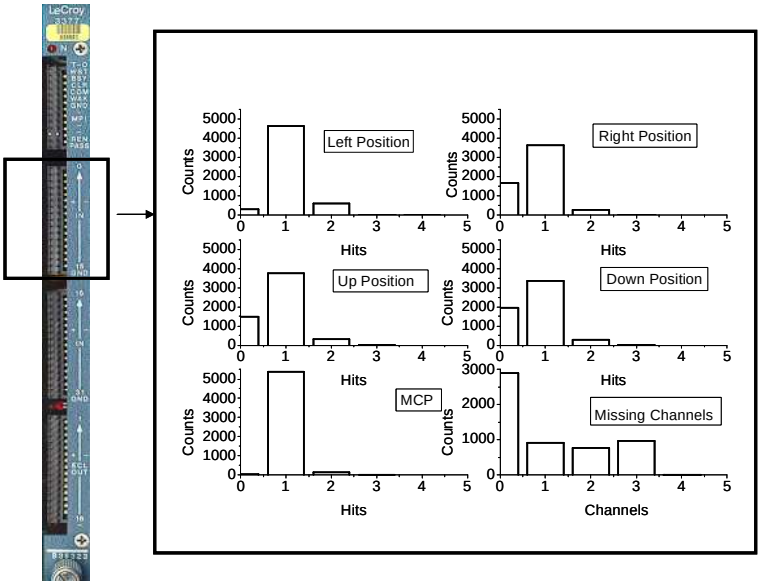

Figure D. Time to Digital Converter and hits. Front Pannel of LeCroy 3377 TDC. The number of hits for four positions and 1 time signal. The last plot shows the number of missing channels for such hits.

Appendix E - Reconstruction Codes

E.1 Analyse.f

```
C------Attosecond Work Station----------------------Electron Measurement-----
------------------
      subroutine analyse(tdc,cnt,counts,adc,nadc,scl,nscl,param)

C ---------------------------------------------------------------------------
-
      implicit none

      integer*4 cnt(32), adc(*),scl(*),nscl,nrec, nel, energy, counts(*),
mu1, mu2, qu1, qu2
      integer ln, rn, tn, bn, cpn, nadc, param
      real tdc(32,16),flux
      real tim, m1, m2, q1, q2, xshift, yshift, x, shift
      !********************
      real s1, E1, z, s2, E2, E, s, q     !********************
      real a1, a2, t1, t2
      real xe, xe_0, ye, ye_0, etof, t, te_0, edx, edy, gxe, gye, re
      real xr1, xr_0, yr1, yr_0, rtof1, rtof2, xr2, yr2, gxr, gyr
      real xesum, yesum, xesd, yesd, xrsum, yrsum, xrsd, yrsd
      real pxe, pye, pze, pze2, pp, pe, totale, totalr, temp, temp2
,tsumx,tsumy,ta
      real tof_to_pe, rndm, coss          ! function
      double precision cubic  ! function
      real vy1, vy2, vz1, vz2
      real cosfi, fi, cosbt, betta, v1, v2
      real alpha, pxe_prime, pye_prime, theta, theta_prime, inc, dalpha
      real pxr(2), pyr(2), pzr(2), ppr, pr, prrx, prry, prrz, prrz2
      real rec(3,16),el(3,16)
      real omega, c
      real onex(16),twox(16),oney(16),twoy(16),cp(16),ec,xcm,ycm
      integer left, right, up, down, mcp, i
      real pau, vjet, PI, me, mu
      real nx, ny, nz
      parameter (PI=3.14159265359)
      parameter (mu=1.661E-27)
      parameter (me=9.1094E-31)
      data omega/0.0528/!for 5V
      data pau/1.993E-24/     !a.u. of momentum
      data ec/1.602E-19/
      data xesum/-141.1/
      data xesd/4.6/
      data yesum/-136.6/
      data yesd/4.1/
      data gxe/0.79365/   ! velocity 1.26 nsec/mm
      data gye/0.83333/     !velocity 1.2 nsec/mm
      data te_0/1.54/ ! from fit
      data ye_0/40.148/
      data xe_0/2.0/
      vjet=9.E-4  !gyr*(delta(ns))/tof(ns)

      mu1 = 14 ! CH2+
```

```
      mu2 = 14 ! CH2+
      qu1 = 1
      qu2 = 1
c       **********************************
c       the following is very important -
c       reversing the axis sign does not just reverse the picture
c       or the direction of rotation, it also makes the pictures worse
c       ______________________________________
      left = 1
      right = 2
      down = 3
      up = 4
      mcp = 10
c       **********************************

      ln = cnt(left)
      do i=1,cnt(left)
          onex(i)=tdc(left,i)+.5*rndm()
      enddo
      rn = cnt(right)
      do i=1,cnt(right)
          twox(i)=tdc(right,i)+.5*rndm()
      enddo
        bn = cnt(down)
      do i=1,cnt(down)
          oney(i)=tdc(down,i)+.5*rndm()
      enddo
        tn = cnt(up)
      do i=1,cnt(up)
          twoy(i)=tdc(up,i)+.5*rndm()
      enddo
        cpn = cnt(mcp)
      do i=1,cnt(mcp)
          cp(i)=tdc(mcp,i)+.5*rndm()
      enddo
      nel = 2
        call resort(nel,cp,cpn,onex,ln,twox,rn,
     *                                 oney,bn,twoy,tn,
     *                                 xesum,yesum,xesd,yesd,
     *                                 el)

      if(nel.lt.1.) return
         tsumx= 2*tdc(10,1)-tdc(1,1)-tdc(2,1)
         tsumy= 2*tdc(10,1)-tdc(3,1)-tdc(4,1)
        call hf1(11,tsumx,1.)
          call hf1(12,tsumy,1.)

      xe = gxe*el(2,1)
      ye = gye*el(3,1)

      etof = tdc(11,1)-el(1,1)-te_0
c ------------**************************------------------
c*********************** Electron momentum**************
      t   =  etof !ns ( minus the node position )
      edx = gxe*(el(2,1)-xe_0)
      edy = gye*(el(3,1)-ye_0)
      re = sqrt(edx**2+edy**2)
```

```
      c = tan(omega*t/2.)
      pxe = 5.E5*me*omega*(edx/c + edy)/(2*pau) !counter clockwise
      pye = 5.E5*me*omega*(edy/c - edx)/(2*pau)! clockwise

      pp = 5.E5*me*omega*(re)/abs(2*sin(omega*t/2.)*pau)
c-------------------------------------
      s=0.1688          !m
      E=0.           !V/m
      shift = 10.01     !due to the third acc. region

      q=1.*ec
      pze=-(1.E9*me*s/etof)/pau

c--------------------------------------
      pe = sqrt(pp*pp+pze*pze)
      totale=27.2*pe**2/2
C ----------------histograms----------------
      if(xe.ne.0.or.ye.ne.0) then
         call hf2(100,edx,edy,1.)
         call hf1(150,etof,1.)
         call hf2(200,etof,re,1.)
         call hf2(201,etof,el(2,1),1.)
         call hf2(202,etof,el(3,1),1.)
         call hf1(740,pe,1.)
         call hf2(710,pxe,pye,1.)
         call hf2(715,pze,pe,1.)
c     *************slicing
         if(abs(pxe). lt. 0.2)  call hf2(720,pye,pze,1.)
         call hf2(725,pye,pe,1.)
         call hf2(735,pze,pe,1.)
c     **************slicing
      if(abs(pye). lt. 0.2)   call hf2(730,pze,pxe,1.)
        call hf2(736,pze,pp,1.)
        call hf1(2500,totale,1.)

      left = 5
      right = 7
      down = 6
      up = 8
      mcp = 9
c       ***********************************
      do i=1,cnt(left)
          onex(i)=tdc(left,i)+.5*rndm()
      enddo
      do i=1,cnt(right)
          twox(i)=tdc(right,i)+.5*rndm()
      enddo
      do i=1,cnt(down)
          oney(i)=tdc(down,i)+.5*rndm()
      enddo
      do i=1,cnt(up)
          twoy(i)=tdc(up,i)+.5*rndm()
      enddo
      do i=1,cnt(mcp)
          cp(i)=tdc(mcp,i)+.5*rndm()
      enddo
      nrec = 16
```

```
        call resort(nrec,cp,cnt(mcp),onex,cnt(left),twox,cnt(right),
     *                                  oney,cnt(down),twoy,cnt(up),
     *                                  xrsum,yrsum,xrsd,yrsd,
     *                                  rec)
       if(nrec.lt.2)return

       endif
       end

C-------------------------------------------------------------------------
       subroutine booking(histfile)
C-------------------------------------------------------------------------

       parameter (nwpawc=4000000)
       common /pawc/ hmemor(nwpawc)
         common /quest/iquest(100)
       character*80 histfile
       real PI
       parameter (PI=3.14159265359)

       call hlimit(nwpawc)
c      print *,'Subroutine: booking...'
       call htitle('ALS98 offline analyse')
         iquest(10)=65000                        !record length of hbook file
       call hropen(1,'als98',histfile,'NQ',2048,istat)
       if (istat .ne. 0) then
          stop 'Error in opening hbook file'
       endif
       call hbook1(11,'tsumx',16000,0.,3000.,0.)
       call hbook1(12,'tsumy',16000,0.,3000.,0.)
       call hbook2(100,'xy e',400,-120.,120.,400,-120.,120.,0.)
       call hbook1(150,'etof',2000,40.,100.,0.)
       call hbook2(200,'wiggles',600,30.,250.,201,0.,100.,0.)
       call hbook2(201,'xfish',600,0.,300.,201,-100.,100.,0.)
       call hbook2(202,'yfish',600,0.,300.,201,-100.,100.,0.)
       call hbook2(710,'e px py',200,-1.,1.,200,-1.,1.,0.)
       call hbook2(720,'e py pz',200,-0.3,0.3,100,-1.5,-0.9,0.)
       call hbook2(730,'e pz px',100,-1.5,-0.8,200,-0.4,0.4,0.)
       call hbook2(736,'e pze pp',200,-1.6,-0.,200,0.,1.6,0.)
       call hbook1(740,'pe',201,0.,3.,0.)
       call hbook1(2500,'el E total',200,0.,36.,0.)
       end

C-------------------------------------------------------------------------
       subroutine polar(alpha, betta, irange, hist, step, hnum, inc)
C-------------------------------------------------------------------------
       implicit none
       real alpha, betta, irange, step, inc ! all in degrees
       integer hist, hnum, i
       real center, bin, alpha1
       integer low, high, ceil
       low = max(0,ceil((alpha-irange/2)/step))

       if(alpha+irange/2.gt.0) then
           high = min(hnum,int((alpha+irange/2)/step))
           alpha1 = alpha
       else
```

```
          high = hnum
          low = max(0,ceil((alpha+360.-irange/2)/step))
          alpha1 = alpha+360.
        endif
        if(high.lt.low) return
        do i=low, high
          center = i*step
          bin = betta+center
          if(bin.lt.-180..or.bin.gt.180.) then
            bin = mod(bin, 360.)
            if (bin.gt.180.) bin = bin - 360.
            if (bin.lt.-180.) bin = bin + 360.
          endif
          if(bin.lt.-180..or.bin.gt.180.) print *,'***', bin
          call hf1(hist+i,bin,inc)
          call hf1(hist+400+i,bin,inc**2)
          if(bin.ge.0)call hf1(hist+i,bin-180.,inc)
          if(bin.ge.0)call hf1(hist+400+i,bin-180.,inc**2)
          if(bin.le.0)call hf1(hist+i,bin+180.,inc)
          if(bin.le.0)call hf1(hist+400+i,bin+180.,inc**2)
        enddo
        end
C-------------------------------------------------------------------------
        real function tof_to_pe(tof)
C-------------------------------------------------------------------------
        implicit none
        real tof, pau
        real s1,e1,s2,e2,q,m
        real a1,a2,t,t1,result
        real cubic  ! function
        pau = 1.993E-24 ! 1 a.u. of momentum
        q = 1.602E-19
        m = 9.1094E-31
        s1 = .240         !m
c       E1 = 100.0        ! v/m
c       E1 = 200.0        ! v/m
        E1 = 1200.0       ! v/m
        s2 = .00801
        E2 = 100000.0
        a1 = q*E1/m
        a2 = q*E2/m
        t = tof*1.E-9           ! to get time in secs
        t1 = cubic(t*(2*a2-a1)/(a1-a2), ! general case
       *          (2*s1+2*s2-a2*t*t)/(a1-a2),t*2*s1/(a2-a1))
        result = m*(s1/t1-a1*t1/2.)
        tof_to_pe = result/pau
        end

C-------------------------------------------------------------------------
        subroutine normal(x1, y1, z1, x2, y2, z2, nx, ny, nz)
C-------------------------------------------------------------------------
          implicit none
          real x1, y1, z1, x2, y2, z2, nx, ny, nz, x, y, z
          real l1, l2, l3
          x = (y1*z2-y2*z1)
          y = (z1*x2-z2*x1)
          z = (x1*y2-x2*y1)
```

```
          l1 = sqrt(x1*x1+y1*y1+z1*z1)
          l2 = sqrt(x2*x2+y2*y2+z2*z2)
          l3 = sqrt(x*x+y*y+z*z)
          if(l1.eq.0.or.l2.eq.0.or.l3.eq.0.) then
            nx = 0.
            ny = 0.
            nz = 0.
          else
            nx = x/l3
            ny = y/l3
            nz = z/l3
          endif
      end
C-------------------------------------------------------------------------
        real function coss(x1, y1, z1, x2, y2, z2)
C-------------------------------------------------------------------------
           implicit none
           real x1, y1, z1, x2, y2, z2
             real scal, l1, l2
             scal = x1*x2+y1*y2+z1*z2
             l1 = sqrt(x1*x1+y1*y1+z1*z1)
             l2 = sqrt(x2*x2+y2*y2+z2*z2)
             if(l1.eq.0..or.l2.eq.0.) then
                 coss = 0.
             else
                 coss = scal/(l1*l2)
             endif
        end


C-------------------------------------------------------------------------
      integer function ceil(x)
C-------------------------------------------------------------------------
          implicit none
          real x
          if(x-int(x).eq.0.) then
            ceil = int(x)
          else
            ceil = int(1.+x)
          endif
      end
C-------------------------------------------------------------------------
      subroutine histout
C-------------------------------------------------------------------------

c     call hindex
c     call hrput(0,histfile,'N')
      call hrout(0,icycle,' ')
      call hrend('als98')
      close(1)
      end

C-------------------------------------------------------------------------
      real function cubic(a,b,c)
c       the real root of the cubic equation with coefficients 1,a,b,c
c       MAKE SURE TO CHOOSE THE RIGHT ROOT IN CASE OF 2 OR 3 REAL
C-------------------------------------------------------------------------
```

```
        implicit none
      real a, b, c
        double precision n, aa, bb, cc, q, r, d, s, t, z, z2, z3, PI
      PI = 3.14159265359
        n = EXP(((log(sqrt(a*a))+2*log(sqrt(b*b))
     *            +3*log(sqrt(c*c))))/14.)
c     print *,n
      aa = a/n
        bb = b/n**2
        cc = c/n**3
c     print *, '*', n, aa, bb, cc
      q = (3.*bb-aa*aa)/9.
      r = (9.*aa*bb-27.*cc-2.*aa*aa*aa)/54.
      d = q*q*q + r*r
c     print *,q,r,d
      if(d.le.0.)then
           t = acos(r/sqrt(-q*q*q))
           z3 = 2.*sqrt(-q)*cos(t/3.) - aa/3 !real root #1 right most
           z2 = 2.*sqrt(-Q)*cos((T+2.*PI)/3.) - aa/3.; ! real root #2
           z = 2.*sqrt(-Q)*cos((T+4.*PI)/3.) - aa/3.; ! real root #3 same if
D=0
c          print *,'all real', n*z, n*z2, n*z3
      else
           if(r+sqrt(d).gt.0.) then
            s = (R+sqrt(D))**(1./3.)
           else
            s = -(-R-sqrt(D))**(1./3.)
           endif
           if(r-sqrt(d).gt.0.) then
            t = (R-sqrt(D))**(1./3.)
           else
            t = -(-R+sqrt(D))**(1./3.)
           endif
           z = s + t - aa/3.
      endif
c     print *, z, n
c     read *
      cubic = z*n
      end
```

E.2 Resort.f

```
C---------------Attosecond Work Station-----------resorting routines---------
-----
      subroutine resort(n,cp,cpn,l,ln,r,rn,d,dn,u,un,hts,vts,hsd,vsd,result)
C-------------------------------------------------------------------------
----
      common/resort_blck/error
      real error

      integer*4 n, cpn, ln, rn, un, dn ! number of hits to reconstract +
                                       ! number per every channel below
      real cp(*),l(*),r(*),u(*),d(*)   ! channel plate, left, right, up, down
```

```
      real hts, vts, hsd, vsd  ! horisontal(vertical) timesum and standard
deviation
      real result(3,*)           ! (t, x, y) times (modified n)

      real v, h, totalv, totalh, total
      integer*4 pairx(2,16), pairy(2,16), four(4), m, ti(16), bti(16)
      integer*4 bpairx1(16), bpairy1(16),bpairx2(16), bpairy2(16),p
C-------------------------functions-----------------------------------------
---
      real bestpair
      real besttime

      totalv = error
      error = abs(hsd + vsd)
      m = min(n,cpn,ln,rn,un,dn)
      totalv = error
      totalh = error


      do k=m,1,-1       ! Starting from maximum k possible
          total = error*k
          totalh = error*k
          totalv = error*k
          i=1
          ll=1
10        j=ll          !(do j=ll,cpn-k+i)
                        !(do j=ll,cpn-k+i) ! Does not work with do loop
20        ti(i)=j
          if(i.lt.k) then
            ll=j+1
            i=i+1
            goto 10
          else
            h = bestpair(ti,k,cp,l,ln,r,rn,hts,pairx)
            v = bestpair(ti,k,cp,d,dn,u,un,vts,pairy)

            if(v.ge.0.and.h.ge.0.and.v.lt.totalv.and.h.lt.totalh)then
                totalv = v
                totalh = h
                do p=1,k
*,ti(p),cp(ti(p)),pairx(1,p),pairx(2,p),pairy(2,p),pairy(1,p)
                  bti(p)=ti(p)
                  bpairx1(p) = pairx(1,p)
                  bpairx2(p) = pairx(2,p)
                  bpairy1(p) = pairy(1,p)
                  bpairy2(p) = pairy(2,p)
                enddo
            endif
          endif
30        j=j+1         !(enddo)
          if(j>cpn-k+i) then  !(enddo)
            goto 40           !(enddo)
          else          !(enddo)
            goto 20           !(enddo)
          endif
40        if(i.gt.1.and.ti(i-1).lt.cpn-k+i) then
            i=i-1
```

```
            j=ti(i)
            goto 30
          endif
C ---------------------------- (cpn choose k) ------------------------------
-
          if(totalv.lt.total.and.totalh.lt.total) then

            goto 50
          endif
      enddo


50    continue
      do p=k,1,-1
*,p,bti(p),cp(bti(p)),bpairx1(p),bpairx2(p),bpairy1(p),bpairy2(p)
          result(1,p)=cp(bti(p))
          result(2,p)=r(bpairx2(p))-l(bpairx1(p))
          result(3,p)=u(bpairy2(p))-d(bpairy1(p))
c         print *,result(1,p),result(2,p),result(3,p)
      enddo
      call sorti(bpairx1,k)
      call sorti(bpairx2,k)
      call sorti(bpairy1,k)
      call sorti(bpairy2,k)
      call reduse(l,ln,bpairx1,k)
      call reduse(r,rn,bpairx2,k)
      call reduse(d,dn,bpairy1,k)
      call reduse(u,un,bpairy2,k)
      call reduse(cp,cpn,bti,k)

c     print *,k, " 0"

70    do
          v=besttime(l,ln,r,rn,d,dn,u,un,hts,vts,four)
          if(v.ge.0)then
            k=k+1
            result(1,k)=v
            result(2,k)=r(four(2))-l(four(1))
            result(3,k)=u(four(4))-d(four(3))

            call reduse(l,ln,four(1),1)
            call reduse(r,rn,four(2),1)
            call reduse(d,dn,four(3),1)
            call reduse(u,un,four(4),1)

          else
            goto 60
          endif
      enddo
60    continue

      n=k
c     print *,n, " 1"

      if(cpn.eq.1.and.(ln+rn).eq.1.and.(dn+un).eq.1) then
          n = n + 1
          result(1,n)=cp(1)
```

```
          if(ln.eq.1) then
            result(2,n)=2.*result(1,n)+hts-2.*l(1)
          else
            result(2,n)=2.*r(1)-hts-2.*result(1,n)
          endif

          if(dn.eq.1) then
            result(3,n)=2.*result(1,n)+vts-2.*d(1)
          else
            result(3,n)=2.*u(1)-vts-2.*result(1,n)
          endif
          call sortd(result,n)
          return
      endif

      if(ln.eq.0.or.rn.eq.0)then
          if((rn.ne.1.and.ln.eq.0).or.(ln.ne.1.and.rn.eq.0)) then
            call sortd(result,n)
            return
          endif
          m = min(2,cpn,un,dn)

          do k=m,1,-1         ! Starting from maximum k possible
            totalv = error*k
            i=1
            ll=1
110         j=ll        !(do j=ll,cpn-k+i)
                        !(do j=ll,cpn-k+i) ! Does not work with do loop
120         ti(i)=j
            if(i.lt.k) then
                ll=j+1
                i=i+1
                goto 110
            else
                v = bestpair(ti,k,cp,d,dn,u,un,vts,pairy)
                if(v.ge.0.and.v.lt.totalv)then
                  totalv = v
                  if(k.gt.1) then
                      call sortd(result,n)
                      return
                  endif
                  bti(1)=ti(1)
                  bpairy1(1) = pairy(1,1)
                  bpairy2(1) = pairy(2,1)
                endif
            endif
130         j=j+1       !(enddo)
            if(j>cpn-k+i) then !(enddo)
                goto 140      !(enddo)
            else        !(enddo)
                goto 120      !(enddo)
            endif
140         if(i.gt.1.and.ti(i-1).lt.cpn-k+i) then
                i=i-1
                j=ti(i)
                goto 130
            endif
```

```
C       ---------------------------- (cpn choose k) ------------------------
-------
          enddo
          if(totalv.lt.error) then
            n=n+1
            result(1,n)=cp(bti(1))
            if(ln.eq.0)then
                result(2,n)=2.*r(1)-hts-2.*result(1,n)
                call reduse(r,rn,bpairx2(p),1)
            else
                result(2,n)=2.*result(1,n)+hts-2.*l(1)
                call reduse(l,ln,bpairx1,1)
            endif
            result(3,n)=u(bpairy2(1))-d(bpairy1(1))
            call reduse(cp,cpn,bti,1)
            call reduse(u,un,bpairy2,1)
            call reduse(d,dn,bpairy1,1)
          else
            if(dn.eq.1.and.un.eq.1)then
                n=n+1
                result(1,n)=(d(1)+u(1)-vts)/2.
                if(ln.eq.0)then
                  result(2,n)=2.*r(1)-hts-2.*result(1,n)
                else
                  result(2,n)=2.*result(1,n)+hts-2.*l(1)
                endif
                result(3,n)=u(bpairy2(1))-d(bpairy1(1))
            else
                call sortd(result,n)
                return
            endif
          endif
      endif

c     print *,n, " 2"

      if(dn.eq.0.or.un.eq.0)then
          if((dn.eq.0.and.un.ne.1).or.(un.eq.0.and.dn.ne.1))  then
            call sortd(result,n)
            return
          endif
          m = min(2,cpn,ln,rn)
          do k=m,1,-1         ! Starting from maximum k possible
            totalh = error*k
            i=1
            ll=1
210         j=ll        !(do j=l,cpn-k+i)
                        !(do j=l,cpn-k+i) ! Does not work with do loop
220         ti(i)=j
            if(i.lt.k) then
                ll=j+1
                i=i+1
                goto 210
            else
                h = bestpair(ti,k,cp,l,ln,r,rn,hts,pairx)
                if(h.ge.0.and.h.lt.totalh)then
                  totalh = h
```

```
                  if(k.gt.1)  then
                      call sortd(result,n)
                      return
                  endif
                  bti(1)=ti(1)
                  bpairx1(1) = pairx(1,1)
                  bpairx2(1) = pairx(2,1)
                endif
              endif
230           j=j+1       !(enddo)
              if(j>cpn-k+i) then !(enddo)
                  goto 240      !(enddo)
              else        !(enddo)
                  goto 220      !(enddo)
              endif
240           if(i.gt.1.and.ti(i-1).lt.cpn-k+i) then
                  i=i-1
                  j=ti(i)
                  goto 230
              endif
C       ---------------------------- (cpn choose k) -----------------------
-------
            enddo
c           print *,n, totalh
            if(totalh.lt.error) then
              n=n+1
              result(1,n)=cp(bti(1))
              if(dn.eq.0)then
                  result(3,n)=2.*u(1)-vts-2.*result(1,n)
                  call reduse(u,un,bpairy2,1)
              else
                  result(3,n)=2.*result(1,n)+vts-2.*d(1)
                  call reduse(d,dn,bpairy1,1)
              endif
              result(2,n)=r(bpairx2(1))-l(bpairx1(1))
              call reduse(cp,cpn,bti,1)
              call reduse(r,rn,bpairx2,1)
              call reduse(l,ln,bpairx1,1)
            else
              if(ln.eq.1.and.rn.eq.1)then
                  n=n+1
                  result(1,n)=(l(1)+r(1)-hts)/2.
                  if(dn.eq.0)then
                    result(3,n)=2.*u(1)-vts-2.*result(1,n)
                  else
                    result(3,n)=2.*result(1,n)+vts-2.*d(1)
                  endif
                  result(2,n)=r(bpairx2(1))-l(bpairx1(1))
              else
                  call sortd(result,n)
                  return
              endif
            endif
         endif

         if(min(ln,rn).eq.1.and.max(ln,rn).eq.2.and.
        *     min(dn,un).eq.1.and.max(dn,un).eq.2.and.cpn.eq.2)then
```

```
          call recover(n,cp,cpn,l,ln,r,rn,d,dn,u,un,hts,vts,hsd,vsd,result)
      endif

      call sortd(result,n)
      end


C-------------------------------------------------------------------------
---
      real function bestpair(ti,n,time,one,one_n,two,two_n,ts,pair)
C-------------------------------------------------------------------------
---
      common/resort_blck/error
      real error, total, ll
      real time(*),one(*),two(*),ts
      integer*4 ti(*), n,one_n,two_n,pair(2,16),cpair(2,16),p
      logical mark(2,16)

      real delta
C       ------------------- Initializing variables ---------------
      bestpair = -1
      total = error*n
      current = 0
      do i=1,one_n
          mark(1,i) = .false.
      enddo
      do i=1,two_n
          mark(2,i) = .false.
      enddo
C       ------------------ Looking for a best n pairs ------------
      i = 1
10    j = 1
20    k = 1
30    if(current < total) then
          if(.not.mark(1,j))then
            ll=delta(time(ti(i)),one(j),two(k),ts)
            if((.not.mark(2,k)).and.ll.lt.error) then
                mark(1,j)=.true.
                mark(2,k)=.true.
                cpair(1,i)=j
                cpair(2,i)=k
                current = current+ll
                if(i.lt.n) then
                  i=i+1
                  goto 10
                else
                  if(current.lt.total)then
                      total = current
                      do p=1,n
                        pair(1,p) = cpair(1,p)
                        pair(2,p) = cpair(2,p)
                      enddo
                  endif
                  mark(1,j)=.false.
                  mark(2,k)=.false.
                  current = current-ll
                endif
```

```
            endif
          else
            j=j+1
            if(j.gt.one_n) then
                goto 50
            else
                goto 20
            endif
          endif
      else
          goto 50
      endif
60    k=k+1
      if(k.gt.two_n) then
          goto 40
      else
          goto 30
      endif
40    j=j+1
      if(j.gt.one_n) then
          goto 50
      else
          goto 20
      endif
50    if(i.gt.1)then
          i=i-1
          j=cpair(1,i)
          k=cpair(2,i)
          current = current - delta(time(ti(i)),one(j),two(k),ts)
          mark(1,j)=.false.
          mark(2,k)=.false.
          goto 60
      endif
C -------------- STOP this mind bugling function -------------------------
      if(total.lt.error*n) bestpair=total
      end




C-------------------------------------------------------------------------
---
      real function besttime(l,ln,r,rn,d,dn,u,un,hts,vts,four)
C-------------------------------------------------------------------------
---
      common/resort_blck/error
      real error, a, b, min
      real l(*),r(*),d(*),u(*),hts,vts
      integer*4 ln, rn, un, dn, four(4), ll

      real lostcp

      min = error
      besttime = -1.
      do i=1,ln
          do j=1,rn
            do k=1,dn
```

```
                do ll=1,un
                  a = lostcp(l(i),r(j),hts)
                  b = lostcp(d(k),u(ll),vts)
c                 print *,a,b
                  if(abs(a-b) .lt. min) then
                      min = abs(a-b)
                      four(1) = i
                      four(2) = j
                      four(3) = k
                      four(4) = ll
                      besttime = (a+b)/2.
                  endif
                enddo
              enddo
            enddo
      enddo
      end

C-------------------------------------------------------------------------
---
      real function lostcp(one,two,ts)
C-------------------------------------------------------------------------
---
      real one, two, ts

      lostcp = (one + two - ts)/2.
c     print *,one,two,ts,lostcp
      end

C-------------------------------------------------------------------------
---
      real function delta(t, one, two, ts)
C-------------------------------------------------------------------------
---
      real t, one, two, ts
      delta = abs(one + two - 2.*t - ts)
      end

C-------------------------------------------------------------------------
---
      subroutine reduse(ar,n,ind,k)
C-------------------------------------------------------------------------
---
      real ar(*)
      integer*4 n, ind(*), k
      do i=k,1,-1
          do j=ind(i)+1,n
c           print *,i,j,ind(i),ar(j-1),ar(j)
            ar(j-1)=ar(j)
          enddo
          n=n-1
      enddo
      end
C-------------------------------------------------------------------------
---
      subroutine recover(n,cp,cpn,l,ln,r,rn,d,dn,u,un,hts,vts,hsd,vsd,result)
```

```
C-------------------------------------------------------------------------
---
      common/resort_blck/error
      real error, me

      integer*4 n, cpn, ln, rn, un, dn ! number of hits to reconstract +
                                  ! number per every channel below
      real cp(*),l(*),r(*),u(*),d(*)   ! channel plate, left, right, up, down
      real hts, vts, hsd, vsd  ! horisontal(vertical) timesum and standard
deviation
      real result(3,*)           ! (t, x, y) times (modified n)

      integer*4 j0,k0,a(1)
      real er
      real delta
      j0=1
      k0=1

      m = n
      if(cpn.lt.1.or.cpn.gt.2)return
      if(min(ln,rn).lt.1.or.max(ln,rn).gt.2)return
      if(min(dn,un).lt.1.or.max(dn,un).gt.2)return
      do i=1,cpn
          m = m + 1
          do j=1,3
            result(j,m)=-1000.
          enddo
          result(1,m)=cp(i)
          me = error
          do j=1,ln
            do k=1,rn
                er = delta(cp(i),l(j),r(k),hts)
                if(er.lt.me)then
                  me = er
                  j0 = j
                  k0 = k
                endif
            enddo
          enddo
          if(me.lt.error)then
            result(2,m) = r(k0)-l(j0)
            a(1)=j0
            call reduse(l,ln,a,1)
            a(1)=k0
            call reduse(r,rn,a,1)
          endif
          me = error
          do j=1,dn
            do k=1,un
                er = delta(cp(i),d(j),u(k),vts)
                if(er.lt.me)then
                  me = er
                  j0 = j
                  k0 = k
                endif
            enddo
          enddo
```

```
          if(me.lt.error)then
            result(3,m) = u(k0)-d(j0)
            a(1)=j0
            call reduse(d,dn,a,1)
            a(1)=k0
            call reduse(u,un,a,1)
          endif
       enddo
       do i=1,cpn
          if((result(2,n+i)+999.)*(result(3,n+i)+999.).lt.0)then
            if((result(2,n+i)+999.).lt.0.and.(ln+rn).eq.1)then
                if(ln.eq.1) then
                  result(2,n+i)=2.*result(1,n+i)+hts-2.*l(1)
                else
                  result(2,n+i)=2.*r(1)-hts-2.*result(1,n+i)
                endif
            endif
            if((result(3,n+i)+999.).lt.0.and.(dn+un).eq.1)then
                if(dn.eq.1) then
                  result(3,n+i)=2.*result(1,n+i)+vts-2.*d(1)
                else
                  result(3,n+i)=2.*u(1)-vts-2.*result(1,n+i)
                endif
            endif
          endif
       enddo
       if((result(2,n+1)+999.).gt.0.and.(result(3,n+1)+999.).gt.0)then
          n = n + 1
          if(cpn.eq.2.and.(result(2,n+1)+999.).gt.0
      *                  .and.(result(3,n+1)+999.).gt.0)then
            n = n + 1
          endif
       elseif(cpn.eq.2.and.(result(2,n+2)+999.).gt.0
      *                  .and.(result(3,n+2)+999.).gt.0)then
          n = n + 1
          result(1,n)=result(1,n+1)
          result(2,n)=result(2,n+1)
          result(3,n)=result(3,n+1)
       endif
       end

C-------------------------------------------------------------------------
-
       subroutine sorti(a,n)
C-------------------------------------------------------------------------
-
       integer*4 n, m, min, a(*)

       do i=1,n
          min = a(i)
          m = i
          do j=i,n
            if(a(j).lt.min) then
                min = a(j)
                m = j
            endif
          enddo
```

```
          if(m.ne.i) then
            a(m) = a(i)
            a(i) = min
          endif
      enddo
      end
C-------------------------------------------------------------------------
-
      subroutine sorta(result,n)
C-------------------------------------------------------------------------
-
      real result(3,*),min
      integer*4 n,j0

      min = result(1,1)

      do i=1,n
          j0 = i
          min = result(1,i)
          do j=i+1,n
            if(n.ge.j.and.result(1,j).lt.min)then
                min = result(1,j)
                j0=j
            endif
          enddo
          do j=1,3
            if(j0.gt.i)then
                min = result(j,j0)
                result(j,j0)=result(j,i)
                result(j,i)=min
            endif
          enddo
      enddo
      end
C-------------------------------------------------------------------------
-
      subroutine sortd(result,n)
C-------------------------------------------------------------------------
-
      real result(3,*),max
      integer*4 n,j0

      max = result(1,1)

      do i=1,n
          j0 = i
          max = result(1,i)
          do j=i+1,n
            if(n.ge.j.and.result(1,j).gt.max)then
                max = result(1,j)
                j0=j
            endif
          enddo
          do j=1,3
            if(j0.gt.i)then
                max = result(j,j0)
                result(j,j0)=result(j,i)
```

```
          result(j,i)=max
        endif
      enddo
enddo
end
```

Appendix F – List of Publications

F.1 Journals

1) Shambhu Ghimire, Bing Shan, Chun Wang, and Zenghu Chang, "High-Energy 6.2-fs pulses for attosecond pulse generation", LASER PHYSICS, 15, 6, (2005)

2) Chakra Man Maharjan , Ali Alnaser , Xieo-Min. Tong , Brite Ulrich , Predrag Ranitovic , Shambhu Ghimire , Zenghu Chang , Igor Litvinyuk , Lew Cocke , "Momentum imaging of doubly charged ions of Ne and Ar in the sequential ionization region", PHYSICAL REVIEW A 72 (4): OCT (2005).

3) Ali Alnaser , Brite Ulrich , Xieo-Min Tong , Igor Litvinyuk, Chakra Man Maharjan , Predrag Ranitovic , Timur Osipov T, R Ali , Shambhu Ghimire, Zenghu Chang , Chi Dong Lin , Cocke C. Lewis, "Simultaneous real-time tracking of wave packets evolving on two different potential curves in H-2(+) + and D-2(+)", PHYSICAL REVIEW A 72 (3): Art. No.030702, SEP, (2005).

4) Bing Shan, Shambhu Ghimire, and Zenghu Chang, "Generation of a XUV supercontnuum at the plateau of high harmonic spectrum", JOURNAL OF MODERN OPTICS 52 (2-3): 277-283 JAN-FEB (2005).

5) Bing Shan, Shambhu Ghimire, and Zenghu Chang, "Effect of orbital symmetry on high-order harmonic generation from molecules," PHYSICAL REVIEW A 69 (2): Art. No. 021404, FEB (2004).

E.2 Conference Proceedings:

1) Shambhu Ghimire, Ximao Feng, and Zenghu Chang, "Measurement of attosecond XUV pulses generated with polarization gating", submitted for SPIE Optics and Photonics, SPIE (2007)

2) Mahendra Man Shakya, Steve Gilbertson, Chengquan Li, Eric Moon, Zuoliang Duan, Jason Jacket, Shambhu Ghimire, and Zenghu Chang, "Effects of Carrier Envelope Phase on Single Shot XUV Supercontinuum Measurements", CLEO (2006) San Francisco, CA.

3) Mahendra Man Shakya, Steve Gilbertson, Chris Nakamura, Chengquan Li, Eric Moon, Zuoliang Duan, Jason Tackett, Shambhu Ghimire and Zenghu Chang, "Effect of Carrier Envelope Phase on Single shot XUV Supercontinuum Measurements" DAMOP (2006).

4) Shambhu Ghimire, Bing Shan, Chris Nakamura, Chun Wang and Zenghu Chang "The Effects of Ionization on the Generation of High Energy 6 fs Pulses", Division of Atomic and Molecular Physics (DAMOP 2005), Lincoln, NE.

5) Chakra Man Maharjan, Ali Alnaser, Xieo-MinTong, Predrag Ranitovic, Shambhu Ghimire, Bing Shan, Zenghu Chang, Igor Litvinyuk, and lewis C. Cocke "COLTRIMS Studies of Correlation in the Sequential Release of Two Electrons from Ar and Ne by Short Laser Pulses", (DAMOP 2005), Lincoln, NE.

6) Zenghu Chang, Bing Shan, Shambhu Ghimire, "Generation of XUV Supercontinuum and Attosecond Pulses", (CLEO 2005), Baltimore, MD.

7) Shambhu Ghimire, Bing Shan, and Zenghu Chang, "The effect of orbital symmetry on high harmonic generation in molecules", Super Intense laser Atom Physics (SILAP 2003), Dallas, TX.

8) Bing Shan, Shambhu Ghimire, Chun Wang and Zenghu Chang "Comparison of ellipticity dependence of high order harmonic generation from molecules and atoms", (DAMOP 2003), Boulder, CO.

9) Bing Shan, Shambhu Ghimire and Zenghu Chang, "Generation of single attosecond pulse in high harmonic plateau", Super Intense Laser Atom Physics (SILAP 2003), Dallas, TX.

10) Bing Shan, Shambhu Ghimire, Chun Wang and Zenghu Chang, "Generation of XUV supercontinuum and single attosecond pulse by polarization gating", Optical Society of America, 87^{th}annual meeting (OSA 2003), Tucson, AZ.

11) Shambhu Ghimire, Mahendra Shakya and Zenghu Chang, "High energy 6 fs pulses for generating a single shot XUV supercontinuum", International Conference on Multiphoton Processes (ICOMP 2005), Orford, QC, Canada.

12) Shambhu Ghimire, Bing Shan and Zenghu Chang, "Characterization of laser pulses with a time-dependent ellipticity for the generation of attosecond x-ray pulses" Workshop on Ultrafast X-ray science (2004), San Diego, CA.